Hydrogen Chloride Electrolysis in a Polymer-Electrolyte-
Membrane Reactor with Oxygen-depolarized Cathode

Elektrolyse von Chlorwasserstoff in einem Polymerelektrolyt-
Membranreaktor mit Sauerstoffverzehrkathode

Dissertation

zur Erlangung des akademischen Grades

Doktoringenieur

(Dr. - Ing)

von   MSc. Isaí González Martínez

geb. am   9 Juli 1986 in Monterrey, Mexiko

Promotionskommission:

    Prof. Dr.-Ing. habil. Kai Sundmacher   (Gutachter)

    Prof. Dr.-Ing. Thomas Turek   (Gutachter)

    Prof. Dr. Mihai Christov   (Gutachter)

    Prof. Dr. rer. nat. habil. Helmut Weiß   (Vorsitz)

Eingereicht am: 02.04.2015

Promotionskolloquium am: 29.10.2015

Acknowledgements

I would like to thank Prof. Sundmacher for the opportunity to undergo my PhD studies in his group, for his guidance and support along these four years. He together with the partners in Clausthal, Prof. Turek and Prof. Kunz helped me keeping focus on what was important in the project as well as the fruitful discussions in our project meetings. I acknowledge also Rafael Kuwertz, who besides providing the electrode membrane assemblies and other material required for the project was a very competent discussion partner, especially in the last phase of the project and the putting together of the patent and DFG report.

Very special thanks go to Tanja Vidaković-Koch for her guidance, constant discussions, and article/dissertation corrections, without her invaluable help this work wouldn't be completed. She was the person who was always there providing support, advice, help, and reprimands when needed, which helped keeping this work as well as publications on track. I managed to learn a lot from her, both on the scientific aspect (both in experiments and simulations) as well as in the way of presenting things and ideas. This work couldn't be brought to closure without the aid of Bianka Stein for the spraying, preparation of MEAs and DLS measurements; Markus Ikert for the SEM analysis and lab assistance; Torsten Schröder for the planning of the cyclone flow cells employed and lab setup realization; the personnel of the MPI and SVT mechanical workshops for the construction of the cells as well as Evelin Felsch for her support in the moving out to the Carnot building and MEA spraying. Thanks also go to Ivan Ivanov, Vladimir Panić, Miroslava Varničić and Nga Do for creating a very varied, interesting, and fun atmosphere in which not only working advices were shared, but also conversations about life, future perspectives, different traditions, which helped me to grow a lot as a person. I acknowledge them as they endured my mean comments of the day for quite some time (and even though they might deny it, they will miss them ☺). To the colleagues from the group and neighboring offices, whose advice, conversations, and getting together enriched my experience and made my time at the MPI a much cherished one.

At this point I would like to enormously thank my family for the support they showed me since my master studies abroad, the patience of communicating only via skype and being together only once per year. I would like to acknowledge my dad for his encouraging example of studies and work since his humble starting up to becoming a doctor, which motivated me into following his steps. To my mom as well who was always there for me for advice (and cooking recipes) and helped me become the person I am now. To my brothers I would like to greatly thank as they had to endure all the accumulated material and jokes of one entire year.

I learned a lot in these past years and hope to keep doing so, as we have every day from every person the opportunity to learn something new.

Table of Contents

Summary

In this work, a novel process for the electrolysis of hydrogen chloride in a polymer electrolyte membrane reactor with an oxygen depolarized cathode was studied by means of half-cell experiments and the modeling of individual reactor components (anode, electrolyte membrane, and cathode). The complete reactor experiments were carried out by our partners from the Technical University of Clausthal. They also produced the membrane electrode assemblies with different catalyst and ionomer compositions employed in this work.

Our experiments were carried out in a cyclone flow cell, where defined temperature and mass transfer conditions can be attained. The kinetics of the hydrogen chloride oxidation were measured and identified. An optimization of the catalyst and ionomer (Nafion) loadings was carried out. A surprisingly high optimum of about 60 wt.% Nafion was found, which is significantly higher than for other electrochemical gas phase reactions (such as hydrogen oxidation, oxygen reduction, etc.). Although technically relevant current densities were reached for all investigated electrodes, a further need for optimization was identified as, theoretically, higher current densities are possible (up to 1000 mA cm^{-2}).

With help of half-cell experiments, kinetics of the HCl oxidation was studied. A 1-dimensional isothermal agglomerate reactor model was developed in order to analyze the transport processes of HCl and water. This showed that the membrane conductivity decreases due to the HCl profile through it. Another important finding is that water produced by the cathodic oxygen reduction reaction condensates in the catalyst layer (as the cathode feed is liquid water or fully humidified oxygen) and diffuses through the membrane, improving its conductivity and compensating for losses due to the HCl concentration profile through it. These results showed the importance of the water balance in the membrane and its impact on the overall reactor operation.

With the established model, the isothermal reactor polarization curves could be reproduced up to current densities of 400 mA cm^{-2}. The cell potential curve at higher current densities could not be described because the reactor doesn't behave isothermal in this area.

The experimental results proved the feasibility of the gas phase electrolysis of hydrogen chloride with the use of an oxygen depolarized cathode. The resulting cell potentials below 1 V represent an important advance for the development of a technical application of the new process for the large-scale chlorine recycling.

Zusammenfassung

Im Rahmen dieser Arbeit wurde ein neuer Prozess zur Elektrolyse von gasförmigem Chlorwasserstoff in einem Polymerelektrolyt-Membranreaktor mit einer Sauerstoffverzehr-kathode verfahrenstechnisch untersucht. Dazu wurden sowohl Halbzellen Experimente als auch die Modellierung von einzelnen Reaktorkomponenten (Anode, Membran, Kathode) und des gesamten Reaktors in enger Kooperation mit der TU Clausthal durchgeführt.

In der TU Clausthal wurden Membran-Elektrode-Einheiten mit unterschiedlichen Zusammen-setzungen hergestellt. Durch Halbzellen-Experimente in einer Zyklonzelle wurde das System unter definierten Temperatur- und Massentransportbedingungen vermessen und die Kinetik der Oxidation von Chlorwasserstoff identifiziert. Auch dadurch war eine Optimierung der Beladungen an Katalysator und Ionomer (Nafion) der Anode und Kathode möglich. Es wurde für die anodische HCl-Oxidation ein optimaler MEA Nafiongehalt von *ca.* 60% festgestellt, der deutlich höher als bei anderen elektrochemischen Gasphasenprozessen (z.B. Wasserstoffoxidation, Sauerstoffreduktion, usw.) liegt. Die durchgeführten Experimente zeigten noch weitere Optimierungsmöglichkeiten, da theoretisch auch höhere Stromdichten (bis zu 1000 mA cm^{-2}) erreicht werden könnten.

Durch die Halbzellen-Experimente konnte die Kinetik der HCl Oxidation untersucht werden. Dabei wurden mit einem aufgestellten, isothermen 1-dimensionalen Agglomeratsmodell die Transportprozesse von HCl und Wasser analysiert. Die Experimente zeigten, dass die Leitfähigkeit der Membran wegen des HCl-Konzentrationsprofils durch die Membran bei steigenden Stromdichten sinkt. Eine wichtige Erkenntnis ist, dass der Wassertransport durch die Membran verbessert wird aufgrund des Transportes von kondensiertem Wasser aus der kathodischen Sauerstoffreduktion unter einer hohen Befeuchtung des Kathodengases oder Nutzung eines flüßigen Elektrolyts. Dies führt zu einer Verbesserung der Leitfähigkeit der Membran die den Verlust der Leitfähigkeit durch das Konzentrationsprofil von HCl durch die Membran kompensiert.

Mit dem aufgestellten, isothermen Reaktormodell konnten die Polarisationskurven bis zu einer Stromdichte von 400 mA cm^{-2} gut wiedergegeben werden. Der Zellspannungsverlauf bei höheren Stromdichten kann noch nicht beschrieben werden, da sich der Reaktor in diesem Bereich nicht mehr isotherm verhält.

Die Experimente zeigten, dass die Gasphasenelektrolyse von Chlorwasserstoff mit einer Sauerstoffverzehrkathode möglich ist. Die erhaltenen Zellspannungen von unter 1 V repräsentieren einen großen Schritt auf dem Weg zu einer möglichen Anwendung des neuen Prozesses für das großtechnische Recycling von Chlor.

---

1   Introduction

Chlorine is a platform chemical with about 15,000 compounds currently commercially produced [1]. It takes part in the manufacture of a wide range of consumer products like textiles, agrochemicals, pharmaceuticals, insecticides, plastics, etc. [2]. Chlorine plays its main role in the industrial sector, predominantly in the production of plastics and organic solvents. Even though chlorine is not always present in the end product, it is required in at least one step of the manufacture process of all compounds shown in Figure 1-1.
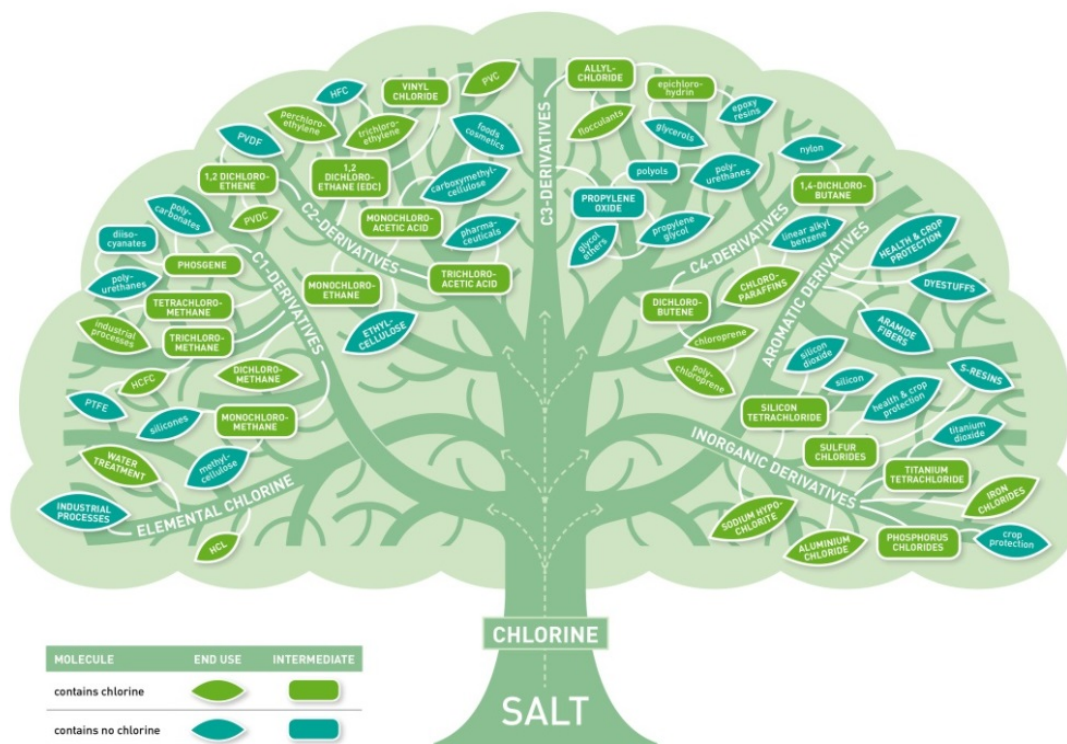
Figure 1-1 Chlorine tree [2]

Total chlorine production in Europe was 9.94 million tons in 2011 and 9.34 million tons in 2010 [3]. Germany is the biggest chlorine producer in Europe, accounting for 43.8% of the total 2011 production (Figure 1-2a). Chlorine is produced mainly via chloralkali electrolysis, which is the second most energy intensive process industrially employed. The latest chloralkali technology is the membrane process, requiring *ca* 3.1-3.3 MWh per ton of chlorine [4]. One of the main uses of chlorine is in chlorination reactions for plastic production (PVC, PVDF, Isocyanates, etc., see Figure 1-2), which produce hydrogen chloride as a byproduct. Taking PVC as an example, it is synthetized from vinyl chloride monomer (VCM), which is produced from ethylene, eq. (1-1):

$$C_2H_{4(g)} + Cl_{2(g)} \rightarrow C_2H_3Cl_{(g)} + HCl_{(g)} \qquad (1\text{-}1)$$

generating hydrogen chloride as a byproduct in a 1:1 ratio to consumed chlorine. For diisocyanate production, such as methylenediphenyl and toluene diisocyanates (MDI and TDI), this ratio increases to 2:1.
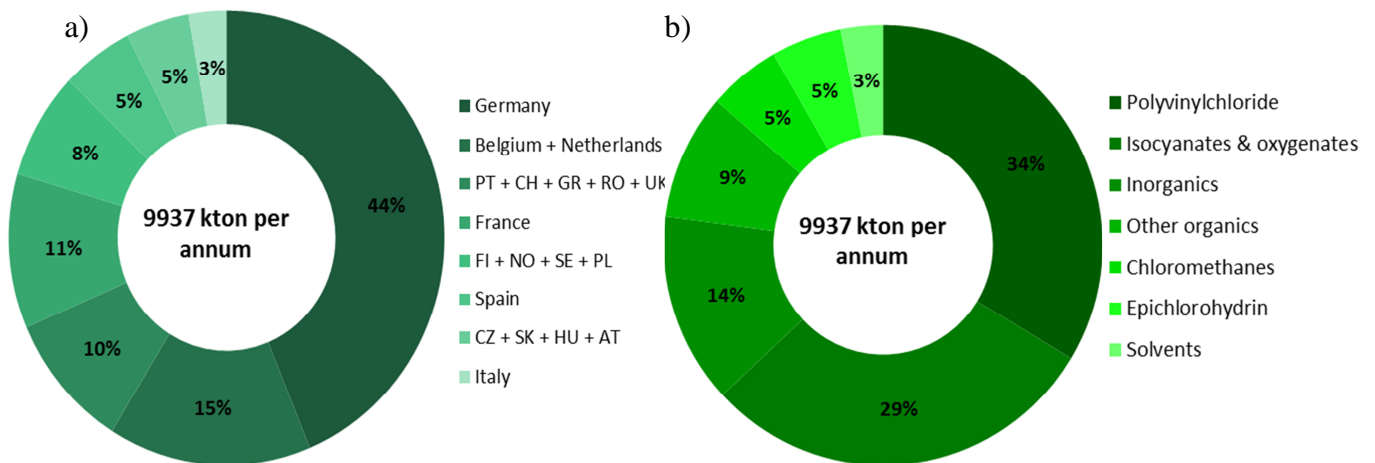
Figure 1-2 a) Chlorine production in 2011 by country; b) Chlorine consumption by industrial segment [3]

Because of the high volumes of generated HCl and the difficulty to commercialize it as a gas, normally anhydrous HCl is absorbed in water to form hydrochloric acid. This acid is commonly employed for other chemical reactions or neutralized and disposed as waste water. But the high HCl market saturation, the required conditions for HCl storage and the legal regulations regarding salt content in waste water have motivated the development of different process alternatives in order to reduce waste streams and improve process economy. For example, in PVC production waste hydrogen chloride is employed in the oxychlorination reaction, eq. (1-2)[5], with oxygen and ethylene to increase chlorine usage. This allows the "recycling" of some of the chlorine contained in hydrogen chloride into ethylene dichloride molecules (EDC).

$$2C_2H_{4(g)} + 4HCl_{(g)} + O_{2(g)} \rightarrow 2C_2H_4Cl_{2(g)} + 2H_2O_{(g)} \qquad (1-2)$$

EDC can be thermally cracked into VCM molecules at high temperatures, allowing further PVC production but still yielding some hydrogen chloride as a byproduct according to eq. (1-3).

$$C_2H_4Cl_{2(g)} \rightarrow C_2H_3Cl_{(g)} + HCl_{(g)} \qquad (1-3)$$
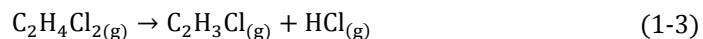
Therefore, not all hydrogen chloride resulting from PVC production can be recycled. On the other hand, for processes like the diisocyanate production, where no reaction variants directly employing hydrogen chloride as an educt exist, chlorine recovery from HCl has been proved to be an attractive solution. Chlorine recycling from HCl can proceed via a catalyzed chemical oxidation and an electrochemical oxidation [6]. The chemical route employs hydrogen chloride and oxygen as educts and requires high temperatures (>300°C [7]), high capital costs, big reactors and proceeds according to the stoichiometry of the Deacon process, eq. (1-4):

$$4HCl + O_2 \rightarrow 2Cl_2 + 2H_2O \qquad (1-4)$$

This reaction is commercially used in the Sumitomo and Bayer processes, which employ fixed bed reactors with ruthenium oxide catalysts supported on TiO$_2$ (rutile) and SnO$_2$ (cassiterite) respectively. This process has a very low energy consumption per ton of chlorine (0.17 MWh, see Table 1-1) [8]. In contrast, the electrochemical route can proceed according to the Deacon process stoichiometry and the hydrogen chloride splitting reaction stoichiometry, eq. (1-5):

$$2HCl \rightarrow Cl_2 + 2H_2 \qquad (1-5)$$
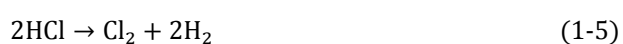
Both electrochemical variants operate at milder temperatures (<90°C), and can use either hydrogen chloride or hydrochloric acid as educts. These processes require smaller reactors and lower capital investments than the chemical route, allowing for decentralized production, partial plant shutdowns, and easy production increase by coupling of new reactors to existing units. Due to these advantages, electrochemical processes have been widely used since the 50's [5]. An overview of the figures of merit for HCl electrolysis is shown in Table 1-1.

Table 1-1 Comparison of the available processes for Chlorine production from HCl recycling

Parameter	Units	Bayer-Uhde-Hoechst	Dupont-Denora	Bayer-Uhdenora	This work
Reversible cell potential[1]	V	-1.41	-0.99	-0.21	0.21
Operating cell potential	V	-2.00	-1.60	-1.35	-0.97
Typical current density	kA m^{-2}	4.0	10.0	4.0	4.0
Temperature	°C	60-90	70-90	≤60	≤60
Separator	-	PVC Diafragma	Nafion	Nafion	Nafion
Anode	-	Graphite	Not disclosed	Ti/Pd-DSA	Pt/C
Cathode	-	Graphite	Not disclosed	Rh. sulfide	Pt/C
HCl physical state	wt %	Liquid (20%)	Gas (100%)	Liquid (20%)	Gas (100%)
Side product	-	H_2	H_2	H_2O	H_2O
Energy consumption	MWh/ton Cl2	1.50	1.25	1.02	0.73

[1] Values are calculated for 60°C, 1M HCl or 101.3 kPa

Two processes depart from liquid hydrochloric acid: the Bayer-Uhde-Hoechst process based on HCl splitting stoichiometry and the Bayer-Uhdenora process, based on Deacon stoichiometry. The first one uses a PVC diaphragm as a separator, while the second one employs a polymer-electrolyte membrane (PEM). The PVC diaphragm produces higher potential losses than a PEM and provides a much lower selectivity to ion crossover, which has encouraged the use of PEM separators for more modern processes.

Operational costs of electrochemical processes depend heavily on the electricity cost, which has been constantly increasing [9], encouraging investigation and optimization of electrochemical process alternatives with lower energy consumption. This resulted in the development of the Dupont-Denora process [10-12], which is based on the Bayer-Uhde-Hoechst process stoichiometry but employs a PEM membrane as a separator, gas diffusion electrodes (GDEs), and hydrogen chloride as the educt, allowing for higher current densities with similar energy consumption. The use of GDEs also allows reactor sizes to be reduced, as they have a typical thickness of 0.5 mm [13] in comparison with dimensionally stable anodes (DSAs). Technical reactors for liquid HCl electrolysis employ massive electrodes with thickness from 0.5 to 2.0 mm. The Bayer-Uhde-Hoechst process employs graphite anodes, which show high levels of wear rate and geometry instability but are cheap. The Bayer-Uhdenora process, still the standard industrially employed

process, employs DSA consisting of a titanium mesh core covered with an electrocatalytical layer (around 10 µm thick) of cobalt, ruthenium and/or iridium oxides [14, 15]. DSAs are normally meshes (also louvre, C-shaped and other profiles have been used in chloralkali cells [5]) or are perforated in order to ensure better liquid mixing and gas release. Schematic representations of two reactor types with DSA and with GDE are shown in Figure 1-3a.
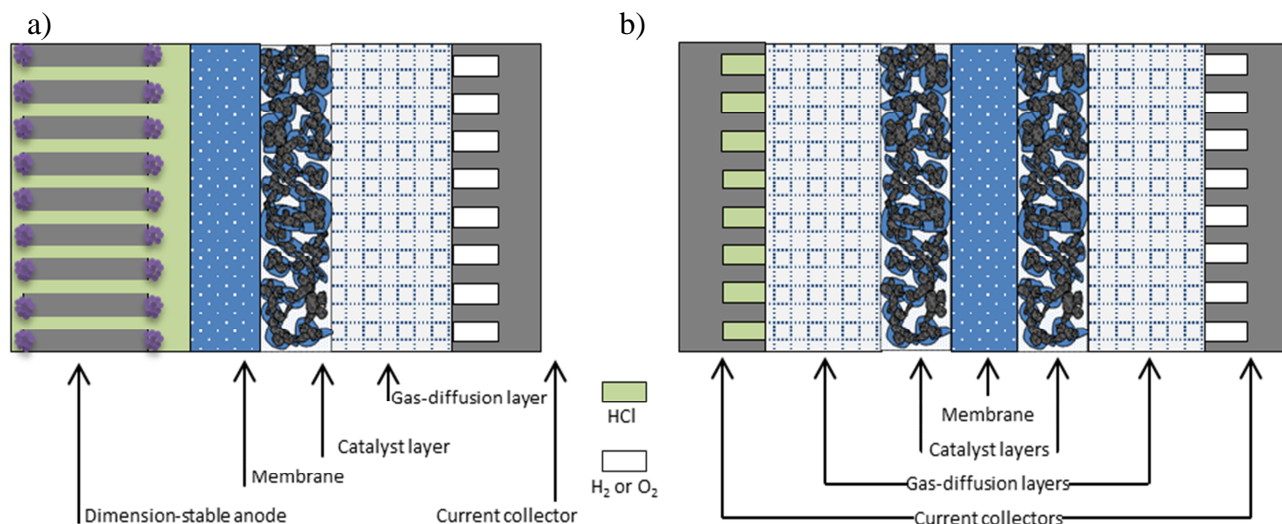

Figure 1-3 Reactor configurations for the HCl electrolysis. a) Dimensionally stable anode (DSA) for the use of liquid HCl as an educt; b) Gas diffusion electrode (GDE) for the use of hydrogen chloride as an educt.

Based on the thermodynamic data presented in Table 1-1, following the Deacon Process stoichiometry combined with the use of an oxygen depolarized cathode and hydrogen chloride as an educt, should lead to lower cell potentials and even higher energy saving. In the above mentioned patent [12], the possibility of the electrolysis of hydrogen chloride with an oxygen-depolarized cathode was mentioned, but no data, possible advantages, or pilot/technical realization was documented or further discussed. This process variant, eq. (1-4), was investigated departing from hydrogen chloride using a PEM separator due to its enormous theoretical energy savings (see chapter 2), higher mass transport rates from the gas-phase, and its allowance to spare HCl absorbers and heat exchangers. The focus of this work was to analyze the process thermodynamics, characterize the GDEs for the hydrogen chloride oxidation (HClOR), and to create kinetic formulations for the HClOR in order to describe and optimize a lab-scale reactor using this process. The only available information about the reaction mechanism of the HClOR was presented by Eames and Newman [10], who employed Pt/RuO_2 electrodes to characterize reaction (1-5) at different temperatures in a fuel cell type reactor. In their setup, only total cell potential could be measured and a separation of losses associated with the membrane or cathode was not possible.

The use of oxygen depolarized cathodes is currently linked to the use of PEM-membranes, from which Nafion is still the market leader [16]. PEMs have the disadvantage of showing ionic conductivity only when water is present in their structure, limiting their operational temperature to less than 90°C and high relative humidity in the gas feeds. Considering this, process variants

involving anhydrous gas feeds are, with state-of-the-art technology, still non-operational. Therefore, water management is of crucial importance in electrolyzers employing PEMs. Water transport in hydrogen chloride electrolyzers was investigated by Motupally *et al.* [11], who reported the electroosmotic drag of water through Nafion membranes to be 3.5 with 100% hydrogen chloride as the anode feed. Lower values were shown by other researchers: 2.5 by Balko *et al.* [17] for a 2.5 M liquid HCl anodic feed and 1.4 by Zawodsinski *et al.* [18] for a 100% humidified hydrogen feed (the latter was employed in [10]). There is currently little available information about the hydrogen chloride-Nafion system (ionic conductivity [19], cathodic platinum poisoning with HCl [20], etc.). Information is mostly available for the liquid HCl-Nafion system, where data about diffusion coefficients in Nafion [21], water transport [22, 23], and Nafion conductivity [24, 25] have been reported. Therefore, the only sources for comparison between processes are thermodynamic calculations and some experimental data. The technical feasibility of the process investigated in this work was shown in cooperation with the University of Technology Clausthal, where a reactor coupling the HClOR and ORR was developed.

This work was organized according to the following structure: in chapter 2, the different available processes and their thermodynamics are explained. In chapter 3, the experimental setups employed for the HCl oxidation and oxygen reduction measurements are shown. In chapter 4, the preparation and characterization of the catalyst inks and membrane electrode assemblies (MEAs) employed in this work are presented. In chapter 5, the cathodic and anodic half-cell reaction measurements are shown. In chapter 6, the modeling and kinetic analysis of both reactions and the membrane is presented together with an analysis of the full reactor. Later, conclusions and an outlook for future work are given.

2 Thermodynamics

2.1 Basic principles

As mentioned in chapter 1, the two main electrochemical processes currently used on an industrial scale are the Bayer-Uhde-Hoechst and the Bayer-Uhdenora processes [5]. The former one employs anodic hydrochloric acid oxidation and cathodic hydrogen evolution reaction (HER).

Overall	$2HCl_{(aq)} \rightarrow Cl_{2(g)} + H_{2(g)}$	(2-1)
Anodic	$2HCl_{(aq)} \rightarrow Cl_{2(g)} + 2H^+ + 2e^-$	(2-2)
Cathodic	$2H^+ + 2e^- \rightarrow H_{2(g)}$	(2-3)
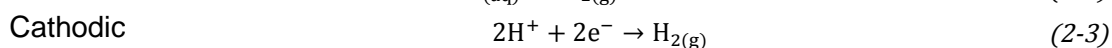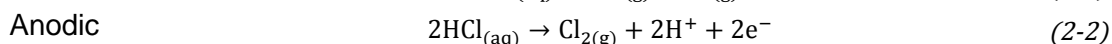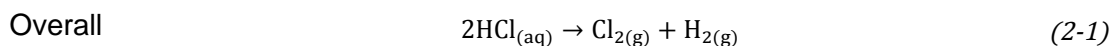
On the other hand, the Bayer-Uhdenora process, which is currently industrially employed, features the same anodic reaction but uses oxygen reduction (ORR) as the cathodic reaction.

Overall	$4HCl_{(aq)} + O_{2(g)} \rightarrow 2Cl_{2(g)} + 2H_2O_{(l)}$	(2-4)
Anodic	$4HCl_{(aq)} \rightarrow 2Cl_{2(g)} + 4H^+ + 4e^-$	(2-5)
Cathodic	$4H^+ + 4e^- + O_{2(g)} \rightarrow 2H_2O_{(l)}$	(2-6)
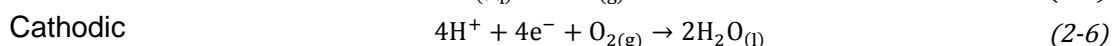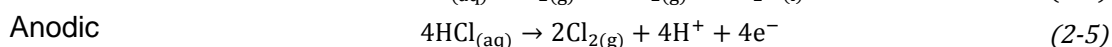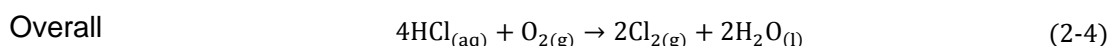
The use of an oxygen depolarized cathode represents an advantage in terms of the reversible cell potential U_{rev} in comparison with processes employing the HER. Different processes employing anhydrous hydrogen chloride have been developed or described [12, 26]: the Dupont-Denora process, which is based on the stoichiometry of the Bayer-Uhde-Hoechst process:

Overall	$2HCl_{(g)} \rightarrow Cl_{2(g)} + H_{2(g)}$	(2-7)
Anodic	$2HCl_{(g)} \rightarrow Cl_{2(g)} + 2H^+ + 2e^-$	(2-8)
Cathodic	$2H^+ + 2e^- \rightarrow H_{2(g)}$	(2-9)
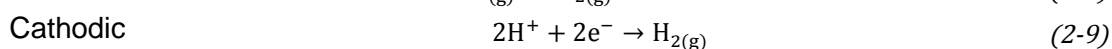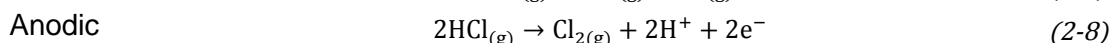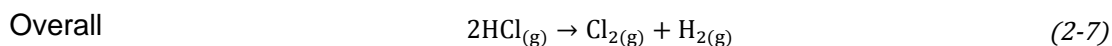
and the process studied in this work, based on the Deacon process stoichiometry:

Overall	$4HCl_{(g)} + O_{2(g)} \rightarrow 2Cl_{2(g)} + 2H_2O_{(l)}$	(2-10)
Anodic	$4HCl_{(g)} \rightarrow 2Cl_{2(g)} + 4H^+ + 4e^-$	(2-11)
Cathodic	$4H^+ + 4e^- + O_{2(g)} \rightarrow 2H_2O_{(l)}$	(2-12)
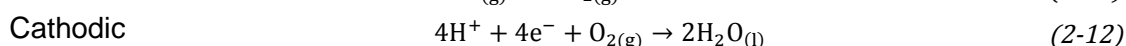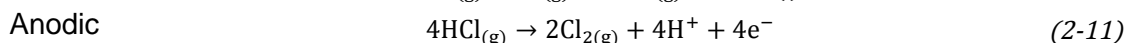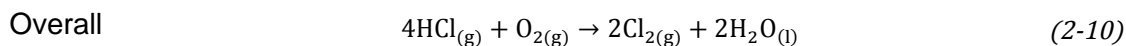
The thermodynamics of the above mentioned processes will be presented in the next sections.

2.2 Reversible electrode potential

The reversible electrode potential is defined as the potential in a cell composed of a standard hydrogen electrode (SHE) paired with any other given electrode. This allows the calculation of the reversible electrode potential directly from thermodynamic data:

$$E_{\text{rev}} = -\frac{\Delta G}{zF} = -\frac{\Delta H - T\Delta S}{zF} \qquad (2\text{-}13)$$

where G stands for the free Gibb's energy, H for the enthalpy, S for the entropy, z the number of exchanged electrons, and F Faraday's constant. In order to determine the reversible electrode potential at temperatures and concentrations different than standard conditions, the Nernst equation is employed:

$$E_{\text{rev}} = E° - \frac{RT}{zF}\ln\left[\frac{\prod a_p^k}{\prod a_r^m}\right] \qquad (2\text{-}14)$$

where a_i stands for the activities of products and reactants, k and m for the stoichiometric coefficients, and $E°$ for the reversible electrode potential at standard conditions. Gas mixtures were considered to be ideal and no interaction parameters or mixing rules were employed. The activity of a single gas is defined as:

$$a_i = \frac{f}{P_{ref}} = \frac{\phi\, P}{P_{ref}} \tag{2-15}$$

where f stands for gas fugacity and ϕ for the fugacity coefficient. Gas activity was calculated using the Stryjek-Vera modification of the Peng-Robinson equation, based on the compressibility factor z_g which provides very good accuracy even for polar gases (see Appendix 10.3.1).

$$P = \frac{z_g RT}{V} \tag{2-16}$$

The fugacity coefficient was considered to be unity as the pressures and temperatures investigated don't deviate considerably from standard conditions and z_g also showed values very close to one. The Nernst equation doesn't consider entropy losses so a temperature correction is needed, which for the ORR was obtained from Bratsch [27].

$$E_{rev}^c = 1.229 + \frac{RT}{zF}\ln\left[\frac{a_{O_2}\,a_{H^+}^4}{a_{H_2O}^2}\right] - 8.456 \cdot 10^{-4}(T_s - 25) \tag{2-17}$$

For the HClOR no temperature dependence correlation is reported, but was obtained from the change in reversible electrode potential with temperature or entropy change according to eq. (2-13).

$$E_{rev}^a = 0.9879 - \frac{RT}{zF}\ln\left[\frac{a_{HCl}^2}{a_{H^+}^2 a_{Cl_2}}\right] + 9.711 \cdot 10^{-5}(T_s - 25) \tag{2-18}$$

The effect of temperature and concentration on the reversible electrode potentials for the ORR and HClOR is shown in Figure 2-1. In Figure 2-1 a), the highest reversible potentials are obtained at high oxygen concentrations and low temperatures for the ORR. On the other hand, for the HClOR, Figure 2-1b), low reversible electrode potentials are obtained at high hydrogen chloride concentrations and low temperatures.
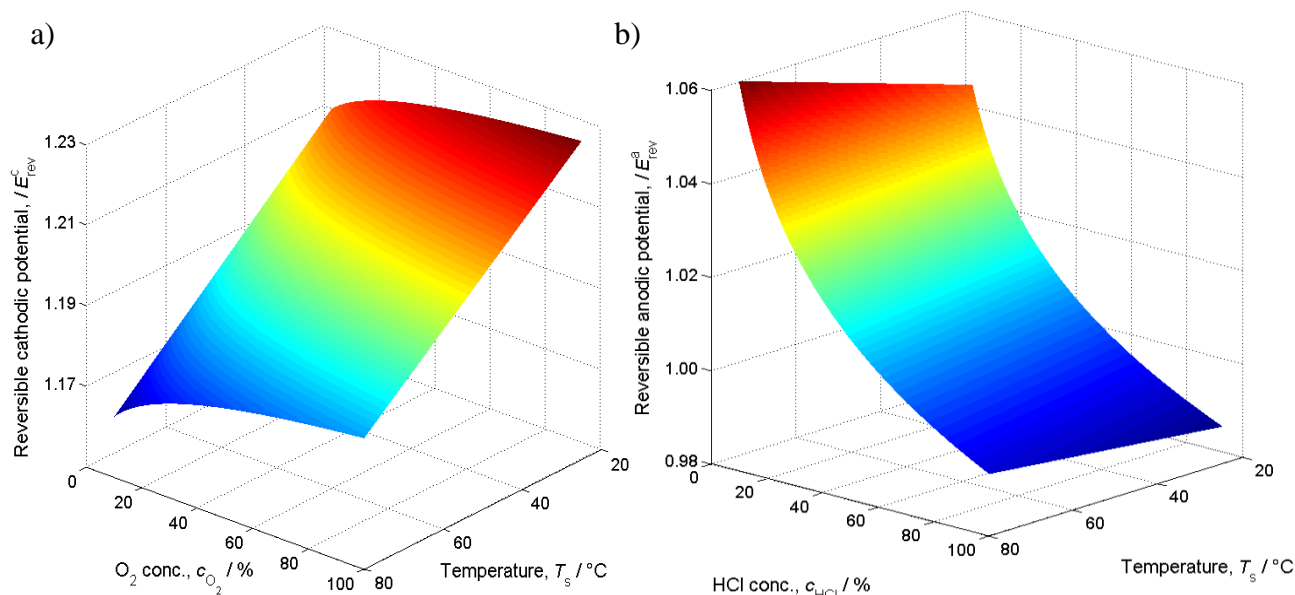

Figure 2-1 Reversible electrode potentials as a function of temperature and educt for the a) ORR; b) HClOR.

In the case of the HClOR in GDEs, the question arises, if the reaction takes place in the liquid or gaseous phase. Nafion is able to uptakes water and hydrogen chloride has a great affinity to absorb in water. The activity of HCl in water (see Appendix 10.3.2) takes values considerably higher than those in the gas phase (11.8 *vs* 0.988 at 60°C, respectively), which allows greater shifts in the reversible electrode potential. The reversible electrode potential for the liquid phase reaction is defined as:

$$E_{rev}^a = 1.358 - \frac{RT}{zF} \ln\left[\frac{a_{Cl^-}^2}{a_{Cl_2}}\right] - 1.248 \cdot 10^{-3}(T_s - 25) \tag{2-19}$$

The measurement of single ion activities is not possible as ions are always present as pairs in solution. Therefore, for hydrochloric acid the mean activity coefficient is obtained by assuming the activity of chloride ions is the same as for protons. This activity is determined by the mean molarity activity coefficient (further referred only as activity coefficient) with a reference molarity (M^θ) of one (see Appendix 10.3.2).

$$a_{Cl^-} = \gamma_{Cl^-} \frac{M_{Cl^-}}{M_{Cl^-}^\theta} \tag{2-20}$$

Employing eq. (2-18) and (2-19), the effect of HCl and chlorine activities was investigated and presented in Figure 2-2. Considerably lower potential values are obtained at high HCl concentrations and temperatures in comparison to standard conditions. The effect of the chlorine partial pressure is considerable, yielding as well values much lower than at standard conditions. To illustrate this, the use of a low chlorine activity (0.001) lowers the reversible electrode potential around 90 mV (Figure 2-2b) compared to the case where activity was assumed to be unity (Figure 2-2a). Increasing the activity of chlorine in an order of magnitude yields a reversible electrode potential reduction of only 60 mV, closing more to the theoretical value of 1.358 at 25°C.
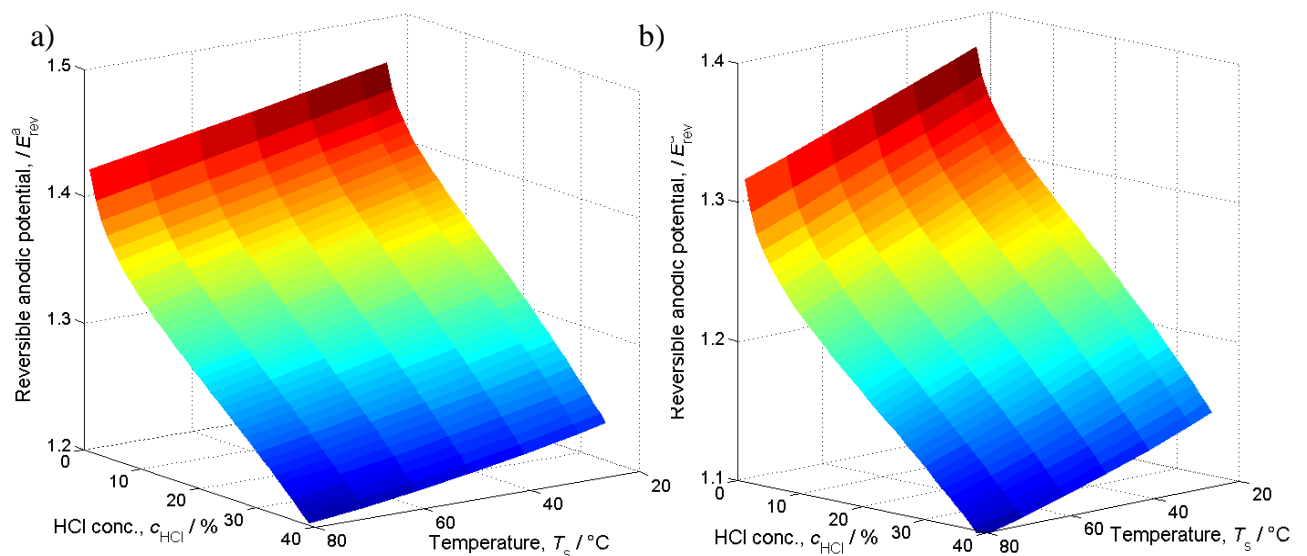

Figure 2-2 Reversible electrode potentials as a function of temperature and chlorine activity for the HClOR in the liquid phase considering a) a chlorine activity of 1; b) a chlorine activity of 0.001.

As seen in Figure 2-2, the reversible potential values are very close to one at temperatures above 70°C and HCl concentrations above 35%. The use of activities in eq. (2-19) allows for higher potential reductions, as activities take values considerably higher than one in the HCl-water system), especially at high HCl concentrations (see Appendix 10.3.2). This allows obtaining reversible electrode potential reductions of up to 140 mV.

2.3 Reversible cell potential

The reversible cell potential U_{rev} can be obtained by subtracting the reversible electrode potential of the anode from the reversible electrode potential of the cathode:

$$U_{rev} = E_{rev}^c - E_{rev}^a \qquad (2\text{-}21)$$

Due to the sulfonic groups contained in Nafion membranes, chloride ions are not able to crossover through them. But water is uptaken by Nafion, and HCl dissociates in it when absorbed from the gas phase. Due to this dissociation in the anode, a potential difference builds between the anode and cathode, the so-called Donnan potential. Protons from the anode are not able to diffuse to the cathode, as they need to balance the negative charge of the chloride ions at the anode. This potential difference affects the reversible potential and must be considered in eq. (2-1). The Donnan potential can be described by the following equation [28] with a_{H^+} as the proton activity:

$$E_{l,H^+}^{mem} = \frac{RT}{F}\ln\left(\frac{a_{H^+}^{an}}{a_{H^+}^{ca}}\right) \qquad (2\text{-}22)$$

For the sake of comparing the different HCl oxidation processes, the effect of the Donnan potential can be neglected for processes employing the same HCl phase (liquid or gaseous), as their proton activities will be identical. A further insight into the effect of the Donnan potential is given in chapter 6.6.

Reversible cell potential was calculated for all processes in Figure 2-3. It is observed that only the Dupont-Denora process shows a positive dependence of U_{rev} with temperature.
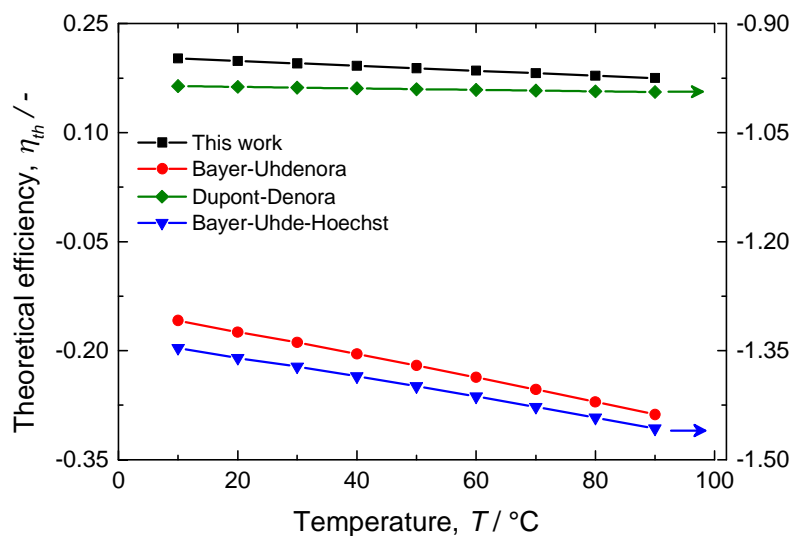

Figure 2-3 Reversible cell potentials for the different HCl oxidation processes.

For the process studied in this work, reversible cell potentials of 0.241, 0.227, 0.218, and 0. 208 V are obtained for temperatures of 25, 40, 50, and 60°C.

To compare the theoretical efficiency η_{th} of different processes, the ratio between irreversible losses and maximal available chemical energy is used:

$$\eta_{th} = 1 - \frac{T\Delta S}{\Delta H} \tag{2-23}$$

In this equation, if the ratio of the entropy change to the enthalpy change is negative, efficiencies higher than unity are obtained. This is the case of processes in which the entropy change is negative and the enthalpy change is positive, as in the case of the Dupont-Denora process.

In Figure 2-4 it can be observed that non-spontaneous processes have higher thermodynamic efficiency with increasing temperature, while for the spontaneous process the effect is opposite.

The difference between η_{th} and unity show the effect of irreversible heat loss at higher temperatures, for which the Bayer-Uhdenora process shows the highest improvement and the Bayer-Uhde-Hoechst the least. For the process studied in this work it is seen that theoretical process efficiencies around 38% can be expected between 50-80°C, the range where industrial processes operate.
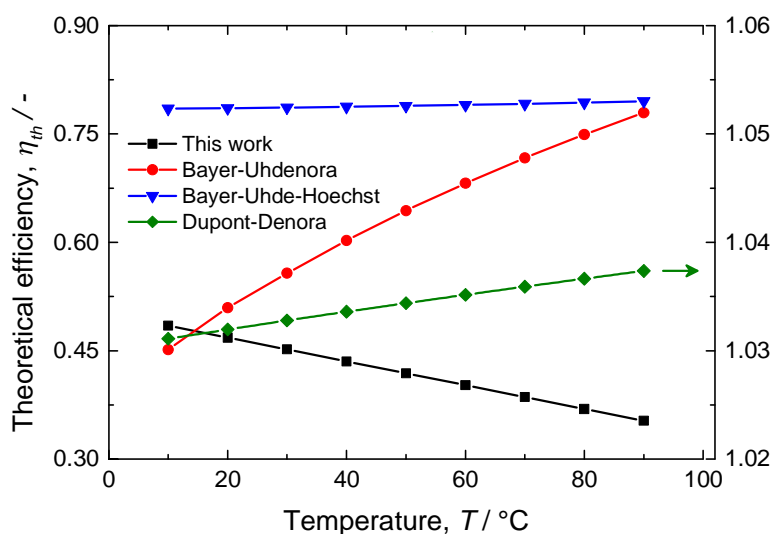
Figure 2-4 Theoretical efficiency for the different HCl process variants.

For the process studied in this work, the reversible cell potential was analyzed as a function of reactant concentration. It is observed that high reactant concentrations favor low cell potentials, being this effect more notorious for processes employing the ORR as the cathodic reaction. Figure 2-5b) shows the effect of relative humidity in the cathode feed. Reversible cell potential decreases with increasing relative humidity. A higher relative humidity implies a lower oxygen activity, as higher water vapor content diminishes the molar fraction of oxygen in the gas stream, which has to be evaluated in experiments in order to determine which parameter shows a higher impact on

reactor operation. A further insight into the effect of temperature and partial pressure is given in sections 5.3.4 and 5.3.5.
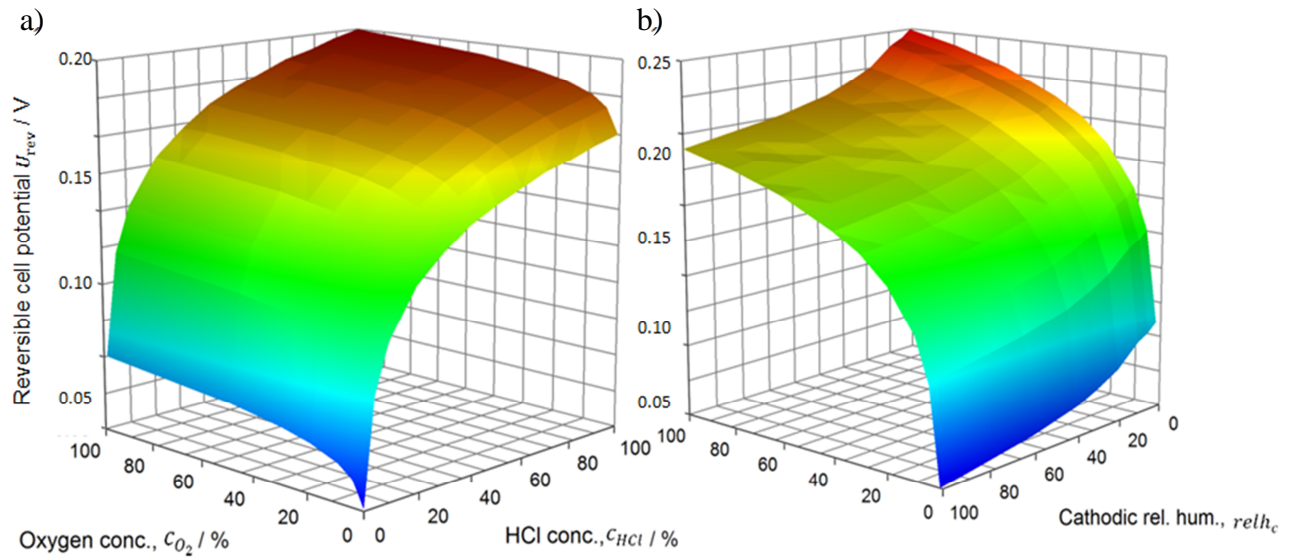
Figure 2-5 Reversible cell potentials as a function of a) anodic feed concentration (hydrogen chloride) and cathodic feed concentration (oxygen); b) relative humidity of the cathodic feed.

2.4 Concluding remarks

As observed from the reversible cell potentials, the use of oxygen depolarized cathodes brings important savings due to the lower potentials required for the hydrogen chloride electrolysis. The lowest reversible anodic electrode potential was obtained at high hydrogen chloride concentrations and low temperatures. The highest cathodic electrode potential was obtained at high oxygen concentrations and low temperatures. In the cathode, lower relative humidity favored higher cell potentials as they result in higher oxygen concentrations.

The reversible potential of the process studied in this work shows a considerable improvement in comparison to other processes, as it is the only one thermodynamically spontaneous, yielding a positive potential or a theoretical net energy gain. Coupled to this is a reduction of the investment costs as no HCl absorption step is required (absorber and heat exchangers), and lower operational costs due to a maximal 40% thermodynamic efficiency. Therefore, this process theoretically shows a higher potential for energy saving as any other existing process for chlorine recycling [6].

3 Experimental setup

The following setup was employed for the characterization of the gas diffusion electrodes and measurement of polarization curves for the HCl oxidation and ORR reduction.

3.1 HCl oxidation

Measurements were performed in the setup presented in Figure 3-1. Hydrogen chloride (grade 4.5, 99.8% purity) and nitrogen (grade 5.0, 99.999% purity) were employed (Linde, Germany). Gas inlets were regulated by In-flow mass flow controllers (Bronkhorst Mättig, Germany). Hydrogen chloride or oxygen were mixed with nitrogen to achieve the desired concentrations and directed to the cyclone flow cell [29]. The cell was kept in a Makrolon capsule to enclose possible hydrogen chloride or liquid electrolyte leakages. This capsule was placed in a UNP500 convection oven with integrated temperature control (Memmert, Germany). Gas products from the cell were neutralized in a packed glass column in counter flow with concentrated NaOH. The cell is shown in detail in Figure 3-2a.
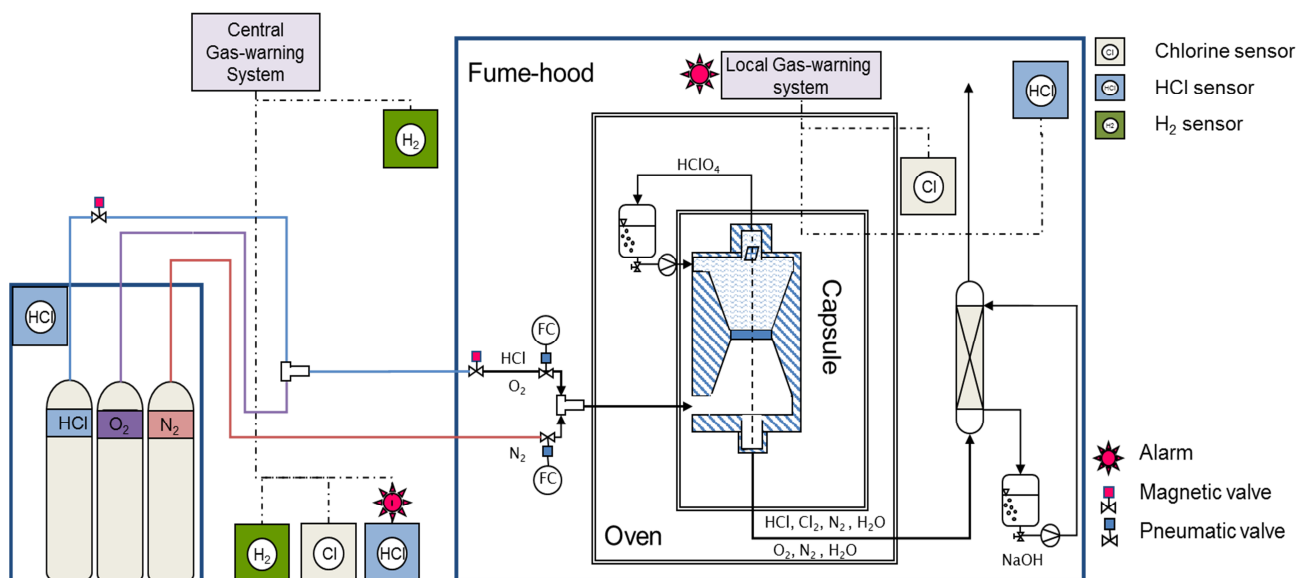
Figure 3-1 Setup for the electrochemical measurements of the HCl oxidation and ORR.

The membrane electrode assembly (MEA, 4) was placed between the two conic compartments of the cell with the gas diffusion layer (GDL, 5) facing the working electrode compartment. A titanium electron conductive support (8) was contacted with the GDL. In the working electrode compartment (1) the gas mixture circulates and reacts at the MEA, liberating protons which are transported through a Nafion 117 membrane to the counter electrode compartment (2). A 4 cm^2 platinized platinum net was employed as the counter electrode (9). The membrane was supported on a perforated PTFE disc (7) to assure mechanical stability. The counter electrode compartment was filled with deaerated 1M solutions of perchloric or sulfuric acid (Merck, Germany). The liquid electrolyte was heated in a jacketed glass vessel controlled by a thermostat F31 (Julabo, Germany) and circulated to the cyclone flow cell by means of a peristaltic

pump (Heidolph, Germany). The reference electrode vessel (3) was connected to the lower compartment of the cell, 2 mm away from the MEA and filled with the liquid electrolyte.

1: Working electrode compartment
2: Counter electrode compartment
3: Reference electrode compartment
4: Catalyst coated membrane
5: Gas diffusion layer
6: Viton gasket seals
7: Perforated PTFE disc
8: Electron conductive support
9: Counter electrode
10: Counter electrode compartment exit
11: Counter electrode compartment entrance
12: Working electrode compartment entrance
13: Working electrode compartment exit
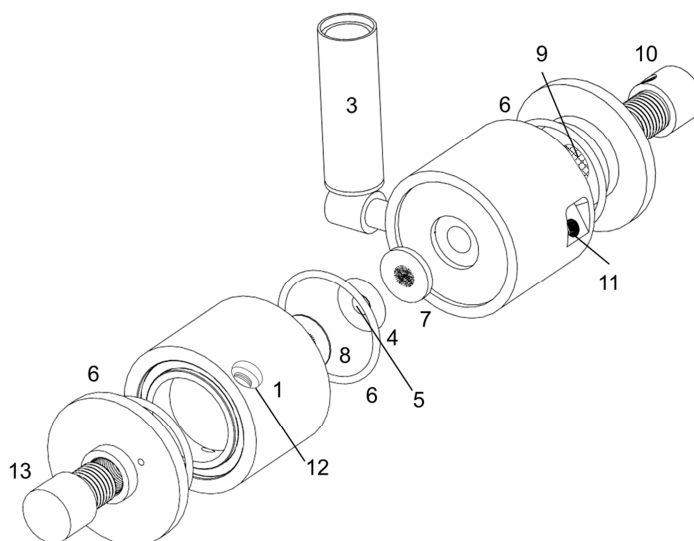
Figure 3-2 Schematic representation of the cyclone cell.

A saturated Ag/AgCl electrode (Meinsberger, Germany) was employed as the reference electrode. The cell was leak-proofed with Viton gasket seals (6). Temperature was monitored with PTFE-covered temperature sensors and inserted at the counter electrode compartment entrance (11) and exit (10) as well as in the working electrode compartment entrance (12) and exit (13).

3.2 Oxygen reduction

For the oxygen reduction reaction (ORR) measurements, a similar setup to the one for the HCl oxidation was employed. The cell was made of Plexiglas with an electron conductive support (8) made of carbon-polymer composite material BMA5 using PVDF as a binder (Eisenhuth, Germany). The HCl feed was replaced with oxygen (grade 4.5, purity 99.995%).
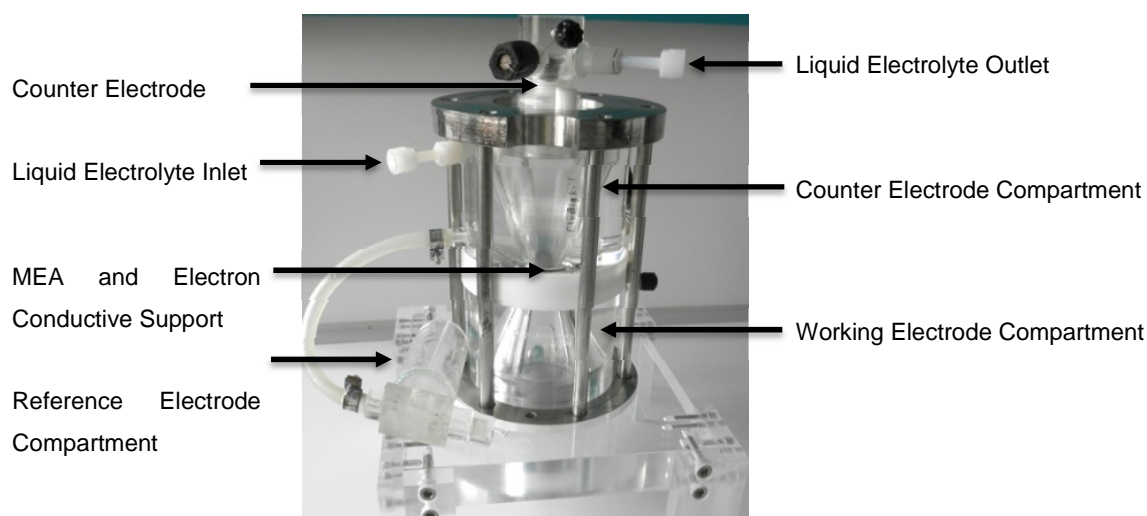
Figure 3-3 Cyclone flow cell for the ORR.

4   MEA preparation

4.1   Electrocatalysts

Several catalysts were tested for the HCl oxidation: unsupported platinum (Johnson Matthey, UK), Vulcan XC72R (Cabot Inc., USA), supported Pt/C (Johnson Matthey, UK), and supported Pt/C (BASF, Germany). All catalysts were employed as received.

4.2   MEA preparation

MEAs were prepared according to the airbrush spraying method [30-32]. MEAs employed in this work consisted of a GDL, a catalyst layer (CL) and a proton exchange membrane.
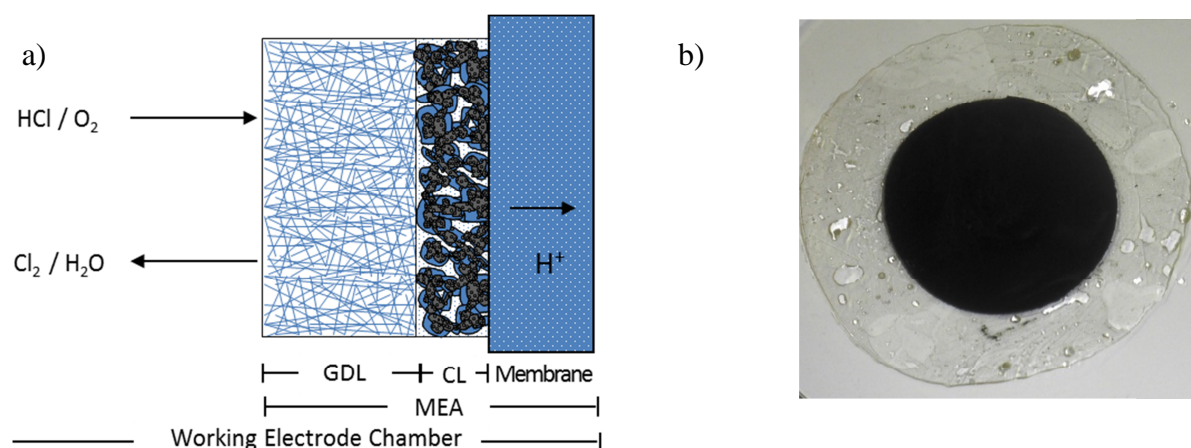

Figure 4-1 a) Schematic representation of a MEA for the half-cell experiments; b) real MEA.

The GDL provided electric contact with the current collectors and structural support to the MEA. GDLs employed were prepared in the TU Clausthal. AvCarb1071HCB carbon cloths (Ballard, Canada) were airbrush sprayed with a Hostaflon PTFE suspension (Dyneon, Germany), and afterwards with EC300J Ketjen Black (Akzo Nobel, Netherlands) suspended with 20 wt% PTFE up to a loading of 4.5 mg cm^{-2}. The treated cloth was pressed with 62 kg m^{-2} for 3 minutes and sintered in an oven for 2 hours at 335°C to improve the homogenization of the layers.

Nafion 117 membranes were employed in this work. Membranes were first cleaned by cooking them for 1 hour at 80°C in water, then 1 hour in a 3% H_2O_2 solution, and again 3 hours in water. Afterwards membranes were protonated by cooking them 1 hour in 1M sulfuric acid followed by three hours in water in order to remove remaining acid.

The catalyst ink was prepared by mixing an appropriate amount of catalyst and a 15% Nafion solution (1:1 weight ratio water:isopropanol) using an overhead mixer for 15 minutes and then dispersing it in an ultrasound bath for 5 minutes. The ink was immediately airbrushed up to the desired loading over the membrane, which was fixed to a metal frame at 120°C. The sprayed membrane was pressed for 3 minutes with 90 kg cm^{-2}. The geometrical area of the CL was 2 cm^2.

The finished MEA was created by simply overlaying the catalyst-sprayed membrane and the GDL in the cyclone flow cell. The MEA was kept pressed together in order to have good electrical

contact between the CL and the GDL with help of the conductive support and the PTFE disk described in section 3.1. The cyclone flow cell was tightened with a torque of 8 Nm.

4.3 MEA characterization methods

4.3.1 BET measurements

The surface area of all catalysts was measured by the Brunauer–Emmett–Teller theory (BET) and the t-plot method with a Nova 2000e (Quantachrome Instruments, USA) in the range of 0.05-0.35 p/p°. Nitrogen was employed as adsorbate.

4.3.2 DLS measurements

Particle size distribution was analyzed by Dynamic Light Scattering (DLS) [33]. Catalyst inks were treated by ultrasound for 5 minutes and measured with a Mastersizer 2000 (Malvern Instrument, UK).

4.3.3 CV measurements

Cyclic voltammetry was employed to characterize MEAs with 0.5 mg cm^{-2} platinum and Nafion loadings from 0.5-2.0 mg cm^{-2}. Measurements were done under nitrogen atmosphere at 60°C in 1M deaerated sulfuric acid as supporting electrolyte with a Solarton 1286 potentiostat. Results were normalized by dividing the current by the Nafion loading in the MEA.

4.3.4 Rotating disk electrode measurements

Catalyst inks prepared according to the procedure presented in chapter 4.2 were employed to coat rotating disk electrodes and achieve the same loadings as for MEAs used in linear sweep measurements. ORR experiments were carried out at 25°C with oxygen-saturated 1M sulfuric acid as electrolyte. Electrolyte saturation was achieved by constantly bubbling oxygen into the electrolyte. Electrodes were preconditioned by CV between 0.2-1.0 V vs. Ag/AgCl with a sweep rate of 50 mV s^{-1} for 10 cycles controlled with a Solarton 1286 potentiostat. Linear sweeps were done in a range between 0.85-1.05 V vs. Ag/AgCl with a sweep rate of 1 mV s^{-1}.

4.3.5 Linear sweep measurements

MEAs were preconditioned by CV between 0.2-1.0 V vs. Ag/AgCl with a sweep rate of 50 mV s^{-1} for 10 cycles controlled with a Solarton 1286 potentiostat. Due to the distance between the Luggin capillary and the CL, potential was corrected via the current interrupt method. Linear sweeps were done in a range between 0.85-1.05 V vs. Ag/AgCl with a sweep rate of 1 mV s^{-1}. Before each temperature change, a linear sweep with nitrogen was recorded and employed as a base line correction for all further measurements. Baseline corrections had current densities below 13 mA cm^{-2} or 7% of the maximal measured current. Results in this work are the average of at least three measurements.

5 Half-cell measurements

5.1 MEA characterization

MEAs with a constant platinum loading of 0.5 mg cm^{-2} and variable Nafion loadings from 0.5-2.0 mg cm^{-2} were investigated by cyclic voltammetry. As presented in Figure 5-1a, characteristic polycrystalline platinum features (hydrogen adsorption/desorption at lower potentials, oxide formation/reduction at higher potentials, see Figure 5-1b) were clearly defined only for the MEA with the lowest Nafion loading. CVs become more featureless with increasing Nafion loading, exhibiting also higher currents. This was attributed to the rise of the double layer capacitance due to an enhancement of the Nafion/carbon interface. This could arise from different GDL surface areas in contact with Nafion (probably due to hot-pressing or different Nafion distribution in the CL at higher Nafion contents). The peak at 0.65 V, characteristic of the quinone/hydroquinone redox couple in Vulcan XC72R [34] supports this statement, as it is more pronounced at higher Nafion loadings. Another reason could be the possible reduction of available platinum surface area when Nafion is present. Changes in platinum active surface area in the presence of Nafion have been reported to be up to 15% lower than bare platinum [35].
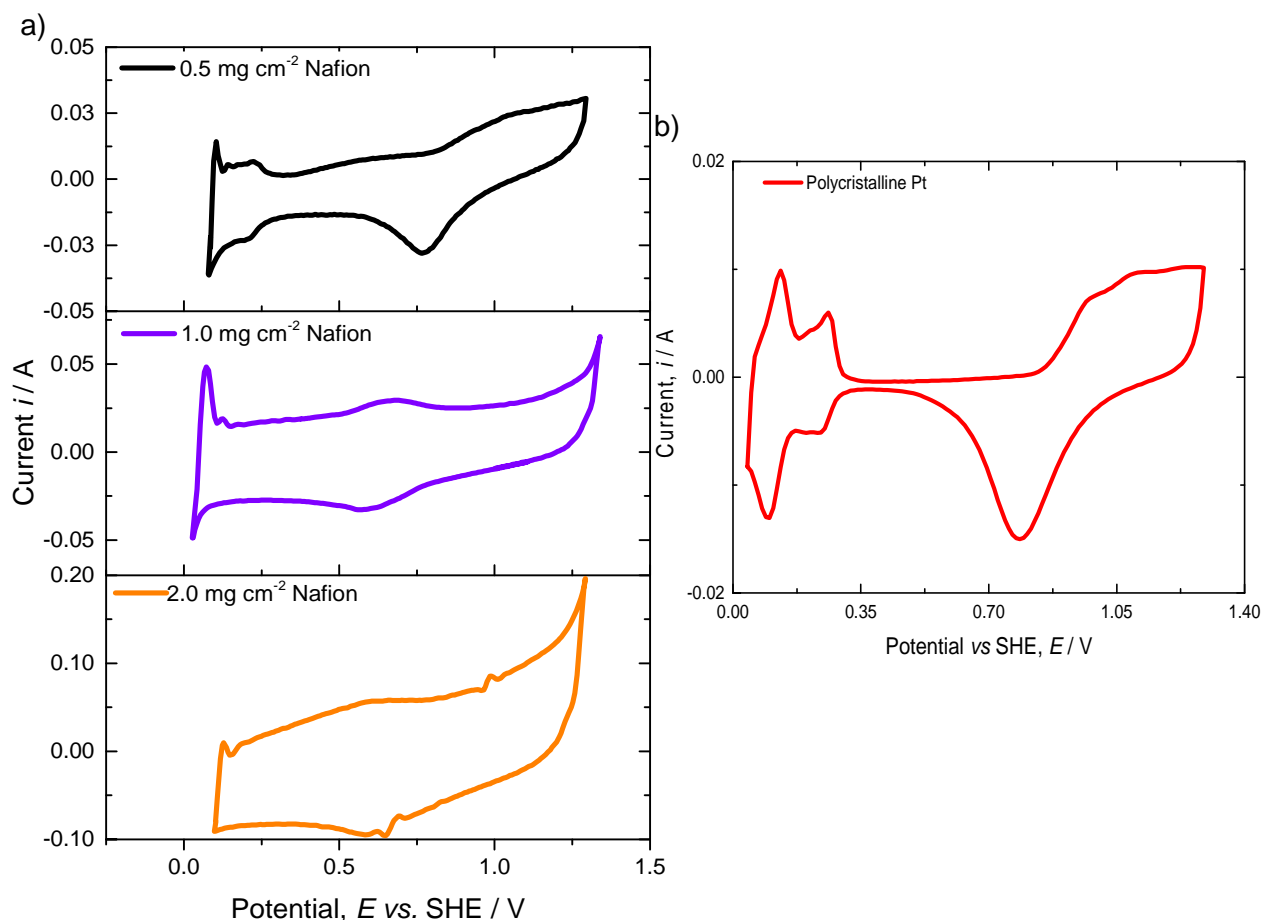

Figure 5-1 a) CVs for a) MEAs with 0.5 mg cm^{-2} platinum normalized to Nafion loading; b) Polycrystalline platinum. Conditions: 60°C, electrolyte: 1M sulfuric acid, sweep rate: 50 mV s^{-1}.

The effect of Nafion loading in GDEs has been extensively investigated in literature. Some authors show an increase in total current with increasing Nafion loading [36, 37], as seen in this work, while others report an optimal Nafion loading [38, 39].

The electrochemical surface area per unit platinum can be calculated from the amount of charge exchanged during the electro-adsorption and desorption of protons on platinum. The procedure explained by Vidaković [40] was followed for the MEA with 0.5 mg cm^{-2} Nafion. It is important to mention that the peaks observed at the leftmost part of the CV were not taken into account as they arise from the oxidation of molecular hydrogen in the liquid electrolyte formed during the backward sweep of the CV. This yielded a specific electrochemically active surface area of 32 m^2 gr Pt^{-1} or an electrochemically active-to-geometrical surface area ratio of 1560 for the MEA with lowest Nafion loading.

In comparison, current state-of-the-art DSAs offer an active surface area around 10-1000 times greater than their geometrical surface area [15], which shows that the use of GDEs can improve catalyst utilization up to 350%.

5.2 Steady state vs. Quasi-steady state measurements

For the HClOR, steady state measurements were compared with quasi-steady state measurements. For the former ones the potential was hold for 5 minutes after which the current was recorded, for the latter ones a constant slow sweep rate of 1 mV s^{-1} was used.

Quasi steady state measurements provided more points along the polarization curve without noticeable deviation from steady state measurements, as shown in Figure 5-2 (typical polarization curve for the HClOR). Therefore they were used for the investigations presented in this work.
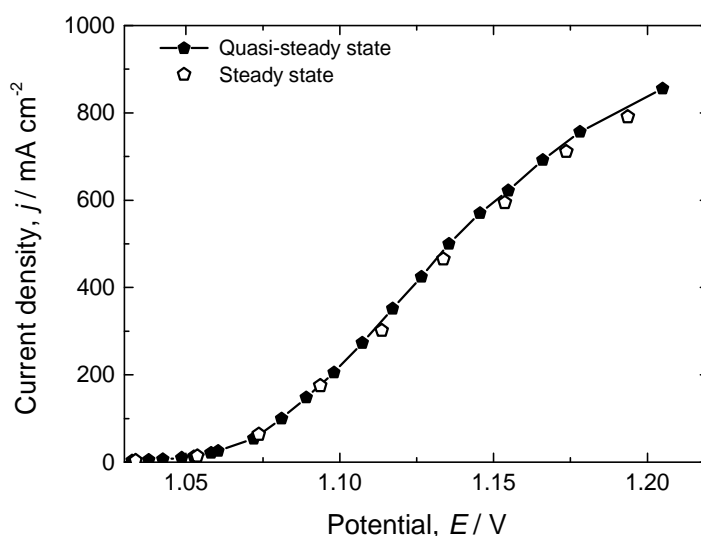

Figure 5-2 Steady-state vs. Quasi-steady-state measurements for a MEAs with 0.5 mg cm^{-2} platinum and 1.0 mg cm^{-2} Nafion at 60°C.

5.3 Anodic measurements

5.3.1 Effect of different catalysts

It is known different catalysts, such as platinum, ruthenium, and their oxides as well as carbon show activity for the HClOR [4, 14, 41-43]. There is still a strong discussion regarding platinum stability in the presence of chloride ions and chlorine, as it may complex to chloroplatinic acid in the presence of HCl and chlorine:

$$\text{Pt} + 2\text{Cl}_2 + 2HCl \rightarrow H_2PtCl_6 \qquad\qquad (5\text{-}1)$$

Kim *et al.* [44] reported that platinum dissolves in the presence of chlorine only in hydrochloric acid solutions with a concentration higher than 3M. For the half-cell experiments realized throughout this work (duration around 6 hours and 10 shutoff sequences), no substantial decrease in platinum activity was observed at a constant temperature, even though potentials up to 1.2 V were applied. The project partners from the TU Clausthal operated a reactor (anodic HClOR and cathodic ORR) for periods of 10 hours without noticing platinum dissolution or deactivation, reaching cell potentials of up to 1.6 V and more than 10 shutoff sequences.

In order to separately assess the range of potential where Vulcan XC72R and platinum have activity for HClOR, MEAs with platinum supported on Vulcan XC72R (Pt/C), unsupported platinum (Pt), and Vulcan XC72R were tested with 100% hydrogen chloride (Figure 5-3a). These catalysts were also analyzed by BET to determine their surface area. Unsupported platinum catalyst had a specific surface area of 24 m^2 g^{-1} while Vulcan XC72R had 202 m^2 g^{-1}. Platinum supported on Vulcan XC72R had a surface area of 116 m^2 g^{-1}.

Industrially relevant current densities (300-400 mA cm^{-2}) were reached by all tested catalysts at 60°C. MEA's with Pt/C catalysts reached the highest current densities in the entire potential range followed closely by the MEA with unsupported Pt, which showed an anodic shift of *ca.* 10 mV at potentials below 1.17 V. Even though current density differences between MEAs with supported and unsupported catalysts didn't exceed 25%, the loading of the latter was 4 times higher (2.0 mg cm^{-2}) than that of the former one (0.5 mg cm^{-2}). This points to a better catalyst utilization by using a support, as confirmed in literature and our BET measurements [30, 45]. This results in better platinum particle dispersion, and consequently an increased surface area which prevents agglomeration. The MEA with only Vulcan XC72R starts to show activity at potentials more positive than 1.13 V and exceed current densities of 300 mA cm^{-2} at potentials above 1.18 V. This corresponds to overpotentials at least 100 mV higher than those of supported and unsupported platinum catalysts. These results indicate that the HClOR occurs on supported Pt/C catalysts only on the platinum surface at low potentials, while at potentials above 1.13 V the reaction might happen simultaneously on the platinum and carbon surfaces. Nevertheless, at 400 mA cm^{-2} and 60°C, Vulcan XC72R contributes roughly with 7% of total current density compared to the Pt/C catalyst. This estimation is based on the assumption that current density generated at a

given loading of pure Vulcan XC72R is equal to the current density produced at the same loading of Vulcan XC72R contained in Pt/C supported catalyst at a given potential.

To better assess catalyst utilization total current was divided by the total catalyst mass obtaining the specific current i (Figure 5-3b). Unsupported platinum shows the lowest current density, followed by supported platinum. Results for the supported catalyst reached current densities similar to the ones reported by Eames and Newman [10]. However, applied potentials in this work were *ca.* 200 mV lower, which can be possibly attributed to a better MEA structure and the fact that in our set-up potential losses associated to the cathode and membrane could be taken out.
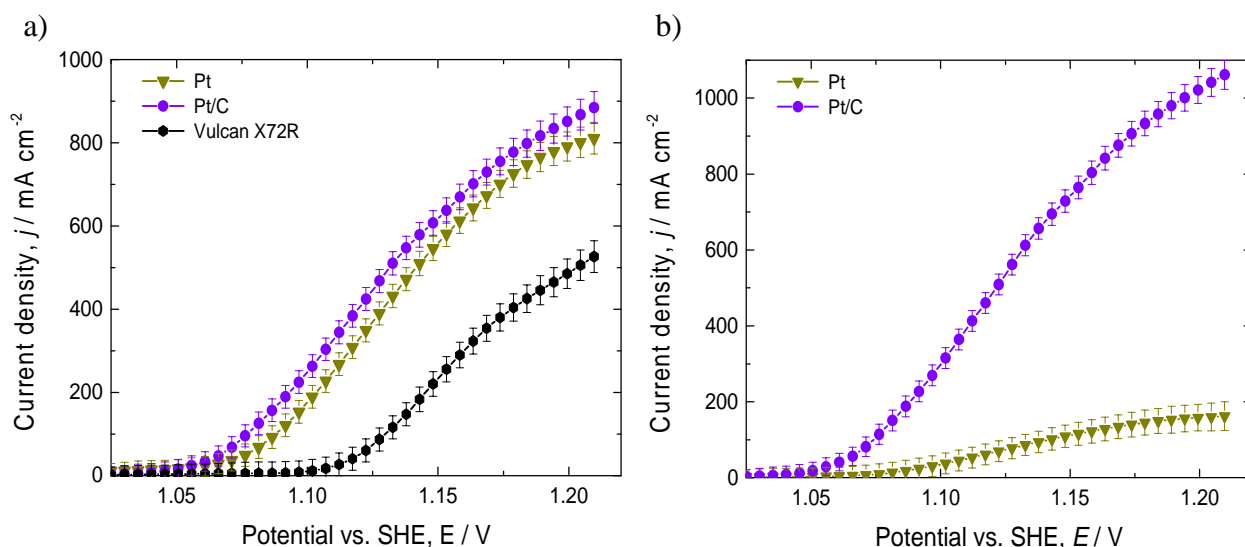

Figure 5-3 Influence of the catalyst type on HClOR activities expressed in terms of: a) current density; b) specific current. Catalyst loadings. Unsupported Pt: 2.0 mg cm⁻² Pt and 1.1 mg cm⁻² Nafion. Supported Pt: 0.5 mg cm⁻² Pt, 1.0 mg cm⁻² Vulcan XC72R, and 1.0 mg cm⁻² Nafion. Vulcan X72R: 0.7 mg cm⁻² Vulcan XC72R and 0.8 mg cm⁻² Nafion. Conditions: 60°C, 101.3 kPa, hydrogen chloride concentration 100%, hydrogen chloride flow rate: 500 ml min⁻¹.

Due to the different phenomena occurring in the MEA, experimentally measured current density j_{ex} can be expressed as a function of diffusion, chemical and electrochemical terms [46]:

$$\frac{1}{j_{\text{ex}}} = \frac{1}{j_{\text{df}}} + \frac{1}{j_{\text{rx}}} + \frac{1}{j_{\text{kn}}} \qquad (5\text{-}2)$$

In order to analyze the Tafel plots of the investigated MEAs, only the kinetic current density j_{kn} is of interest. As diffusion and chemical reaction limitations can't be clearly separated, current density was corrected according to the following equation:

$$j_{kn} = \frac{j_{(\text{df,rx})}\, j_{\text{ex}}}{j_{(\text{df,rx})} - j_{\text{ex}}} \qquad (5\text{-}3)$$

Tafel slopes of ca. 30 mV (Figure 5-4) at low current densities were observed for all catalysts. Values between 30-40 mV have been associated to either difficult chlorine removal from the electrode surface or to chloride absorption from the solution [41], which limits the amount of active sites available for the reaction.

The Tafel slope doubles at higher potentials pointing to a possible change in surface coverage on the electrode. MEA porosity also affects the Tafel slope, as shown by Banham and Soderberg [47], with variations up to ±10 mV depending on pore size.
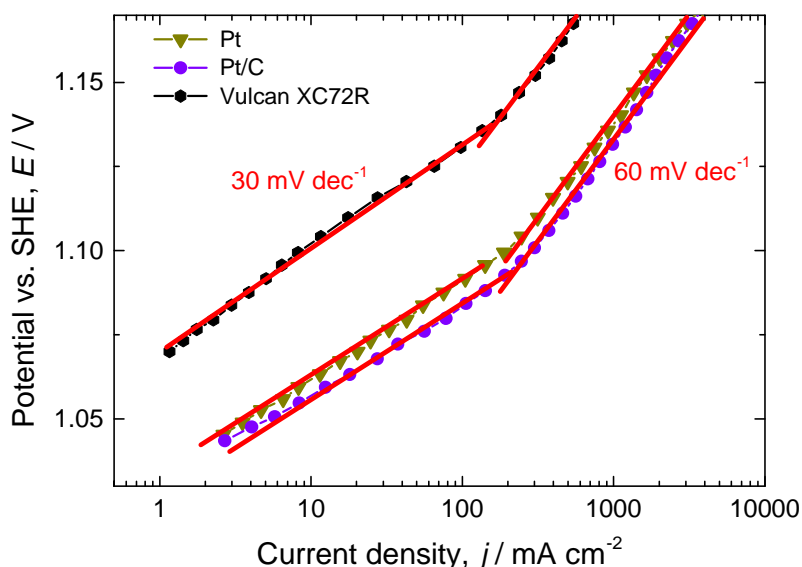
Figure 5-4 Tafel plot for the HClOR on different catalysts. Conditions as in Figure 5-3.

5.3.2   Effect of platinum loading

The effect of the platinum loading was investigated on MEAs with 0.2, 1.0, and 2.0 mg cm^{-2} at a constant Nafion loading of 0.5 mg cm^{-2}. An initial increase of platinum loading from 0.2 to 1.0 mg cm^{-2} improves MEA performance at potentials above 0.975 V (Figure 5-5a). Nevertheless, a further increase from 1.0 to 2.0 mg cm^{-2} shows no remarkable enhancement but a decrease in performance at lower potentials.
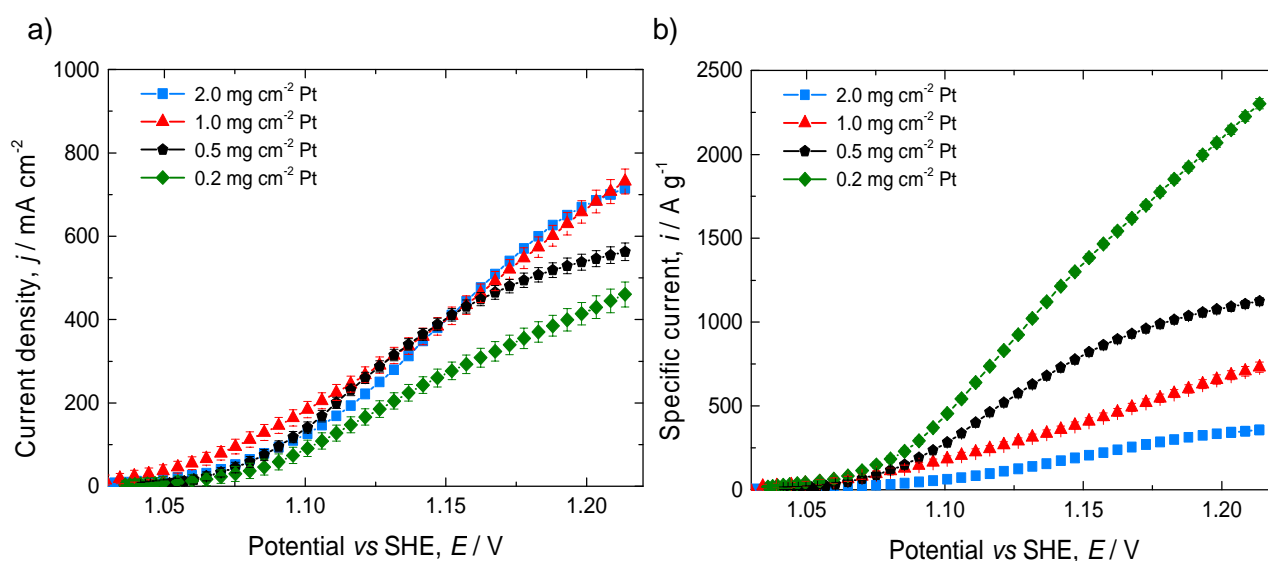
Figure 5-5 a) Polarization curve for MEAs with constant Nafion loading of 0.5 mg cm^{-2} and varying platinum loadings; b) specific current. Conditions as in Figure 5-3

The worst overall performance was shown by the MEA with the lowest platinum loading (high Nafion content, 60 wt%). It is important to remark that the total number of active sites in these experiments is changing, and a decrease of activity with a decrease of the total number of active sites can be expected. This behavior was observed for the platinum loading range from 0.2-1.0 mg cm$^{-2}$. Another important criterion for judging MEA activity is catalyst utilization. To better visualize this, current density in Figure 5-5a was divided by platinum loading, resulting in the specific current i, presented in Figure 5-5b.

This normalization resulted in an inverse dependence between i and Nafion content, where the MEA with the lowest platinum loading (highest Nafion content) showed the best performance. This dependence points to a catalyst utilization improvement with higher Nafion/platinum ratios.

5.3.3 Effect of Nafion loading

MEAs with a constant platinum loading of 0.5 mg cm^{-2} and varying Nafion loadings of 0.5, 1.0, and 2.0 mg cm^{-2} were investigated. Polarization curves are shown in Figure 5-6a, where all MEAs reached technical current densities (300-400 mA cm^{-2}) at potentials below 1.17 V. Optimization of the Nafion loading results in an overpotential decrease of *ca.* 40 mV between MEAs with highest and lowest Nafion loadings at 400 mA cm^{-2}. Although small, this difference accounts for 21% of the total potential window investigated, showing its importance for process optimization.

With a constant platinum loading the number of active sites remains unchanged allowing to analyze catalyst utilization directly from Figure 5-6a. It is observed that the MEA with the highest Nafion loading attains the best performance at current densities up to 360 mA cm^{-2}; at current densities higher than 800 mA cm^{-2} the MEA with 1.0 mg cm^{-2} performs better.
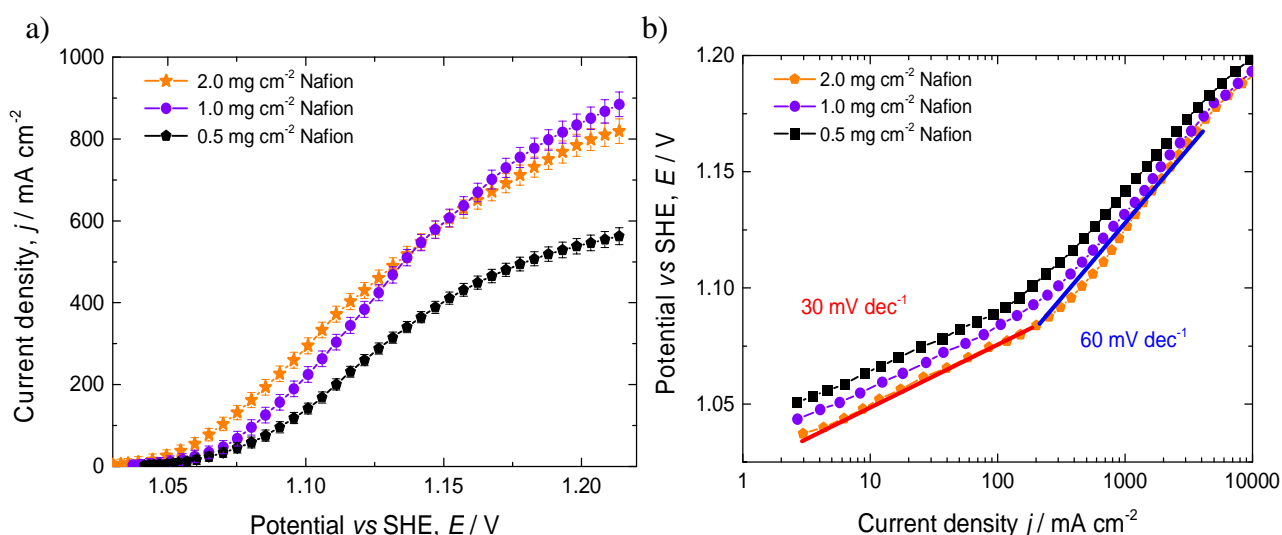

Figure 5-6 a) Polarization curve for MEAs with constant platinum loading of 0.5 mg cm^{-2} and varying Nafion loading; b) Tafel plot. Conditions as in Figure 5-3.

Between 360 and 800 mA cm^{-2} there is no considerable difference between MEAs with 1.0 and 2.0 mg cm^{-2} Nafion. The MEA with the lowest Nafion loading, 0.5 mg cm^{-2} showed the worst

performance in the entire potential range. From the Tafel plot in Figure 5-6b it is observed that the Tafel slope for the different MEAs attained values between 31-36 mV dec^{-1} at low current densities (<100 mA cm^{-2}), close to the expected value of 30 mV dec^{-1} on platinum for chloride oxidation [41].

To better understand the role of Nafion, the dependences of specific currents at two potential values, 1.098 and 1.175 V, are shown in Figure 5-7. At lower potentials, specific current increases with Nafion content. At higher potentials, lower Nafion contents perform better. This dependency qualitatively corresponds to literature results for other gas phase reactions [48, 49]. The use of very high Nafion loadings is discouraged due to an increase of the mass transport resistance. Very low loadings are also avoided due to incomplete platinum particle coverage and higher tortuosity of the ionic transport network. These dependencies yield a bell shaped correlation of specific current to Nafion content at higher potentials, as shown in Figure 5-7. This can be attributed to an increase in mass transport resistance at Nafion contents above *ca.* 60 wt%, value considerably higher than those of other gas phase reactions such as the ORR. At low potentials, mass transport doesn't pose a high resistance due to the low reactant consumption, therefore no maximum is observed.
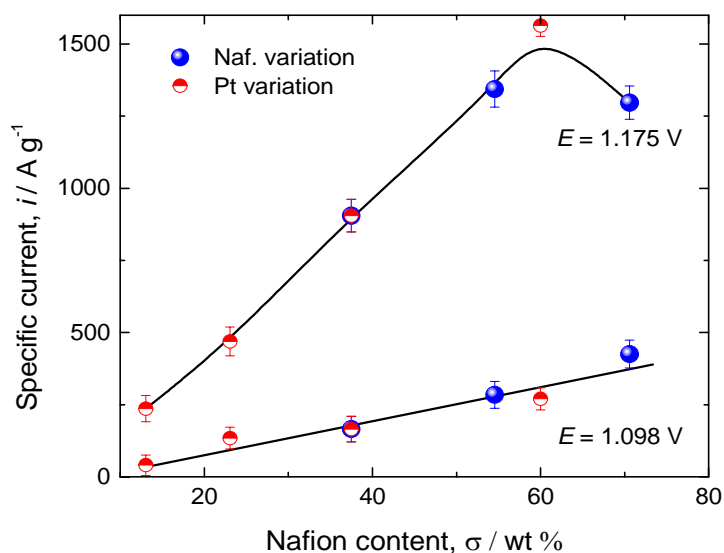
Figure 5-7 Dependence of the specific current for the HClOR on Nafion content at two different potential values. Condition as in Figure 5-3

In literature it has been reported that at high Nafion contents the ORR activity is reduced [37], which was also observed in this work (section 5.4.1). This is commonly attributed to a higher mass transport resistance of the gaseous reactant through the Nafion film around the catalyst. A reason why this was not observed for the HClOR could be the higher HCl solubility in Nafion and/or higher diffusion coefficient through Nafion compared to oxygen. The gaseous HCl diffusion coefficient in Nafion hasn't been reported, but information about the aqueous HCl diffusion coefficient through Nafion membranes is available. Comparison of the oxygen and aqueous HCl diffusion coefficients in Nafion shows that the latter one is 10 times larger than the former one, $4.52 \cdot 10^{-11}$ m^2 s^{-1}, compared to $3.80 \cdot 10^{-12}$ m^2 s^{-1} [25, 50]. Nevertheless, HCl absorbs in Nafion up to 8.70 mol% compared to 0.01 mol% for oxygen [51, 52].

Therefore, it might be the case that strong HCl absorption overwhelms its slow diffusion, leading to a better performance at higher Nafion loadings than the ORR. Unlike oxygen, hydrogen chloride absorbs chemically in water forming hydrochloric acid, a very exothermic process (heat of absorption ~2000 kJ kg^{-1} HCl [53]), which could lead to water evaporation. Thus, it is possible that higher Nafion contents contribute to better water preservation in the CL and therefore higher ionic conductivity.

Another reason why the activity of MEAs changes with different Nafion loadings could be a Nafion loading dependent agglomerate radius, and subsequent thickness of the Nafion layer surrounding the agglomerate. In order to get a better insight into this hypothesis, the effect of the Nafion/catalyst ratio on the organization of agglomerates was investigated with dynamic light scattering (DLS) experiments. Catalyst inks were prepared with different Nafion to catalyst ratios using two platinum loadings, 0.5 and 1.0 mg cm^{-2}, together with low and high Nafion loadings, 0.5 and 2.0 mg cm^{-2}. As shown in Figure 5-8, higher Nafion to catalyst ratios contribute to better catalyst dispersion, seen through the formation of smaller agglomerates. This was notorious at the higher platinum loading where an increase of Nafion to catalyst ratio resulted in a decrease of agglomerate size from 2.0 to 0.7 µm. At a constant Nafion loading of 0.5 mg cm^{-2}, catalyst dispersion was much better for inks containing lower catalyst loadings, agglomerate size of 1.2 µm, compared to an agglomerate size of 2.0 µm at higher platinum loading.
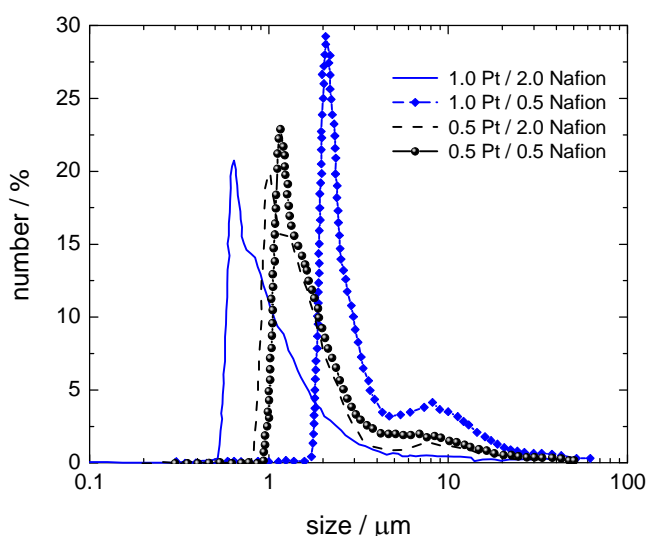
Figure 5-8 DLS measurements of catalyst inks with different compositions.

Different agglomerate structures could also be attributed to the higher affinity of Nafion to carbon than to platinum [6, 54]. In addition, the particle size of carbon is at least one order of magnitude larger than platinum, making it more accessible for Nafion to cover it. This results are in accordance to the polarization curves presented in chapter 5.3.3, where an increase of the Nafion loading (or Nafion/Pt ratio) improved current density considerably (Figure 5-6a, 2.0 and 1.0 mg cm^{-2} compared to 0.5 mg cm^{-2}). This could be attributed to more active sites being easily available due to the increased surface area of the agglomerates.

5.3.4 Effect of Temperature

The effect of temperature was investigated on a MEA with 0.5 mg cm^{-2} platinum and 1.0 mg cm^{-2} Nafion at temperatures of 25, 40, 50 and 60°C, as shown in Figure 5-9a. The highest attainable current densities varied almost linearly with increasing temperature. Electrode activity showed a considerable increase from 50 to 60°C at current densities lower than 400 mA cm^{-2}.

Tafel plots are presented in Figure 5-9b for all investigated temperatures. In experiments, Tafel slopes were found to be 39, 36, 35, and 33 mV dec^{-1} for 25, 40, 50, and 60°C. Tafel slopes were found to be inversely proportional to the temperature.

Regarding the issue of the reaction taking place in the gas or liquid phase (section 2.2), it is observed that the change in the measured open circuit potential is only *ca.* 3 mV. Analyzing the predicted change in reversible electrode potential, eq. (2-18) for the gas phase and (2-19) for the liquid phase reactions, values of 3 and 16 mV are obtained. This supports the theory of having a reaction directly from the gas phase rather than from the liquid phase.
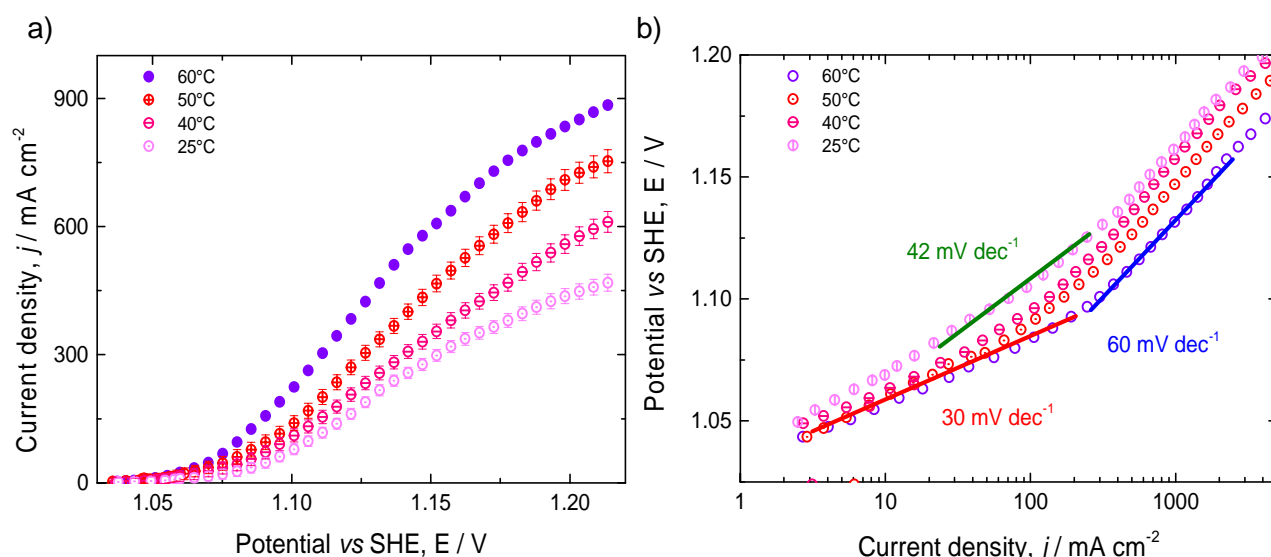
Figure 5-9 a) Polarization curve for a MEA with 0.5 mg cm^{-2} and 1.0 mg cm^{-2} Nafion loading at different temperatures; b) Tafel plot. All other conditions as in Figure 5-3.

5.3.5 Effect of Concentration

The effect of concentration to the HClOR was measured at 60°C for hydrogen chloride concentrations of 100, 80, 60, 40, and 20%. Results are presented in Figure 5-10. It is observed that the difference in current density is greater when reducing hydrogen chloride concentration from 100 to 80% than between any other concentration change, especially in the range of 1.07-1.17 V. Furthermore, as expected, lower current densities were recorded at lower hydrogen chloride concentrations along the entire potential range. At 20% hydrogen chloride concentration a limiting current density plateau was clearly reached.

According to the Nernst equation, eq. (2-14), a change in hydrogen chloride concentration from 100 to 20% produces a reversible potential loss of 46 mV. Losses observed in our

experiments are in the range of 60-70 mV. Tafel slopes are presented in Figure 5-10b, where it is observed that values of 30 and 60 mV dec^{-1} were attained at low and high potentials respectively.
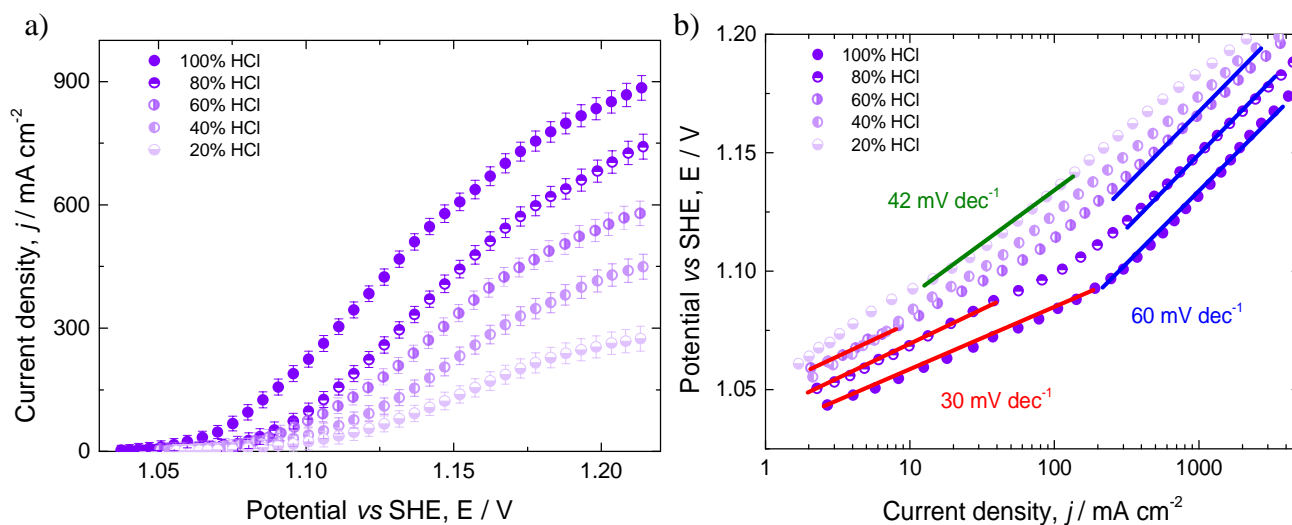
*Figure 5-10 a) Polarization curve for a MEA with 0.5 mg cm^{-2} and 1.0 mg cm^{-2} Nafion loading at different hydrogen chloride concentrations; b) Tafel plot. All other conditions as in Figure 5-3.*

For concentrations of 60% and lower, a transitional Tafel slope of *ca.* 42 mV dec^{-1} was observed, whose potential range increased with decreasing hydrogen chloride concentration.

5.3.6 *Apparent kinetic parameters*

The use of the cyclone cell allows to clearly determine the effect of the external mass transfer to the MEA (between hydrodynamic diffusion layer, HDL, and MEA), but not to separate kinetic currents from internal mass transport effects in the MEA. Because of this, parameters determined in the next sections are apparent, not purely kinetic, and include the effect of the electrode structure such as porosity, internal mass transport, catalyst distribution, etc.

5.3.6.1 Possible reaction mechanisms for the HClOR

The only proposed mechanism for the gaseous HCl oxidation was suggested by Eames and Newman [10] as a Heyrovsky-Tafel (HT) mechanism, eq. (5-4) and (5-5).

Heyrovsky
$$HCl + Pt \rightleftharpoons PtCl + H^+ + e^- \qquad (5\text{-}4)$$

Tafel
$$2PtCl \rightleftharpoons 2Pt + Cl_2 \qquad (5\text{-}5)$$
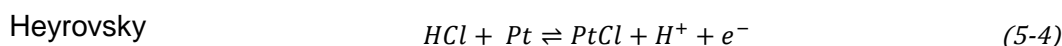
Another possible reaction pathway is the Heyrovsky-Volmer (HV) mechanism, in which both steps are electrochemical, eq. (5-6) and (5-7):

Heyrovsky
$$HCl + Pt \rightleftharpoons PtCl + H^+ + e^- \qquad (5\text{-}6)$$

Volmer
$$HCl + PtCl \rightarrow Pt + Cl_2 + H^+ + e^- \qquad (5\text{-}7)$$
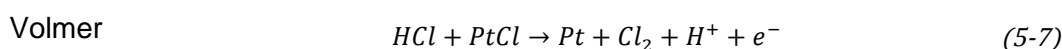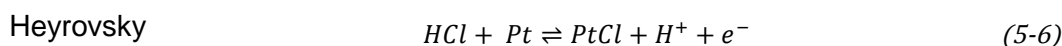
Also possible would be to have the Heyrovsky reaction as the first step followed by the Volmer and Tafel reactions in parallel, a Heyrovsky-Volmer/Tafel mechanism (HVT), as hinted by O'Brien *et al* [4]. These four equations can also be proposed for the HClOR from the liquid phase, replacing

HCl with Cl$^-$ and eliminating the proton terms. Therefore, the kinetic analysis to follow is valid for both, chlorine evolution from hydrogen chloride or from hydrochloric acid.

Expressions for current density were calculated for each of the mechanisms assuming one of the reactions to be the rate determining step (*r.d.s.*) and the other to be in quasi-equilibrium. For electrochemical reactions, the *r.d.s.* was defined based on the Tafel equation. Adapting the kinetic analysis presented by Gileadi [55] for the HT mechanism, it was assumed that the adsorption of HCl on platinum (Heyrovsky reaction) could be described by the Frumkin isotherm at all surface coverages [55], eq. (5-8).

$$\frac{\theta}{1-\theta} exp\left(\frac{\epsilon\theta}{RT}\right) = k_o c_{HCl} \, exp\left(\frac{zF}{RT}\eta\right) \tag{5-8}$$

where k_o represents the kinetic constant and z the exchanged electrons in the *r.d.s.*, θ coverage of the adsorbed PtCl species and ϵ a lateral interaction factor. Ignoring the preexponential term in eq. (5-8) results in the Temkin isotherm. The kinetic equation based on the *r.d.s.* (Tafel reaction) was then formulated:

$$r = k_T \theta^2 \, exp\left(\frac{2\beta\epsilon\theta}{RT}\right) \tag{5-9}$$

Substituting the exponential term from the Temkin isotherm yields the total reaction rate for the HT mechanism:

$$r = k_T K_H^{2\beta} c_{HCl}^{2\beta} \, exp\left(\frac{2\beta zF}{RT}\eta\right) \tag{5-10}$$

Leading to an expression for total current density j:

$$j = 2F k_T K_H^{2\beta} c_{HCl}^{2\beta} \, exp\left(\frac{2\beta zF}{RT}\eta\right) \tag{5-11}$$

Analogous formulations for the other mechanism were formulated to obtain the theoretical reaction orders and Tafel slopes in the next sections.

5.3.6.2 Reaction order

Reaction order n was determined from the slope of a plot of the natural logarithm of the kinetic current against the natural logarithm of the gas phase mole fraction, presented in Figure 5-11a.

The points followed a linear trend up to mole fractions of 80%, yielding reaction orders of 0.82±0.07, 1.07±0.09, and 0.97±0.07 at potentials of 1.065, 1.095, and 1.155 V. The first two potential values are found in the Tafel slope region of 30 mV dec^{-1}, while the third one in the 60 mV dec^{-1} region. The value at 100% concentration clearly didn't follow the trend and was left out of the calculation.

Assuming the reaction takes place in the liquid phase, HCl concentration can be replaced with chloride ion activities, yielding a better linear fit along the entire range (Figure 5-11b). Values obtained were 1.27±0.06, 1.29±0.07, and 0.98±0.12 at potentials of 1.065, 1.095, and 1.155 V respectively.
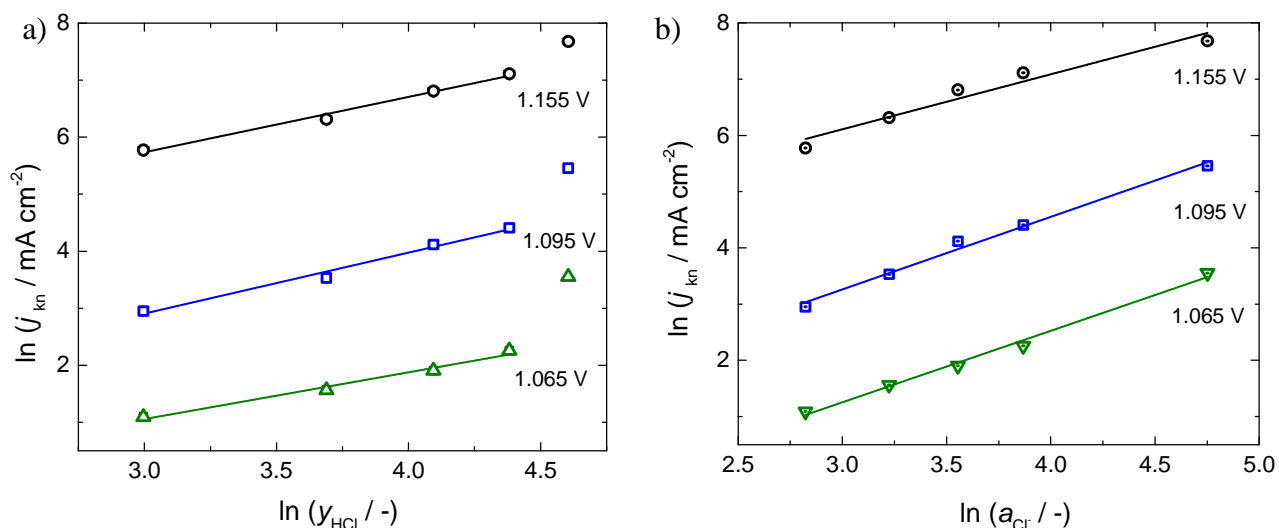
Figure 5-11 Apparent reaction order with respect to a) HCl concentration; b) Cl- activity for a MEA with 0.5 mg cm^{-2} platinum and 0.5 mg cm^{-2} Nafion. Conditions as in Figure 5-10.

Comparing the values from Figure 5-10b to the theoretically expected reaction orders from the kinetic analysis (Table 5-1), it is possible to explain the reaction order with the HV mechanism at high surface coverages or the HT mechanism at intermediate surface coverages.

Table 5-1 Reaction orders for the different r.d.s. of the mechanisms proposed

Mechanism	r.d.s.	$\theta \approx 0$	$0.2 < \theta < 0.8$	$\theta \approx 1$
Heyrovsky Volmer	Volmer reaction	2.0	1.5	1.0
Heyrovsky Tafel	Tafel reaction	2.0	1.0	-

The shift in reaction order can be due to the change of surface coverage with potential, as observed between 1.095 and 1.115 V. Another possible cause for the deviation of the reaction order from unity is the formation of platinum oxide, expected at potentials around 1.0-1.1 V [56], which would yield a potential dependent catalytic surface. Oxide formation could be shifted to even lower potentials in the presence of complexing agents like chloride ions. Potential-dependent apparent reaction orders have been previously reported for other anodic reactions involving chlorides [57] as well as cathodic reactions [58, 59]. Platinum oxide is thermodynamically stable at the given potential and acidity conditions. Yet, if platinum particles are small or porous enough [56], the oxide is prone to corrosion, altering the catalytic surface and thus the overall reaction order.

5.3.6.3   Tafel slopes

As shown in previous sections, experimentally observed Tafel slopes were to some extent temperature dependent (Figure 5-9b) and attained values around 30 mV dec^{-1} at low potentials and 60 mV dec^{-1} at higher ones.

Tafel slopes for chlorine evolution from hydrochloric acid, *i.e.* the Bayer-Uhde-Hoechst process, have been reviewed elsewhere, and show similar values: between 28 and 60 mV dec^{-1} along a temperature range of 25-85°C [41]. With help of a kinetic analysis analogous to that

presented in chapter 5.3.6.1, the Tafel slopes for the HT and HV mechanisms were calculated at different surface coverages and presented in Table 5-2:

Table 5-2 Tafel slopes for the different r.d.s. of the mechanisms proposed at 25 and 60°C

Mechanism	r.d.s.	$\theta \approx 0$	$0.2 < \theta < 0.8$	$\theta \approx 1$
Heyrovsky Volmer	Volmer reaction	39-44	60-67	117-131
Heyrovsky Tafel	Tafel reaction	30-32	60-67	∞

Theoretical Tafel slopes reach values between 30-32 mV dec^{-1} for the HT mechanism with limiting Tafel reaction under Langmuir conditions, while values between 60-67 mV dec^{-1} are predicted under Temkin conditions. For the HV mechanism values between 39-44 mV dec^{-1} are predicted at Langmuir conditions while under Temkin conditions values between 60-67 mV dec^{-1} are expected. Considering the low Tafel slope values of 30 mV dec^{-1} observed at high temperatures (50 and 60°C), the HV mechanism is unable to explain them under any surface coverage condition (corresponding Tafel slope values lie around 42-44 mV dec^{-1}). On the other hand, the HT mechanism can explain both observed Tafel slopes of 30 and 60 mV dec^{-1} under Langmuir and Temkin conditions, respectively. Therefore, the choice of the HT mechanism with the Tafel reaction as the *r.d.s.* was considered to be the most appropriate to describe HClOR kinetics. Use of the Temkin isotherm leads to trustable values of both Tafel slope and reaction order in the surface coverage range of 0.2-0.8. Because experimental results can be explained in this range of θ, use of the Temkin isotherm is justified. It is important to mention that theoretical Tafel slope values don't consider structural effects such as pore size and CL resistance (an indirect measure of the Nafion content), which could yield slightly different values than theoretically expected [47].

5.3.6.4 Activation energy

Analogous to the reaction order, apparent activation energy was found to be potential dependent with values around 16-30 kJ mol^{-1} (Figure 5-12a), exhibiting a bell-shaped dependence on potential.
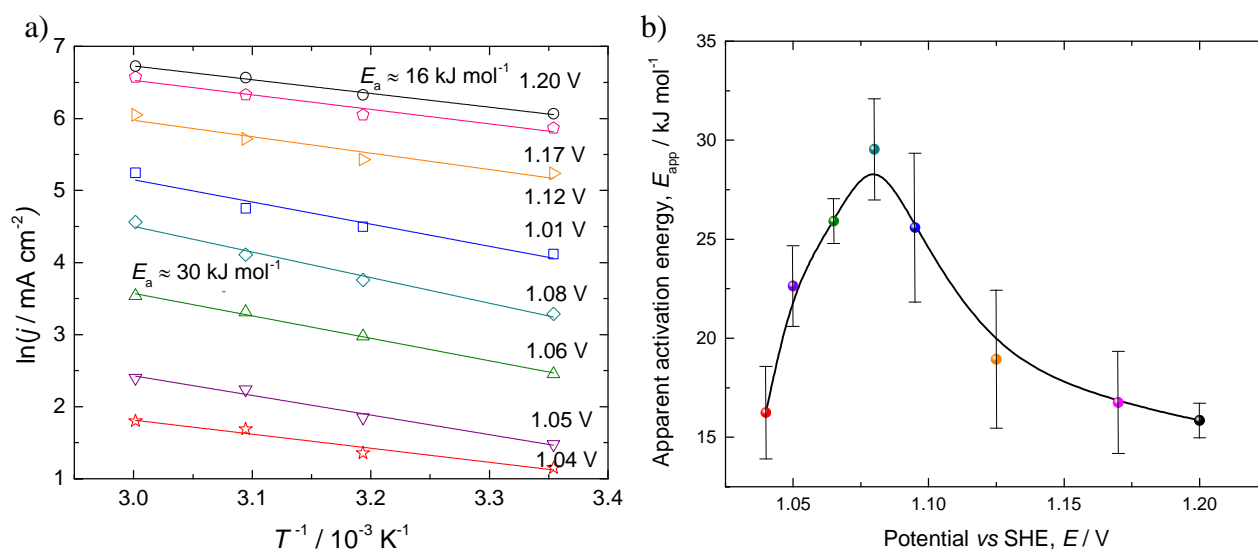
Figure 5-12 a) Arrhenius plot for a MEA with 0.5 mg cm^{-2} platinum and 0.5 mg cm^{-2} Nafion; b) potential dependence of the apparent activation energy. Conditions as in Figure 5-3.

Values went from 16 kJ mol^{-1} at low potentials (<1.05 V) to values of 30 kJ mol^{-1} at medium potentials (1.07-1.10 V) and back again to 16 kJ mol^{-1} at higher potentials (Figure 5-12b).

The increase in activation energy can be attributed to a change in the surface coverage of the platinum surface. The apparent activation energy drops further [60] as the surface coverage remains relatively constant and the effect of the electrochemical activation becomes more pronounced at higher potentials.

5.3.6.5 Exchange current density

Apparent exchange current density j_o was extracted from polarization data presented in the Tafel plots. Commonly, the exchange current density is extracted by extrapolating current density of a Tafel plot at the reversible electrode potential value. In our case, a value for the reversible electrode potential could not be clearly identified, as the question still remains open if the reaction takes place from the gas or liquid phase. Thus, apparent exchange current density was extracted at a value of 1.04 V, the observed open circuit potential. In contrast to the Tafel slope, exchange current density is an extensive parameter and incorporates the MEA active surface area, a function of the platinum and Nafion loadings, and is an indicator of the number of available active sites.
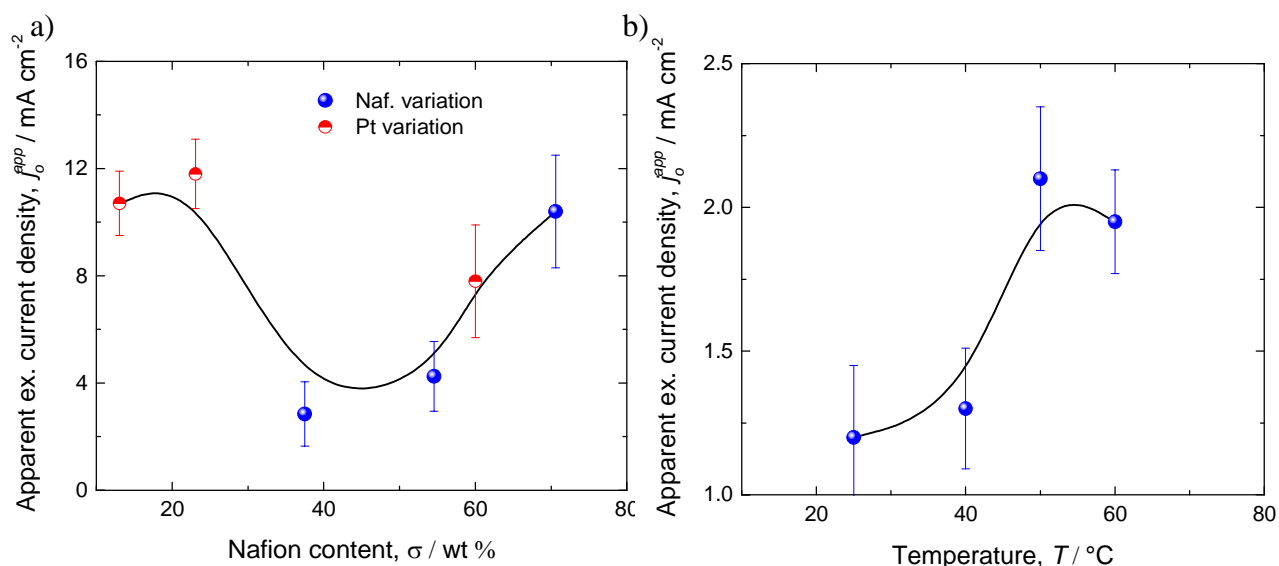
Figure 5-13 Exchange current density as a function of a) Nafion content at 60°C; b) temperature for a MEA with 0.5 mg cm^{-2} platinum and 0.5 mg cm^{-2} Nafion. Other conditions as in Figure 5-3.

For the gaseous HClOR, Eames and Newman [10] didn't explicitly reported exchange current density values but kinetic constants depending on hydrogen chloride partial pressure [10]. When transformed into current density at 40°C and 101.3 kPa HCl pressure, an approximate value of 7 mA cm^{-2} is obtained, which is near the values measured in chloralkali electrolyzers: 8.5 mA cm^{-2} for platinum in 5M NaCl solutions [4]. Nevertheless, it was expected that hydrogen chloride oxidation would proceed with higher exchange current densities than electrolysis from the liquid phase, as the HCl absorption and slow diffusion through the liquid would be substituted by direct reaction of

hydrogen chloride at the catalyst surface. Similar to the results of Eames and Newman, in this work only MEAs with Nafion contents below 30% (platinum loadings above 1.0 mg cm^{-2}) exhibited values above 13 mA cm^{-2}, as shown in Figure 5-13a. Higher Nafion contents yielded exchange current densities between 2-5 mA cm^{-2}.

From the apparent exchange current density values it is not possible to determine if the reaction proceeds directly from the gas or liquid phase, as the values obtained were very similar to those found in chloralkali electrolyzers. It is possible that for the gas phase reaction a different amount of active surface area is available in the MEA, as Nafion changes its structure when in contact with water vapor or liquid water. Another remaining question is if only the platinum surface covered with Nafion or water is electrochemically active, which is still under extensive discussion especially in the fuel cell community [6, 61]. This issue will be further discussed in chapter 6.1.

5.3.6.6 Mass transfer and reaction resistance analysis

Because of the complex structure of the MEA, it is important to determine which layer contributes with the highest mass transport resistance. The species analyzed are hydrogen chloride and chlorine. This is done through a mass Biot number analysis as presented by Vidaković [40] (Appendix 10.12) employing the binary diffusion coefficient (see Appendix 10.5.2), the effective diffusion coefficient D_i^{eff} (in case of porous media, see Appendix 10.4) or the mass transfer coefficient k and the layers thickness δ. It was considered that the void fraction is filled with gas. In order to assess the effect of the external mass transfer resistance from the gas bulk to the one found in the GDL, the following mass Biot number was employed:

$$\text{Bi}_\text{m}^{HDL/GDL} = \frac{D_{HCl}^{GDL}/\delta_{GDL}}{k_m}$$
(5-12)

where k_m takes a value of $1.76\cdot10^{-3}$ m s^{-1} (see Appendix 10.12), resulting in a mass transfer resistance 16 times greater in the GDL (250 μm thick, $7.01\cdot10^{-6}$ m^2 s^{-1} D_i^{GDL}) as in the HDL. To assess the ratio between mass transport resistances in the GDL and the CL eq. (5-13) was used:

$$\text{Bi}_\text{m}^{GDL/CL} = \frac{D_{HCl}^{CL}/\delta_{CL}}{D_{HCl}^{GDL}/\delta_{GDL}}$$
(5-13)

The mass transfer resistance turned to be 2 times higher in the GDL than in the CL. Even though porosity in the GDL is considerably higher than in the CL (75% against 20%, respectively [45, 62]), the GDL diffusion coefficient is only 7 times greater than in the CL ($7.01\cdot10^{-6}$ vs. $9.66\cdot10^{-7}$ m^2 s^{-1}). Considering that the GDL is 12 times thicker than the CL (250 vs. 20 μm), the greatest mass transfer resistance was found to be allocated in the GDL. In order to analyze the ratio of the mass transport to the kinetic resistance in the CL, the second Damköhler number [40] was used:

$$\text{DaII} = \frac{j\,\delta_{CL}}{z\,F\,c_{HCl}\,D_{HCl}^{CL}}$$
(5-14)

Considering a HCl concentration of 36.6 mol m^{-3} (at 101.3 kPa, 60°C) with a current density of 750 mA cm^{-2}, the DaII takes a value of 0.022, indicating a higher resistance of the electrochemical

reaction than CL diffusion. The multiplication of DaII with the different Biot numbers yields the relation of the mass transfer resistances to the resistance due to the electrochemical reaction. Multiplication of eqs. (5-13) and (5-14) shows the electrochemical reaction resistance is ~26 times higher than the resistance due to diffusion in the GDL.

$$\text{DaII } \text{Bi}_m^{GDL/CL} = 0.045 \qquad (5\text{-}15)$$

Comparing the electrochemical reaction resistance with the mass transport resistance through the entire MEA (multiplication of eqs. (5-12) and (5-15)), shows that both resistances are in the same order of magnitude:

$$\text{DaII } \text{Bi}_m^{GDL/CL} \text{Bi}_m^{HDL/GDL} = 0.73 \qquad (5\text{-}16)$$

Therefore, optimization of the mass transport in the GDL as well as the improvement of the kinetic rate in the CL are of crucial importance for total current density and MEA performance.

5.4 Cathodic measurements

Analogous to the anodic measurements, the cathodic gas feed was not humidified. This was done because the MEA is contacted with the supporting electrolyte in the counter electrode compartment, thus providing enough water in order to keep the CL well hydrated.

5.4.1 Effect of Nafion loading

MEAs were prepared under the same conditions as for the HClOR (varying Nafion loadings at constant platinum loading of 0.5 mg cm^{-2}).
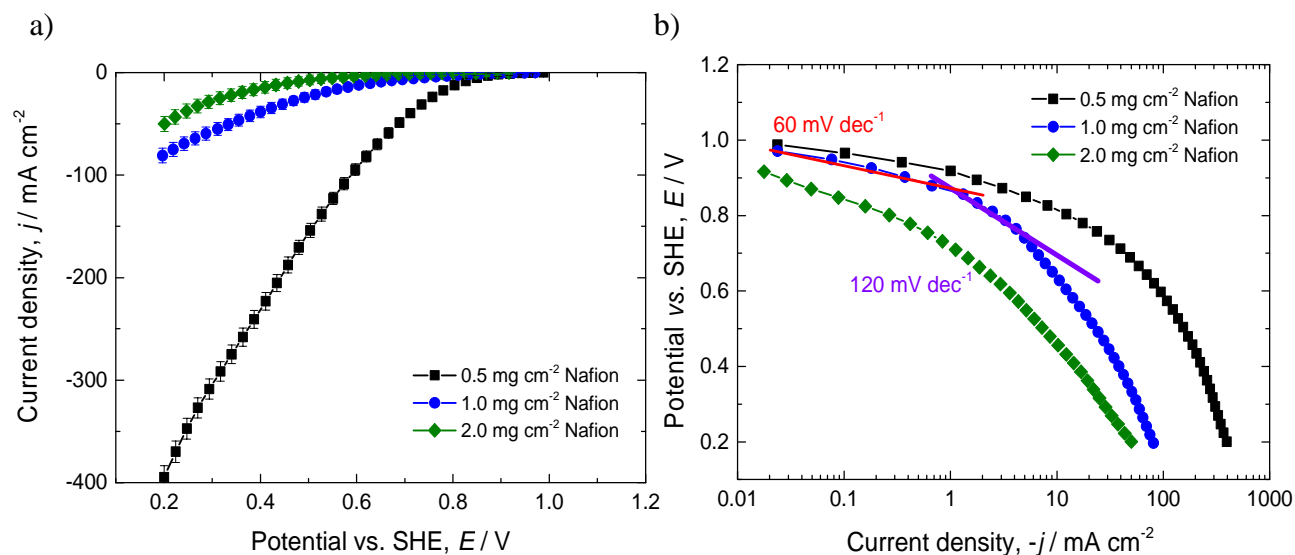
Figure 5-14 a) Polarization curve for the ORR on MEAs with platinum loading of 0.5 mg cm^{-2} and varying Nafion loadings; b) Tafel plot. Conditions: 60°C, 101.35 kPa, 100% oxygen, oxygen flow rate: 500 ml min^{-1}.

Contrary to the HClOR, MEA activity decreases with increasing Nafion loading as shown in Figure 5-14a. The best performance was obtained with a Nafion loading of 0.5 mg cm^{-2}, 38% Nafion content, in the entire potential range.

This could be attributed to a decrease in the active surface area, a change of the catalytic platinum surface, or a decrease of the effective oxygen concentration at the active sites with increasing Nafion loading. Active surface area can diminish because of electrical isolation due to excessive Nafion, which can lead to differences between 15-42% in current density at MEAs with and without Nafion [35, 63]. If this was the case, a reduction of current density with increasing Nafion loading should also be reflected in experiments for the HClOR (chapter 5.3.3). However, the opposite trend was observed. A change of the catalytic platinum surface could be hinted between MEAs with Nafion loadings of 0.5 and 1.0 when compared to the MEA with 2.0 mg cm^{-2}. The Tafel slopes for the former two show values of 60 mV dec^{-1} and 120 mV dec^{-1} while the latter one exhibits a value around 85 mV dec^{-1}, as shown in Figure 5-14b. The 60 mV dec^{-1} Tafel slope is associated to oxygen reduction on a platinum oxide surface under Temkin conditions, while the 120 mV dec^{-1} is associated to ORR on a chemisorbed oxygen-free platinum surface [64]. Therefore, a change in the prevailing type of platinum surface could be related to the Nafion loading, which at higher values allowed for a transition to a chemisorbed oxygen-free platinum surface at lower potentials.

A possible explanation for the trend in current density observed in Figure 5-14a is a reduction of the oxygen concentration at the active sites with increasing Nafion loading. Oxygen absorption in Nafion can be described by Henry's Law [65, 66], resulting in very small concentration values compared to the bulk (see Appendix 10.11). Hydrogen chloride follows a very different behavior, as observed in Figure 5-14, explaining the different trend in current density with Nafion loading. Rotating disk electrode (RDE) experiments were performed in order to assess the validity of current density being mainly determined by the reactant concentration at the active sites. By having a liquid electrolyte instead of a gas mixture, the trend in current density with Nafion loading should reflect that observed in Figure 5-14 just at lower current densities, as reactant concentration at the active sites will diminish proportionally to Henry's Law. CLs were prepared with the same compositions as those investigated in Figure 5-14 plus one with considerably less Nafion. Results are presented in Figure 5-15.

RDE experiments show that current density was negatively impacted by increasing the Nafion loading. A further Nafion loading decrease (red markers) improves MEA performance, especially at high overpotentials. This hints towards an optimal Nafion loading lower than 0.5 mg cm^{-2}, which corresponds to results presented by several authors [37, 48, 67], in which optimal Nafion loading values for the ORR were reported to be around 30-36% (depending on MEA preparation conditions and platinum and supporting material loadings). The lowest Nafion loading employed for MEAs in this work was 0.5 mg cm^{-2}, which corresponds to 38% Nafion, a value already above the optimal range. This indicates that the cathode performance can still be improved by further decreasing the amount of Nafion in the MEA, as shown by RDE experiments. As mentioned before, the low diffusion coefficient of oxygen in Nafion as well as the high amount of Nafion surrounding platinum particles at high Nafion loadings, could be a reason for the decrease in current density.
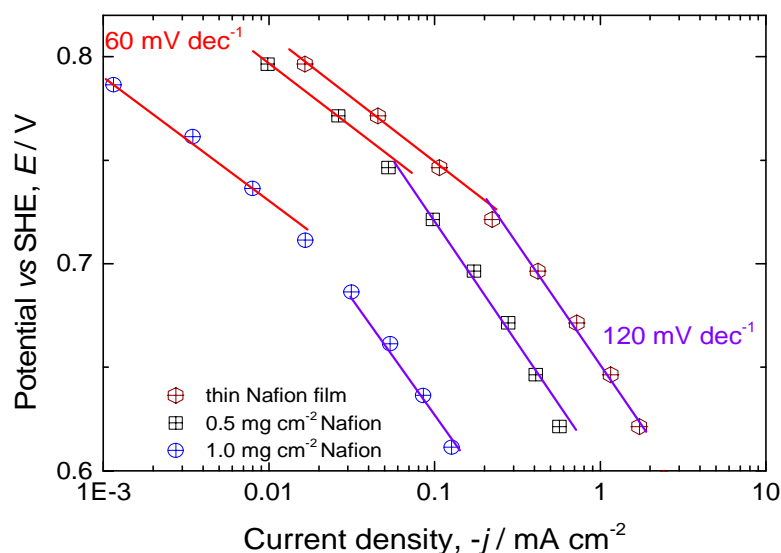
Figure 5-15 Tafel plot for RDEs at different catalyst to Nafion ratios with a constant Pt loading of 0.5 mg cm^{-2}. Conditions: 25°C, rotation rate: 3600 min^{-1}, electrolyte: 1M oxygen saturated sulfuric acid.

Exchange current densities for the ORR as a function of Nafion content were obtained from Figure 5-14b by the procedure presented for the HClOR at the electrode reversible potential, eq. (2-17). Values of $1.2 \cdot 10^{-6}$, $7.6 \cdot 10^{-6}$, and $8.5 \cdot 10^{-6}$ A m^{-2} for Nafion loadings of 0.5, 1.0, and 2.0 mg cm^{-2} were obtained. Reported values for the ORR in fuel cells with hydrogen oxidation as the anodic reaction are $1.7 \cdot 10^{-6}$ A m^{-2} for platinum oxide [45], which are in the same order of magnitude as those from our MEAs.

5.4.2 Effect of Temperature

The effect of temperature was investigated for MEAs with 0.5 and 1.0 mg cm^{-2} Nafion at a constant platinum loading of 0.5 mg cm^{-2} (Figure 5-16a). It is observed that limiting current density rises with increasing temperature. This could be attributed to an increase of the oxygen diffusion coefficient in Nafion, as corroborated by Parthasarathy *et al.* [51]. Current density also increased with temperature, as expected from faster kinetics as reported by other authors [45, 52, 68].

The same Tafel slope regimes as in the case of MEA Nafion variation were observed: at the low Nafion loading (thinner Nafion film surrounding the agglomerates) a low Tafel slope region from OCP to around 0.9 V, and a high slope region at lower potentials. At the higher Nafion loading the low Tafel slope region is shorter and transitions faster to the high Tafel slope region. At low Nafion loadings the high Tafel slope region attains values above 120 mV dec^{-1} already at current densities above 10 mA cm^{-2}. Some authors [69] reported that the potential window for the low Tafel slope region can extend further, up to values of 0.7 V. In our case, the transition to a slope of 120 mV dec^{-1} happens at considerably higher potential values, which can be attributed to the thickness and tortuous internal structure of the CL, as hinted by Chirkov and Rostokin [69]. They showed that extended low Tafel regions (up to 0.8 V) could be attained when the active layer is thin and current arises from pure kinetics (no influence of mass transport), which is commonly not the case of technical GDEs.

Exchange current density was calculated at 25 and 60°C for the high Nafion loading (in the same fashion as for the HClOR, just substituting the OCP with the reversible cathodic potential) yielding values of $2.6 \cdot 10^{-6}$ and $7.6 \cdot 10^{-6}$ A m^{-2}, while for the low Nafion loading values of $6.8 \cdot 10^{-6}$ A m^{-2} and $6.1 \cdot 10^{-5}$ were obtained. A change of one order of magnitude has been reported in literature when going from 25 to 60°C [45, 70], in accordance to data of the MEA with 0.5 mg cm^{-2} Nafion.
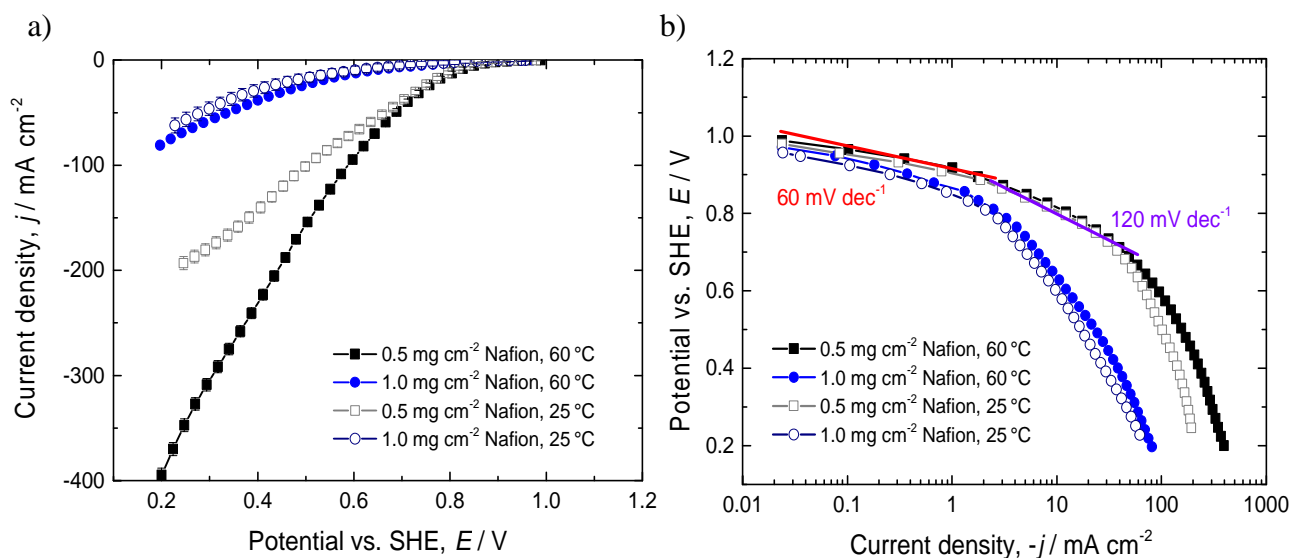

Figure 5-16 a) Polarization curves at 60 and 25°C for the ORR on MEAs with 0.5 and 1.0 mg cm^{-2} Nafion at constant 0.5 mg cm^{-2} platinum loading; b) Tafel plot. Conditions as in Figure 5-14.

It has been hypothesized in literature that higher temperatures shift the Pt/PtO mixed potential towards the electrode reversible potential and accelerate ORR kinetics, increasing exchange current density [45, 70]. This effect was observed for both analyzed MEAs. The contrast between values obtained for the low and high Nafion loadings could be correlated to a change in the composition of the Pt/PtO surface due to an increased Nafion content, as hinted by the different Tafel slopes obtained when varying Nafion loading.

5.4.3 Effect of Concentration

The effect of concentration for the ORR has been investigated by several authors [51, 71], especially because air is cheaper than a pure oxygen feed. This effect was measured at 60°C for oxygen concentrations of 100, 80, 60, 40 and 2% and presented in Figure 5-17a. A reduction of oxygen concentration from 100% to 20% yields an average current density decrease of 70% in the entire potential range, which is in accordance to results reported by other authors [51, 71].

The two characteristic Tafel slopes of 60 and 120 mV dec^{-1} were observed clearly only for 100% oxygen. At lower concentrations this slope was barely seen (at current densities below 0.1 mA cm^{-2} and potentials above 0.9 V, see Figure 5-17b) and at 2% oxygen was not present at all. In literature, the 60 mV dec^{-1} slope has been reported up to potentials as low as 0.8 V [45]. In Figure 5-17b, a slope between 60 and 120 mV dec^{-1} is observed at potentials higher than 0.85 V. The higher Tafel slope has been related to the platinum surface being free of oxygenated species, being the *r.d.s.* the first electron transfer.
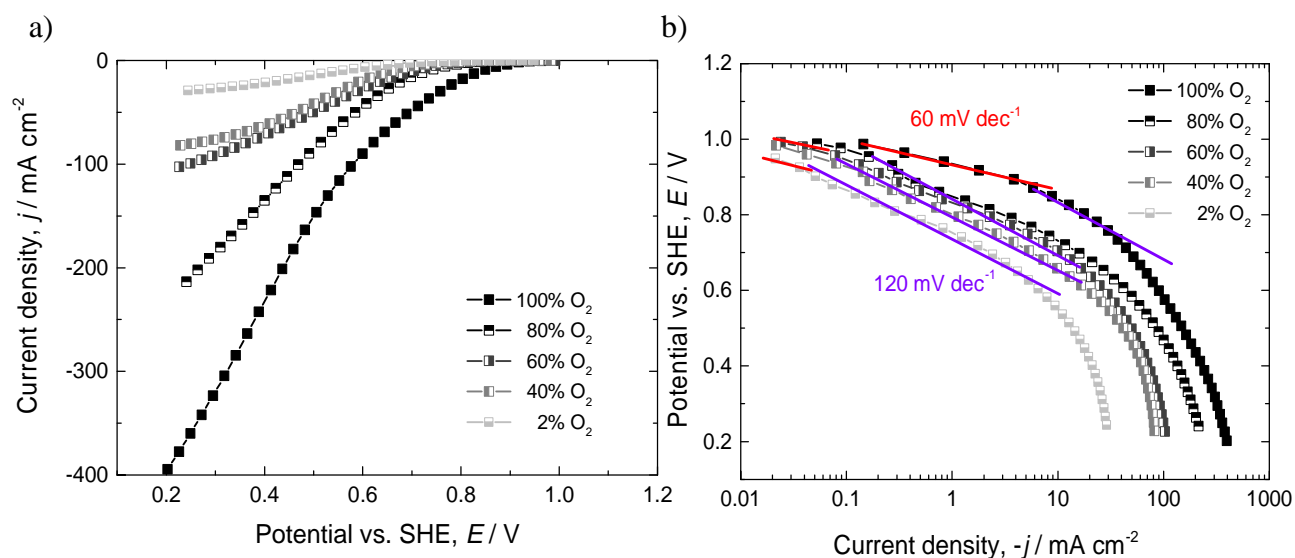
Figure 5-17 a) Polarization curves at different oxygen concentrations for the ORR on a MEAs with 1.0 mg cm^{-2} Nafion and 0..5 mg cm^{-2} platinum; b) Tafel plot. Conditions as in Figure 5-14.

It can also be seen from the Tafel plot that lowering the concentration from 100 to 80% has the greatest impact on current density when compared to the other concentration variations, analogous to the HClOR. The lower current density values show that the cathode is the limiting electrode for the HClOR-ORR reaction couple. Therefore it is advisable to use pure oxygen as the cathode feed in order to minimize the considerably high cathodic overpotential. With 21% oxygen and a potential of 0.2 V, a current density of only 50 mA cm^{-2} was obtained (interpolated from the curves of 4 and 40% oxygen in Figure 5-17a), in comparison with 400 mA cm^{-2} obtained with pure oxygen. Considering that the anode causes considerably lower potential losses than the cathode, optimization efforts should be focused more on the latter one, where a higher potential loss reduction might be possible.

Regarding the mass transport resistances in the MEA, a Biot number analysis analogous to the one presented for the HClOR, eq. (5-13) and (5-12), was employed. It was determined that in the cathode, the GDL mass transfer resistance is 6.3 times higher than in the CL.

The GDL use for the ORR is the same as for the HClOR, but the CL is thinner as less Nafion is present (10 µm). The diffusion coefficient of oxygen is almost twice as that of hydrogen chloride and oxygen has also a lower viscosity (see Appendix 10.6). The mass transfer resistance through the HDL and GDL is almost identical ($Bi_m^{HDL/GDL}$ = 1.04), therefore a lower oxygen concentration has a higher impact to current density along the entire analyzed potential range than an equivalent reduction of hydrogen chloride. Hydrogen chloride had a resistance 3 times higher in the GDL than in the HDL while employing the same GDL as in MEAs for the ORR.

5.4.4 Effect of Chloride ions

For the present process it was important to check the tolerance of platinum catalyst toward HCl crossover, as the influence of chloride ions to the ORR has been shown to be prejudicial along the entire potential range for the ORR [20, 72]. According to theory, no crossover is expected since Nafion should exclude the passage of chloride anions due to the sulfonic groups in its structure and the Donnan effect [73, 74]. Consequently, chloride anions can be transported through the membrane only as neutral HCl molecule. Still, HCl transport through the membrane cannot be excluded due to the significant concentration gradient between the anode and cathode compartments. Another point is the fact that water is transported from the anode to the cathode by the electroosmotic drag, and HCl has a great affinity to water and might be transported as a non-dissociated molecule.

This effect was estimated by measuring the performance of ORR after replacing the liquid electrolyte in the counter electrode compartment of the cyclone cell with hydrochloric acid. In accordance with literature [20, 72], our results confirmed that no observable HCl crossover takes place, as variations in current density ranged from 4-6%, which were in the same order of magnitude as experimental error (*ca* 5%).

6   Modelling

Modeling has received a lot of attention in literature as it offers the possibility to reduce the quantity of expensive, time-consuming, and complicated experiments, allowing for a better understanding of the phenomena taking place in the system. Electrochemical reactors can be described at different length scales and complexity (hierarchy), analogous to what other authors such as Vlachos *et al.* [75] have employed in the field of chemical reaction engineering. The latter authors introduced a hierarchy of models at each length scale describing the level of model detail. A schematic representation of the different length scales and hierarchy is presented in Figure 6-1.
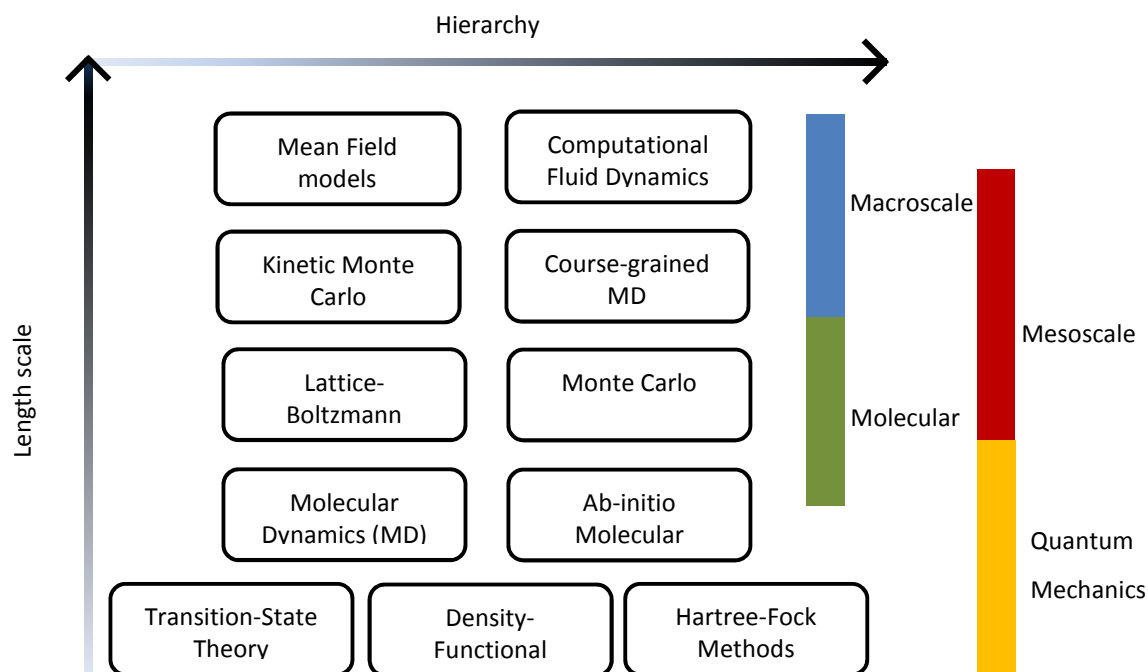

Figure 6-1 Modeling approaches overview organized by length scales and hierarchy.

As an example, at the Quantum Mechanics scale, Density Functional Theory can be employed in order to take into account activation energies, interactions between single atoms, etc. In order to get a broader insight at the same length scale, *i.e.* between several atoms, semi-empirical formulations with smaller calculation times such as Transition-State Theory can be employed, representing a lower hierarchy [75]. This hierarchy relation is kept along the entire length scale from atoms (Quantum Mechanics) up to entire reactors (Macroscale). In the macroscale, lower hierarchy formulations take the form of mean-field models, where the system is analyzed disregarding fluid dynamics, opposite to Computational Fluid Dynamics models.

In order to analyze the entire HClOR-ORR process, considering the model categorization of Figure 6-1, a mean field macroscale, 1-dimensional, isothermal model has been developed. The choice of a macroscale model is supported by the fact that it allows the direct computation of polarization curves, which can be compared with performed experiments done at isothermal conditions. For this purpose three main modeling domains have been introduced: two GDEs

(anode and cathode) and the membrane. Each GDE is in turn divided into the following components (see Figure 6-2):

- Hydrodynamic diffusion layers (HDL): Gas layers formed at the GDL-gas bulk interfaces.
- Gas diffusion layers (GDL): Conductive carbon clothes to provide physical support to the CLs, distribute current, and manage water.
- Catalyst layers (CL): Layers where the chemical and electrochemical reactions take place. They contain a further internal dimension: the agglomerate coordinate (Figure 6-2b). Agglomerates are considered to have two boundaries: the outer Nafion layer/CL and the internal core of platinum and C particles/outer Nafion layer.
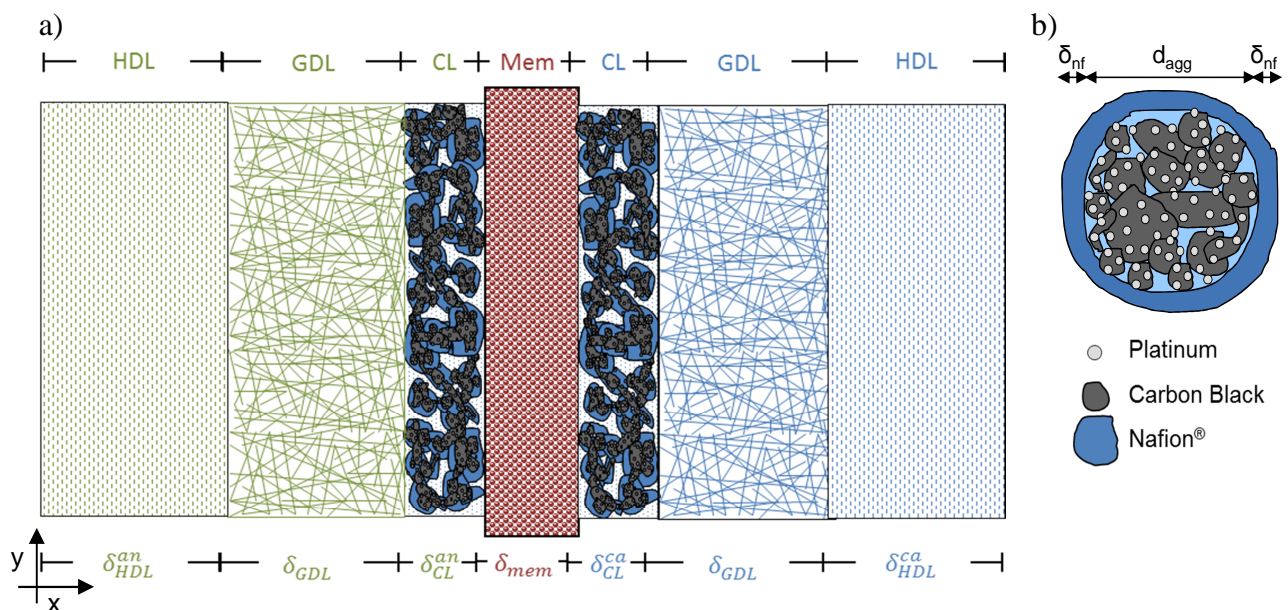

Figure 6-2 a) Modeling domains: Green – anode, red – membrane, blue –cathode; b) schematic representation of a single agglomerate.

Macroscopic models consider their domain as a continuum, employing effective transport properties *i.e.* diffusion coefficients, ionic and electric conductivities, etc. Other model parameters are obtained by fitting experimental data or making educated guesses based on SEM and TEM image analysis (layer thickness, void fraction, etc.). Ideally, model parameters should be obtained by using lower length scale model results (microscopic/mesoscopic models). This is still not common praxis, as the coupling of the multiple physical processes taking place in an electrolyzer requires immense computational resources for their proper simulation [76].

For this process, special attention was devoted to the GDEs. Because the HDL and GDL in the MEAs represent only a mass transport resistance, modeling efforts were concentrated in the CLs. In this layer not only electrochemical and chemical reactions take place, but also species, electron, and ionic transport. Because of this complexity, several models have been proposed in literature to describe the CL, such as the thin-film, flooded-layer, and agglomerate models [77, 78]. An overview of the macroscale models is presented in Figure 6-3.
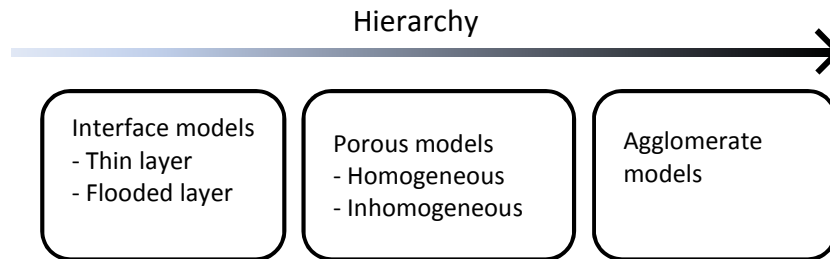
Figure 6-3 Overview of the different macroscopic modeling approaches for catalyst layers.

Interface models consider the CL as a boundary between the GDL and the membrane, ignoring its structure, thickness and composition (Figure 6-4a). These models commonly simulate only global reaction rates, but may also include more complex descriptions of reaction kinetics [79-84]. Most models describing entire electrochemical reactors employ this formulation.
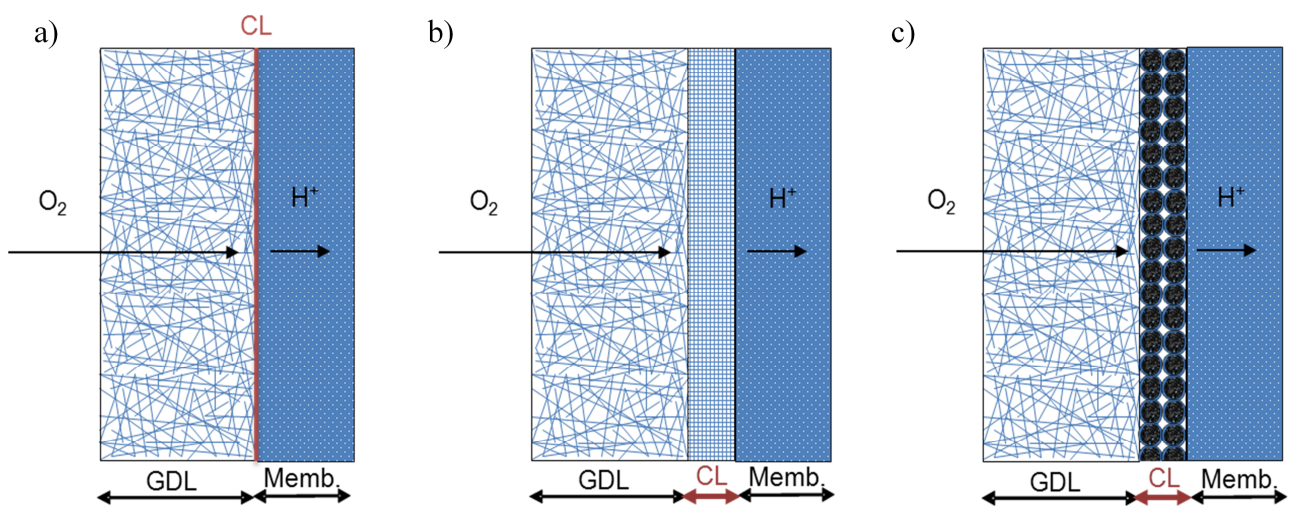

Figure 6-4 CL models: a) thin layer; b) homogeneous porous electrode; c) agglomerate model.

Porous electrode models consider the structure and thickness of the CL. They account for transport and consumption/production of species in the CL (Figure 6-4b). All three components, void space, electric, and ionic conducting networks are homogeneously distributed along the CL thickness. The effective transport properties are defined by the porosity and volume fraction of each phase. Porous models are mostly used to analyze kinetic formulations and reactant depletion along the CL [81-84]. Agglomerate models assume that the CL is composed of microsized Pt/C agglomerates bounded together by the polymer electrolyte, giving rise to a macro-sized porous network (Figure 6-4c). In addition, the reaction rates and transport inside the agglomerates are taken into consideration. These models are employed to better adjust experimental data, especially in the case of mass transport limitations (*e.g.* fuel cell flooding). Although both porous and agglomerate models account for layer thickness and morphology, they differ in the type of pores they consider (see Figure 6-5). Unlike porous electrode models where only secondary pores are considered [85-90], agglomerate models consider primary pores (20-40 nm diameter) and secondary pores also (0.05-1.0 µm) [66, 77, 91-95].
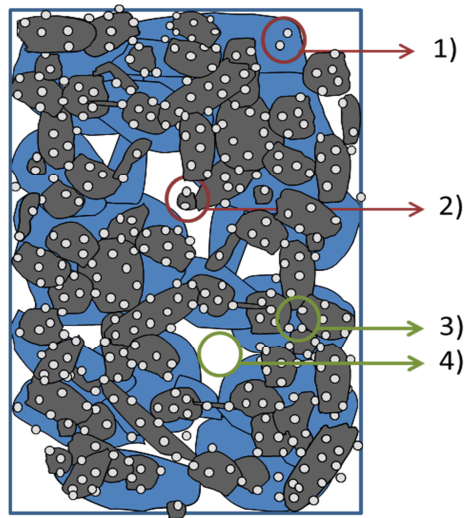
Figure 6-5 Schematic representation of the CL. 1: inactive catalyst due to lacking electrical contact, 2: inactive catalyst due to lacking electrolyte; 3: primary pore, 4: secondary pore; b) Schematic representation of a single agglomerate.

Therefore, porous models cover a "longer" length scale than interface models, but one shorter than agglomerate models. Harvey, *et al.* [96] made a comparison between the three modeling approaches for the ORR considering only one-phase flow. Employing the same CL parameters for all simulations, overpotential underestimation by the thin layer and porous models at 500 mA cm^{-2} was 25 and 60 mV, while at 1000 mA cm^{-2} was 80 and 140 mV, respectively. The thin layer model underestimates overpotential along the entire polarization curve. Porous and agglomerate models yield almost identical results at low overpotentials. At high overpotentials, only the agglomerate model is capable to correctly simulate limiting current density, while other approaches greatly overestimate it, as seen in Figure 6-6.
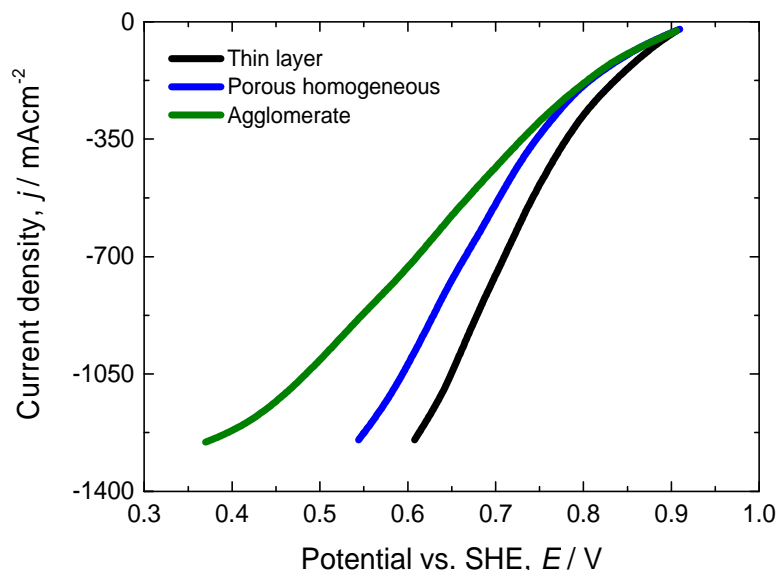

Figure 6-6 Polarization curves for interface, porous and agglomerate models, adapted from [96]

The main difference between models is the physical description they have of the CL, which affects the way current density behaves at high overpotentials. *I.e.*, thin-layer models don't reach a limiting current density because they don't consider any internal mass transport limitations, only

reactant depletion in the gas channel. On the other hand, flooded layer and agglomerate models incorporate mass transport limitations by means of a liquid or electrolyte layer, where reactant diffusion coefficients are considerably lower than in the gas phase, allowing for a better description of the limiting current densities. In general, agglomerate models have more parameters than other models, allowing for a more accurate description of experimental data [77, 78, 96].

There has been a lot of discussion about the physical basis of this model, especially because agglomerates are hard to identify in the finished MEAs. Nevertheless, because of the advantages of accurate current density description at high overpotentials and the insightful internal structural portrayal of the CL, the agglomerate model was chosen to describe the HClOR and ORR in this work. One dimensional (perpendicular to the MEA), isothermal agglomerate models for the anode and cathode were separately developed in order to analyze experimental data from the half-cell measurements. Because of the consideration of the agglomerate coordinate inside the CL, the anode and cathode models are considered quasi-two dimensional. Afterwards, a model for the membrane was developed and coupled to the anode and cathode models in order to simulate the entire reactor with the HClOR and ORR.

6.1 Assumptions

For both the anode and cathode models the following assumptions were made:

1. The gaseous components are incompressible and can be described by the Peng-Robinson-Stryjek-Vera equation (Appendix 10.3.1)
2. The system is isothermal
3. The system is in steady-state
4. All materials are isotropic
5. The electroneutrality condition applies
6. Reactants are transported only by diffusion
7. Agglomerates are round
8. Agglomerates are composed of a homogeneous mixture of Pt/C and Nafion
9. The applied potential is constant inside individual agglomerates
10. The catalyst layer is homogeneous and has a defined structure along its thickness
11. Water uptaken by Nafion behaves as free water
12. Nafion HCl uptake is the same as its pure water uptake

It is important to mention that the corrections to transport coefficients due to the tortuosity of the Nafion-Pt/C networks in this work are described by the Bruggeman correlation, directly related to assumptions 4, and 7-9. Strictly speaking, a 3D model is required to properly describe individual agglomerates, the electrical network (contact between agglomerate cores) as well as the ionic pathway (contact between Nafion in the agglomerate and the layer surrounding the agglomerate)

throughout the CL. Such an effort was made by Das *et al* [97], but could only study very limited areas (10x2x2 µm), as it proved to be computationally very expensive.

For the membrane, the following assumptions were made:
1. The membrane is impermeable to gas flow
2. The membrane is impermeable to dissolved oxygen and chlorine
3. HCl can be transported through the membrane only as a neutral molecule
4. The membrane porosity and thickness is independent of water uptake
5. The HCl/H_2O mixture inside Nafion complies with the Flory-Huggins theory for polymer/fluid interactions
6. The diffusion coefficient temperature dependency follows the Einstein-Stokes equation.
7. Water uptaken by Nafion has the same density and absorption properties as free water
8. The permeability of water through the membrane is negligible

Assumption 1 is only partially true as most gases show some degree of absorption in water, and therefore can be transported to the other electrode as dissolved species in water. Assumption four is not physically correct, as it is well known that the structure of Nafion is a function of water content [98] and changes from a sponge-like structure at low water contents to a hair-like structure at higher ones. Nevertheless, it is common practice in literature to consider the porosity and density of Nafion as constants [66, 78, 95, 99]. Assumption 8 refers to convective transport, which is considered to be negligible given the small pores present in Nafion.

6.2   Modeling domains

6.3   Physical phenomena

Based on this geometrical framework, the physical phenomena considered by the anode and cathode models are:
1. Reactant diffusion from the gas bulk to the MEA surface
2. Reactant diffusion through the void fraction of the GDL
3. Reactant diffusion through the void fraction of the CL
4. Reactant absorption from the gas pores (void fraction) in the CL into Nafion
5. Reactant diffusion through Nafion surrounding the agglomerates to the platinum active sites
6. Reaction at the platinum surface
7. Product diffusion from the platinum particle active sites to the outer surface of the Nafion layer surrounding the agglomerates
8. Product desorption from Nafion to the gas pores in the CL
9. Product diffusion through the GDL to the gas bulk

Assumption 5 implies that HCl reacts at the platinum surface in an absorbed state. This was assumed considering that Nafion has a very low permeability to gases and it has a high affinity to

water. HCl doesn't absorb in water as a neutral molecule like oxygen, but dissociates into protons and chloride. This is the reason to use an absorption model for HCl in Nafion and consider chloride activities and not hydrogen chloride concentration for the kinetic equations.

The physical phenomena described by the membrane model are:

1. Proton diffusion and migration from the anode to the cathode
2. Water transport by diffusion from the cathode to the anode and osmotic drag from the anode to the cathode
3. HCl transport by diffusion from the anode to the cathode

6.4   Anode

The HDL is relatively stagnant with tangential velocity variations of less than 2% [29]. The thickness of this layer is a function of the gas mixture's viscosity v_{mix}, the diffusion coefficient of the mixture D_{mix} (see Appendix 10.5.2), and the radial velocity ω.

$$\delta_{HDL} = \frac{3.57\, D_{mix}^{\frac{1}{3}}\, v_{mix}^{\frac{1}{6}}}{\omega^{\frac{1}{2}}} \tag{6-1}$$

The radial velocity is a function of the flow rate $\dot{V}$, which for the cyclone reactor is given by:

$$\omega = 19.2 \cdot \dot{V} \tag{6-2}$$

The GDL is considered to be a homogeneous carbon cloth with 75% porosity and a thickness of 350 µm. The CL thickness δ_{CL} is estimated according to the following equation:

$$\delta_{CL} = \frac{\left(\frac{l_{Pt}}{\rho_{Pt}} + \frac{l_C}{\rho_C} + \frac{l_{Naf}}{\rho_{Naf}}\right)}{(1 - \epsilon_{CL})} \tag{6-3}$$

6.4.1   Governing equations

6.4.1.1   Mass transport

Mass transport along the GDE proceeds *via* convection and diffusion. These mechanisms govern the transport of gaseous species in accordance to the general mass balance:

$$\frac{\partial}{\partial t}(\epsilon_m c_i) = -\nabla N_i^{diff} - \nabla(u_i\, c_i) + \chi \tag{6-4}$$

where χ stands for the species sources/sinks. For the HDL only the first term on the right-hand side was considered and porosity was taken as unity. Considering the low Reynolds number values obtained (<1000, laminar regime), the main transport phenomena taking place in the HDL is diffusion [29]. This was corroborated by the small changes in concentration along this layer obtained by the model (see chapter 6.4.4), allowing to neglect the effect of convection (effect on the profiles lower than 5%). To model diffusive transport, Fick's second law was used due to the low chlorine mass fractions, temperature, and pressure of the gases involved. It is important to note that for the gas phase concentrations were employed, as only small deviations from the ideal gas law were obtained for all investigated gases (deviations lower than 3%, see Appendix 10.3.1).

$$\frac{\partial}{\partial t} c_i^{\mathrm{HDL}} = -\nabla(\mathrm{D}_i^{\mathrm{HDL}} \nabla c_i^{\mathrm{HDL}}) \tag{6-5}$$

For the GDL (and other porous media), the diffusion coefficient was taken as the effective diffusion coefficient through the porous media (see Appendix 10.4.2). A discussion of the available correlations for the effective properties has been given by Shah *et al.* [100]. Convection, the second term on the right-hand side of eq. (6-4), was neglected as it accounted for less than 2% of the concentration gradient present in the GDL due to the small pore size, low permeability, and negligible CL thickness [101, 102]. This yields the total GDL mass balance:

$$\frac{\partial}{\partial t} \left(\epsilon_{GDL} c_i^{\mathrm{GDL}} \right) = -\nabla \left(\mathrm{D}_i^{\mathrm{GDL}} \nabla c_i^{\mathrm{GDL}} \right) \tag{6-6}$$

Besides species transport also sources/sinks are present, represented by the third term in eq. (6-4), with a_{CL} as the ratio of the surface area of the agglomerate to total CL volume and $\mathrm{N_{agg}}$ as the mass flux to/from the agglomerate. For gases in the CL the mass balance yields:

$$\frac{\partial}{\partial t} \left(\epsilon_{CL} c_i^{CL} \right) = -\nabla(D_i^{CL} \nabla c_i^{CL}) + a_{CL} N_{agg} \big|_{r=R} \tag{6-7}$$

where Nabla operates perpendicular to the CL. The mass flux from/to the agglomerate employs the activity of chloride ions and not HCl because, as mentioned in section 6.2, is calculated from the microscale mass balance inside the agglomerates, which yields the following analytical solution (details of the derivation are presented by Sun, *et al* [66]):

$$a_{CL} N_{agg} \big|_{r=R} = \left(a_{Cl^-}^{CL/agg} \right)^{2\beta} \left[\frac{1}{k_{\mathrm{mod}} v_i \mathrm{E_f} (1 - \epsilon_{CL})} + \frac{\delta_{\mathrm{Naf}}\left(r_{\mathrm{agg}} + \delta_{\mathrm{Naf}} \right)}{3 \mathrm{D}_{\mathrm{HCl}}^{\mathrm{Naf}} (1 - \epsilon_{\mathrm{CL}})} \right]^{-1} \tag{6-8}$$

Due to the highly non-linear nature of the HCl-H$_2$O system, activities instead of concentrations were employed for absorbed species. The first term on the right hand side represents the effect of chloride activity, the second one kinetics, and the third one the mass transport resistance through the Nafion layer surrounding the agglomerate. Chlorine activity is a direct function of the concentration of hydrogen chloride at the CL/agglomerate interface. Commonly, gas absorption in Nafion is described by Henry's Law [65, 66, 103], which is not applicable to the HCl- H$_2$O system due to its non-linearity (see Figure 10-5). Therefore, experimental data for HCl absorption (see Appendix 10.11.3) was employed to relate the gas fraction of hydrogen chloride in the CL gas pores, y_{HCl}, to the absorbed HCl mole fraction in Nafion, x_{HCl}. This relation is shown in eq. (6-9), where T_s stands for temperature in °C:

$$x_{HCl} = -\frac{\ln\left(\frac{-1.59E - 4T_s + 1.027}{y_{HCl}} - 1 \right) - 8.525 \cdot 10^{-4} \mathrm{T_s} + 0.1734}{0.4737 \mathrm{T_s} + 42.544} \tag{6-9}$$

Knowing the concentration of water in Nafion (from the water uptake of Nafion, see Appendix 10.7), the concentration of HCl in Nafion can be calculated using the result from eq. (6-9):

$$c_{\mathrm{HCl}}^{\mathrm{Naf|CL}} = \frac{\mathrm{x_{HCl}} c_{\mathrm{H_2O}}}{1 - \mathrm{x_{HCl}}} \tag{6-10}$$

For the reactant and product absorption in the liquid electrolyte, it was considered that Nafion had the same absorption properties as water, as no data is available on hydrogen chloride absorption in Nafion. A detailed procedure to calculate the absorbed concentrations of hydrogen

chloride and chlorine is given in Appendix 10.11. First, the weight fraction of HCl in equilibrium with the hydrogen chloride concentration in the CL void fraction is calculated. With this value, the concentration of HCl in Nafion is determined and employed in the activity model shown in Appendix 10.3.3.

6.4.1.2 Reaction mechanism

For the first term in brackets in eq. (6-7), the HCl oxidation kinetics, a Heyrovsky-Tafel mechanism with the Tafel reaction as the *r.d.s.* can be employed, as shown in previous work [104, 105] and in chapter 5.3.6. This has been also supported by other authors [10, 41].

$$Cl^- + Pt \rightleftharpoons PtCl + e^- \qquad (6\text{-}11)$$

$$2PtCl \rightleftharpoons 2Pt + Cl_2 \qquad (6\text{-}12)$$
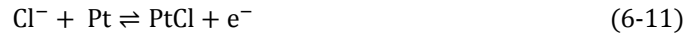
Both reactions were modeled according to the power law. As an example, the Heyrovsky reaction is presented:

$$r_{s,H} = k_{o,H}^+ a_{Cl-}^{CL/Naf}(1 - \theta_{Cl}) - k_{o,H}^- \theta_{Cl} \qquad (6\text{-}13)$$

The kinetic constants for the electrochemical reaction were defined as:

$$k_o^+ = \frac{k_o^{+,o}}{zF a_{Cl-,ref}^{CL/Naf}} exp\left(\frac{\beta F}{RT}\eta_{CL}\right) \qquad (6\text{-}14)$$

$$k_o^- = \frac{k_o^{-,o}}{zF \theta_{Cl-,ref}} exp\left(-\frac{(1-\beta)F}{RT}\eta_{CL}\right) \qquad (6\text{-}15)$$

where β stands for the symmetry factor, F for Faraday's constant, and η_{CL} for the electrode overpotential. The kinetic constant for the chemical reaction was defined in a similar manner without the exponential term. Furthermore, a single kinetic formulation was employed assuming the Tafel reaction is the *r.d.s.* and that the overall reaction takes place under Temkin conditions. As shown by Gileadi [55], total current density can be expressed as:

$$j = 2Fk_T\left(\frac{k_{o,H}^+}{k_{o,H}^-}\right)^{2\beta}\left(\frac{a_{Cl-}^{CL/Naf}}{a_{Cl-,ref}^{CL/Naf}}\right)^{2\beta}(a_{Cl-,ref}^{CL/Naf})^{2\beta} \exp\left[\frac{2\beta F}{RT}(E_{rev} + \eta_{CL})\right] \qquad (6\text{-}16)$$

The term $2Fk_T(k_{o,H}^+/a_{Cl-,ref}^{Cl/Naf} k_{o,H}^-)^{2\beta}(a_{Cl-,ref}^{CL/Naf})^{2\beta} \exp(\frac{2\beta F}{RT}E_{rev})$ has the units A m^{-2} and represents an intrinsic exchange current density j_o^{in}, which is independent of CL structural parameters and is characteristic for each catalyst. As shown in previous work [104], the equilibrium potential for the HClOR is hard to define, as the chlorine partial pressure plays a significant role and can hardly be controlled or measured at the CL in our setup. Therefore, exchange current density values estimated from experimental Tafel plots are apparent exchange current densities j_o^{ap}, a function of the open circuit potential ($E^{o.c.}$, taken as 1.04 V), electrode thickness, catalyst and Nafion loading, etc. [105]. The relationship between the intrinsic and apparent exchange current densities is given by:

$$j_o^{app}(E^{o.c.}) = a^o m_{Pt} j_o^{in} \qquad (6\text{-}17)$$

where m_{Pt} stands for the catalyst loading in the CL and a^o for the catalytic surface area per catalyst mass. Considering the same j_o^{in} for all CL structures (correct only as long as the same catalyst is employed), the effective specific active surface area in the CL a_{Pt}^o can be estimated knowing the apparent exchange current density from experiments.

The spherical geometry of the agglomerates and concentration change along its core is taken into account by means of a Thiele module and effectiveness factor approach [66]. The Thiele module is defined as:

$$\Phi_j = \frac{r_{agg}}{3} \sqrt{\frac{(n+1)\,k_{mod}\,c_{Cl-}^{CL|Agg^{n-1}}}{2D_i^{agg}}} \tag{6-18}$$

with the agglomerate radius r_{agg}, reaction order n, diffusion coefficient inside the agglomerate D_i^{agg}, and a modified kinetic constant k_{mod}, which includes the effect of both reactions through j_o^{in}.

$$k_{mod} = \frac{a_{Pt}^o\,j_o^{in}}{zFc_{Cl-}^{ref}} \exp\left(\frac{2\beta F}{RT}\eta_{CL}\right) \tag{6-19}$$

The effective specific surface area can be derived from geometrical considerations:

$$a_o^{Pt} = a_o \frac{l_{Pt}}{\delta_{CL}} \tag{6-20}$$

High Φ-values represent a much faster reaction rate than diffusion, or that reactants are consumed in the outer layers of the agglomerate leaving its core partially unused. *I.e.,* for a Φ-value of 2, only 80% of the agglomerate volume is employed; at a value of 5, only 50%. With the Thiele module the efficiency factor E_f is obtained.

$$E_f = \frac{1}{\Phi}\left(\frac{1}{\tanh(3\Phi)} - \frac{1}{3\Phi}\right) \tag{6-21}$$

Current density can be expressed as a mass flux by means of Faraday's law, which yields after some mathematical manipulation (as presented in [66]):

$$a_{Pt}^o N_{agg}\big|_{r=R} = \left(a_{Cl-}^{CL/agg}\right)^{2\beta} \left[\frac{1}{k_{mod}E_f(1-\epsilon_{CL})}\right]^{-1} \tag{6-22}$$

Considering the transport limitations imposed by the Nafion layer surrounding the agglomerate core, eq. (6-22) turns into eq. (6-8).

The electrochemical reaction's driving force is the overpotential η_{CL}, which in this work was considered to be homogeneously distributed inside the agglomerate and to be constant throughout the CL (due to its low thickness, less than 8 µm). It was calculated as the difference between the given potential and the experimentally observed open circuit potential of 1.04 V.

$$\eta_{CL} = E - 1.04 \tag{6-23}$$

6.4.2 Boundary conditions

6.4.2.1 Mass transport

The boundary conditions employed for species transport are:

Anode gas channel/HDL$_{an}$	$x = 0$		$c_i^{HDL} = c_i^b$	(6-24)

HDL$_{an}$/GDL$_{an}$	$x = \delta_{HDL}^{an}$	$-N_i^{HDL} = -N_i^{GDL}$		(6-25)
GDL$_{an}$/CL$_{an}$	$x = \delta_{HDL}^{an} + \delta_{GDL}$	$-N_i^{GDL} = -N_i^{CL}$		(6-26)
CL$_{an}$/Membrane	$x = \delta_{HDL}^{an} + \delta_{GDL} + \delta_{CL}^{an}$	$N_i = 0$		(6-27)
Agg Nafion layer/CL void	$r = r_{agg} + \delta_{naf}$	$c_i^{Naf} = \frac{x_{HCl}c_{H_2O}}{1-x_{HCl}}$ (See Appendix 10.11)		(6-28)

In Table 6-1 a summary of the employed parameters in the simulations is presented.

Table 6-1 Parameters employed for the simulation

Parameter	Symbol	Value	Units	Reference
GDL thickness[2]	δ_{GDL}	250	µm	[62, 106]
GDL density[2]	ρ_{GDL}	700	kg m^{-3}	[62]
GDL electrical conductivity[2]	σ_{el}^{GDL}	200	$S\,m^{-1}$	[106]
GDL pore size[2]	r_p^{GDL}	30	µm	[106]
GDL porosity[2]	ϵ_{GDL}	0.75	-	[62]
CL thickness	δ_{CL}	9-14	µm	calculated
CL electrical conductivity	σ_{el}^{CL}	5500	$S\,m^{-1}$	calculated
CL porosity	ϵ_{CL}	0.09-0.52	-	[107]
Pt density	ρ_{Pt}	21450	kg m^{-3}	[108]
Agglomerate radius	r_{ag}	100	nm	[105]
Vulcan XC72R density	ρ_C	1750	kg m^{-3}	[97, 109, 110]
Nafion density[1,3]	ρ_{Naf}	1588	kg m^{-3}	calculated
Max. Nafion 117 water content (liquid)	λ_{liq}^{max}	22	mol H$_2$O mol SO$_3^{-1}$	[18, 111, 112]
Max. Nafion 117 water content (vapor)	λ_{vap}^{max}	14	mol H$_2$O mol SO$_3^{-1}$	calculated
HCl bulk diffusion coefficient in the mixture	D_{HCl}^0	$1.10 \cdot 10^{-5}$	m^2 s^{-1}	calculated
HCl diffusion coefficient in the GDL	D_{HCl}^{GDL}	$8.62 \cdot 10^{-6}$	m^2 s^{-1}	calculated
HCl diffusion coefficient in the CL	D_{HCl}^{CL}	$2.10 \cdot 10^{-6}$	m^2 s^{-1}	calculated
HCl diffusion coefficient in Nafion	D_{HCl}^{Naf}	$9.68 \cdot 10^{-12}$	m^2 s^{-1}	[21] / calculated
HCl diffusion coefficient in the agglomerate	D_{HCl}^{agg}	$3.22 \cdot 10^{-12}$	m^2 s^{-1}	calculated
Exchange current density	j_o^{in}	$2.10 \cdot 10^{-1}$	A m^{-2}	calculated

1: Conditions for all parameters: 60 °C, 1 bar, 100% saturation;
2: Untreated carbon cloth from Quintech was considered as the GDL;
3: Nafion 117 was considered for Nafion properties

6.4.3 Temperature effect on HClOR kinetics

The model developed in chapter 6.4 and the experimental data presented in chapter 5.3.4 were employed to determine j_o^{in} and E_a for the HClOR. Kinetics for the HClOR were described by eq. (6-16), which after regrouping terms and using the definition of the intrinsic exchange current density results in eq. (6-29):

$$j = j_o^{in} \left(\frac{a_{Cl-}^{CL/Naf}}{a_{Cl-,ref}^{CL/Naf}} \right)^{2\beta} \exp\left(\frac{2\beta F}{RT} \eta_{CL} \right) \qquad (6\text{-}29)$$

As shown in chapter 6.4.1.2, j_o^{in} is a function of temperature, which was approximated by an Arrhenius formulation:

$$j_o^{in} = A \, \exp\left(\frac{-E_a}{RT}\right) \qquad\qquad (6\text{-}30)$$

where E_a stands for the activation energy. Simulations for the anodic model were done considering a gas flow of 100% hydrogen chloride on MEAs with 0.5 mg cm^{-2} platinum, 1.0 mg cm^{-2} Nafion loading, and a Pt/C ratio of 60%, as shown in Figure 6-7. Fitting experimental values to eq. (6-30), an activation energy of 48.05 kJ/mol and a preexponential factor of 5.037·10^6 A m^{-2} were obtained.
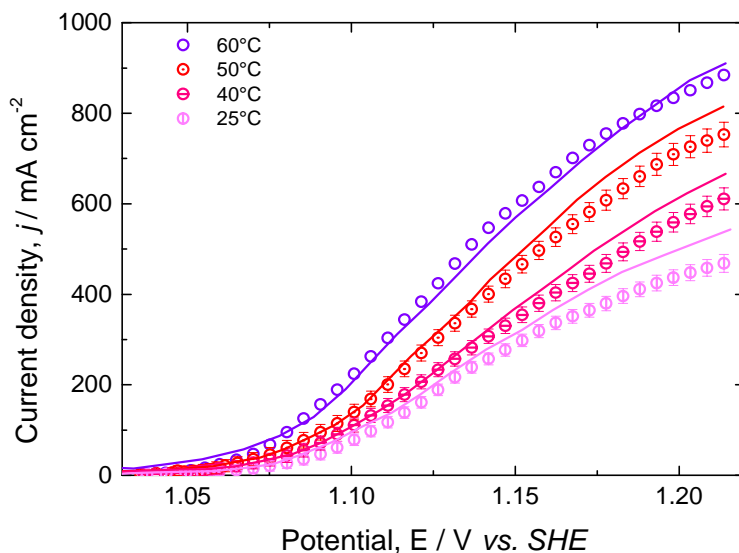

Figure 6-7 Polarization curves at different temperatures. Conditions: Pt loading: 0.5 mg cm^{-2}, Nafion loading: 1.0 mg cm^{-2}, hydrogen chloride concentration: 100%, pressure: 101.13 kPa.

The activation energy value is considerably higher than the apparent activation energies found experimentally [105], which ranged from 16 to 30 kJ mol^{-1}. It is important to note that a linear decrease of HCl concentration represents a non-linear decrease of HCl activity, as shown in Appendix 10.3.2. The activity coefficients for HCl in water attain values up to 9 at 60°C, while at 25°C they can be as high as 15. This complicates assigning the difference between fitted and experimental values to the variable water uptake of Nafion, which increases with temperature allowing a greater amount of hydrogen chloride to absorb.

Regarding the intrinsic exchange current density, values from the experimental apparent values at 1.04 V can be obtained with help of eq. (6-17). Results yield values four times higher than those obtained from the simulations, but have the same order of magnitude. *I.e.*, for the MEA employed in Figure 6-7, an intrinsic exchange current density from apparent experimental data of 0.65 A m^{-2} is obtained (a_o = 32 m^2 g^{-1}, [113] and j_o = 10.4 mA cm^{-2} for the MEA shown in Figure 6-7), while the value from simulations is 0.15 A m^{-2}.

As observed in Figure 6-7, at all investigated temperatures current density was overestimated at potentials lower than 1.08, while in the potential region from 1.08 to 1.15 showed good agreement. At potentials higher than 1.15 V experimental data showed a slower increase in current density as simulations. The reason for such behavior at low potentials is much likely the overestimation of the capacity of Nafion to absorb HCl, which corresponds to the fact that higher

amounts of HCl can be absorbed at lower temperatures (see Appendix 10.11.3). However, Nafion uptakes a smaller amount of water at lower temperatures, counteracting the increased HCl absorption. Also, as mentioned before, it was assumed the behavior and absorbing properties of water uptaken in Nafion were the same as those of pure water.

6.4.4   Diffusion layers

Concentration profiles of hydrogen chloride/hydrochloric acid were analyzed through the entire MEA structure at three different potentials: 1.07, 1.13, and 1.20 V at the same conditions as in section 6.4.3. The HDL has a thickness of 860 µm at the above mentioned conditions, greatly surpassing the thickness of the GDL (250 µm) and CL (10 µm).

Hydrogen chloride needs to diffuse through both the HDL and GDL in order to reach the active sites in the CL. These layers pose transport resistances to hydrogen chloride, which shows a linear decrease as shown in Figure 6-8a. The slope of the concentration decrease is higher in the GDL than in the HDL, corroborating the results presented in the Biot number analysis from chapter 5.3.6.6. The change of hydrogen chloride concentration in the CL shows a different behavior, as it is not only affected by diffusion but also consumption throughout the layer. Therefore, the HCl concentration profile in the HCl is not linear, as shown in Figure 6-8b.
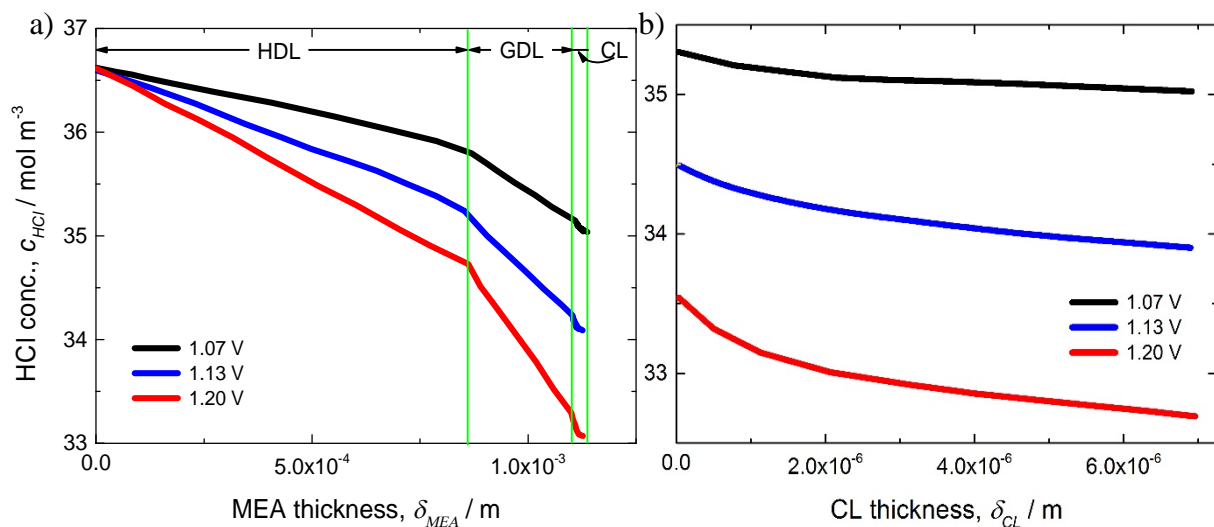

Figure 6-8 HCl concentration at different potentials. Conditions: Pt loading: 0.5 mg cm^{-2}, Nafion loading: 1.0 mg cm^{-2}, hydrogen chloride concentration: 100%, pressure: 101.13 kPa, temperature 60°C.

It can be seen that at higher potentials hydrogen chloride consumption is higher, and the greatest concentration drop takes place in the GDL. Due to the small thickness of the CL, hydrogen chloride has a relatively uniform distribution in the gas channels even at high potentials. Hydrogen chloride was not depleted in the CL void fraction for any of the potentials investigated. Therefore, it is expected that the main transport limitations take place inside the agglomerates, where the absorbed HCl diffusion coefficient is considerably lower than in the gas phase.

Because the hydrogen chloride depletion is low along the MEA, reaction kinetics needs to be improved in order to obtain better current densities. HCl absorption behavior shows little change between the concentrations observed along the CL (33-35 mol m^{-3}, see appendix 10.11.3), leading to the conclusion that a greater improvement in current density could be obtained with a better understanding of the CL structure. The agglomerate model allows modifying the internal structure of the CL and agglomerates, providing a better insight into where the main limitations could be.

6.4.5 CL Structural effects

Agglomerate models commonly employ 8 parameters, which are shown in Table 6-2. These parameters affect the polarization curves to a different extent and not all of them can be experimentally controlled or defined. Therefore, parameters were classified in three categories: controllable (can be directly controlled when preparing a MEA), measurable (can be representatively measured but not directly regulated), and non-measurable (can only be estimated or assumed). The effects of these parameters were analyzed in order to identify the most critical ones and identify the best optimization potential in the CL. Because of the interrelation between parameters, commonly changing one parameter affects others, thus complicating the discussion of one single parameter at a time.

For the results to be presented in the next sections MEAs are characterized by two parameters, the catalyst loading l_{Pt} and the Nafion content σ_{Naf} (calculated from the platinum and Nafion loading together with the platinum to carbon ratio). It has been shown by us [105] and other researchers [48, 114], that not only the Nafion content must be taken into consideration when properly characterizing MEAs, but also either the platinum or Nafion loadings. For example, a CL with 55% Nafion might be composed of a Pt/C catalyst with 60% platinum and the following loadings: 0.5 mg cm^{-2} platinum and 1.0 mg cm^{-2} Nafion, 1.0 mg cm^{-2} platinum and 2.0 mg cm^{-2} Nafion, as well as 2.0 mg cm^{-2} platinum and 4.0 mg cm^{-2} Nafion.

Table 6-2 Agglomerate model parameters

Controllable		Measurable		Non-measurable	
Pt to C ratio	$rw_{Pt/C}$	CL thickness	δ_{CL}	Agglomerate Nafion content ς_{Naf}	
Pt loading	l_{Pt}	CL porosity	ϵ_{CL}	Nafion layer thickness	δ_{agg}
Nafion loading	l_{Naf}	Agglomerate radius	r_{agg}	around the agglomerate	

For results presented in this work the Nafion content and either the platinum or the Nafion loading is given for every simulation presented. Conditions for the simulations were 100% HCl at 101.3 kPa at 60°C.

6.4.5.1 Nafion loading

GDEs with 0.5 mg cm^{-2} platinum and 0.5, 1.0 and 2.0 mg cm^{-2} Nafion, corresponding to 38, 55, and 71 wt% Nafion respectively, were studied at 60°C. It has been reported in literature that increasing

the Nafion loading has a negative impact in the void fraction, attaining values from 25 to 10% [107, 115]. As mentioned before, Nafion is required inside the agglomerate to fill the void space and provide an ionic conductive network, represented by the agglomerate Nafion content. A maximum value of 48% is defined in order to guarantee contact between electrically-conductive particles, analogous to the simple cubic packing structure from the Bravier crystal system [116]. Increasing the anodic Nafion loading increases also catalyst utilization, as shown in chapter 5.3.3, which translates into a change of the catalytic surface area per catalyst mass a_o. Employing the experimentally obtained apparent exchange current density j_o^{app} for a MEA with 71% Nafion, 0.5 mg cm^{-2} platinum (103.8 A m^{-2}), and a_o (32 m^2 g^{-1}) from the catalyst vendor [107], an intrinsic exchange current density j_o^{in} of 0.65 A m^{-2} is obtained from eq. (6-17). This value was employed for all simulations at a temperature of 60°C.

As a change in Nafion loading alters the surface area per catalyst mass a_o (due to partial surface covering of the catalyst surface, leaving it inactive), it was employed as a fitting parameter. Considering that j_o^{in} is independent of the CL structure, starting values for a_o were obtained from eq. (6-17) using j_o^{app} from experiments. The active surface area was calculated with eq. (6-20). Because the change of CL void fraction with different Nafion loadings is not known, it was also employed as a fitting parameter. Starting values for the CL void fraction of 10, 13, and 52% were employed for Nafion loadings of 2.0, 1.0, and 0.5 mg cm^{-2} [107] respectively. Optimization was done using a trust-region method based on the non-linear minimum squares algorithm implemented in Matlab. The values employed for the simulation are presented in Table 6-3 with fitting parameters highlighted.

Simulations are compared to experimental data in Figure 6-9a. It can be seen that the model is able to qualitatively reproduce the experimentally observed effect of Nafion loading variation.

Table 6-3 Agglomerate model parameters for simulations depending on Nafion loading

Parameter	Unit	Nafion Loading / mg cm^{-2}		
		2.0	1.0	0.5
j_o^{app}	mA cm^{-2}	10.4	4.2	2.8
a_{Pt}^o	m^{-1}	1.09E+07	8.25E+06	8.87E+06
δ_{Naf}	nm	54.09	35.09	20.63
σ_{Naf}	%	70.6	54.5	37.5
a_o	m^2 g^{-1}	32.0	12.3	8.3
ϵ_{CL}	%	11.3	18.5	24.1

Quantitatively, the model overestimates current density especially at potentials below 1.09 V. This could be attributed to an effect not considered in the model which experimentally affects the activation region, such as a difficult chlorine desorption or change of the catalytic surface with potential. Trials were made to lower the intrinsic exchange current density to better describe the low potential region of the polarization curves. This resulted in a better agreement at potentials below 1.09, but a higher underestimation of current density at potentials above 1.13 V, deteriorating the overall result.
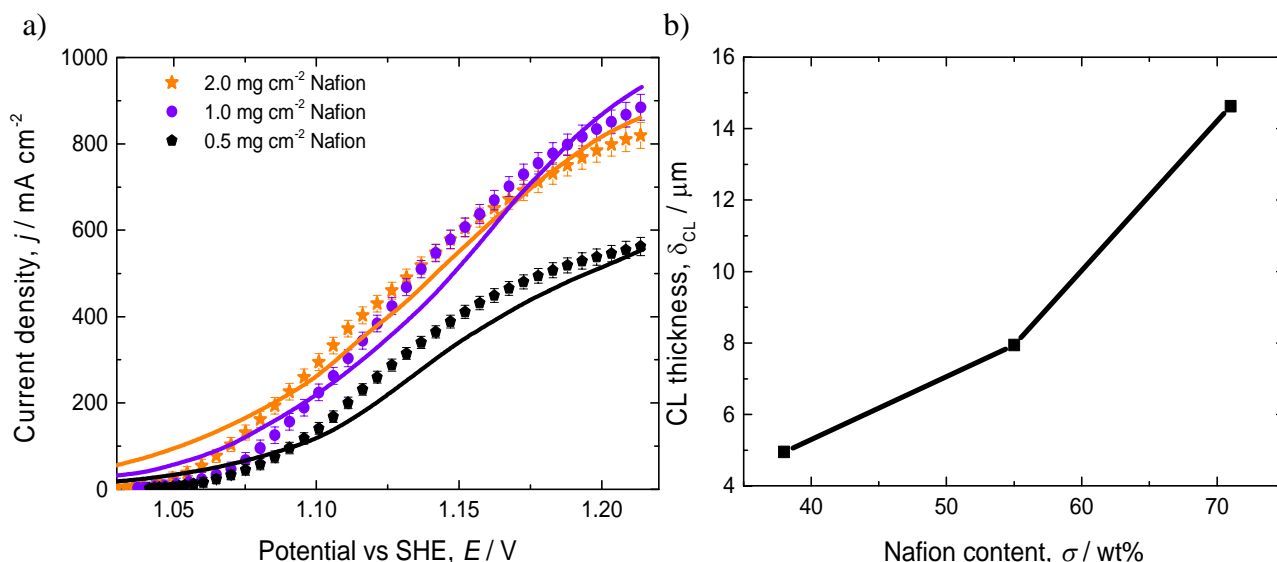
Figure 6-9 Experimental and simulation data for different Nafion loadings at constant 0.5 mg cm⁻² platinum loading; b) Dependence of calculated CL thickness on Nafion content in the CL. Conditions as in Figure 5-3.

Higher Nafion loadings lead to thicker CLs, which points to higher values of a_o and thus a higher effective specific active surface area a_{Pt}^o. The increase in a_{Pt}^o with the Nafion loading supports the observation made in chapter 5.3.3, that the optimum Nafion loading for the HClOR is considerably higher than for the ORR. As it was mentioned before, hydrogen chloride has a higher absorption in water than oxygen (at 60 °C is 8.70 wt% for HCl while for oxygen it reaches only 0.01%), allowing an increased HCl concentration to reach the active sites. This leads to the ORR depending more on diffusional transport than the HClOR. Another probable explanation for the discrepancy at low potentials is that at potential values above 1.11 V, the HClOR proceeds also on carbon with the same Tafel slope as for platinum [60]. Therefore, a higher Nafion loading would render more carbon active allowing for higher current densities, which is not taken into account by the model. This leads to an overestimation of the platinum surface area allowing a better agreement at higher potentials, while overestimating current density at lower potentials (< 1.09 V).

Another effect of increasing the Nafion loading is the rise in the thickness of the Nafion layer surrounding the agglomerates, δ_{Naf}, which poses a mass transport resistance resulting in a decrease of current density. The observed Nafion content optimum in the current study is surprisingly high: 52% Nafion. In contrast, the reported optimum for the ORR on similar catalysts as in this work lies around 32% [38]. This shows that the effect of thicker Nafion layers surrounding the agglomerates is less significant for the HClOR than for the ORR, mainly due to the higher absorption of hydrogen chloride in Nafion, as mentioned before. Therefore, optimization results reported for the ORR could not be directly employed for the HClOR.

The Nafion loading shows a high influence in current density, allowing for overpotential savings of up to 70 mV at current densities around 350-400 mA cm⁻², at which commonly electrolyzers are industrially operated.

6.4.5.2 Platinum loading

Polarization curves for platinum loadings of 0.2, 1.0 and 2.0 mg cm^{-2} at a constant Nafion loading of 0.5 mg cm^{-2} (60, 23, and 13 wt% Nafion respectively) were simulated and compared with experiments, as shown in Figure 6-10a. Similar as for the Nafion loading, a_o values were fitted and are presented in Table 6-4. The value of the intrinsic exchange current density was the same as for the Nafion loading variation.

Changing the platinum loading alters the maximum number of available active sites present in the CL. Due to the small radius of the agglomerates, even for the smallest Nafion content, 13%, agglomerates were completely filled with Nafion and had a thin Nafion film surrounding them. In contrast to the variation of Nafion loading, CL thickness didn't changed much with the variation of platinum, as it has a considerably higher density than Nafion (see Figure 6-10b). This is corroborated experimentally in Figure 6-10a, where only a minimal difference in current densities at platinum loadings above 1.0 mg cm^{-2} was obtained. Even though at high platinum loadings more catalyst is present in the CL, Nafion is not present in enough quantities to cover all platinum particles. Therefore the amount of active sites reaches a plateau and no increase in active surface area can be observed. The lowest platinum loading (60% Nafion content) has the thickest Nafion layer surrounding the agglomerates, which imposes a higher mass transport limitation to the active centers and results in current density limitations along the entire potential range investigated.
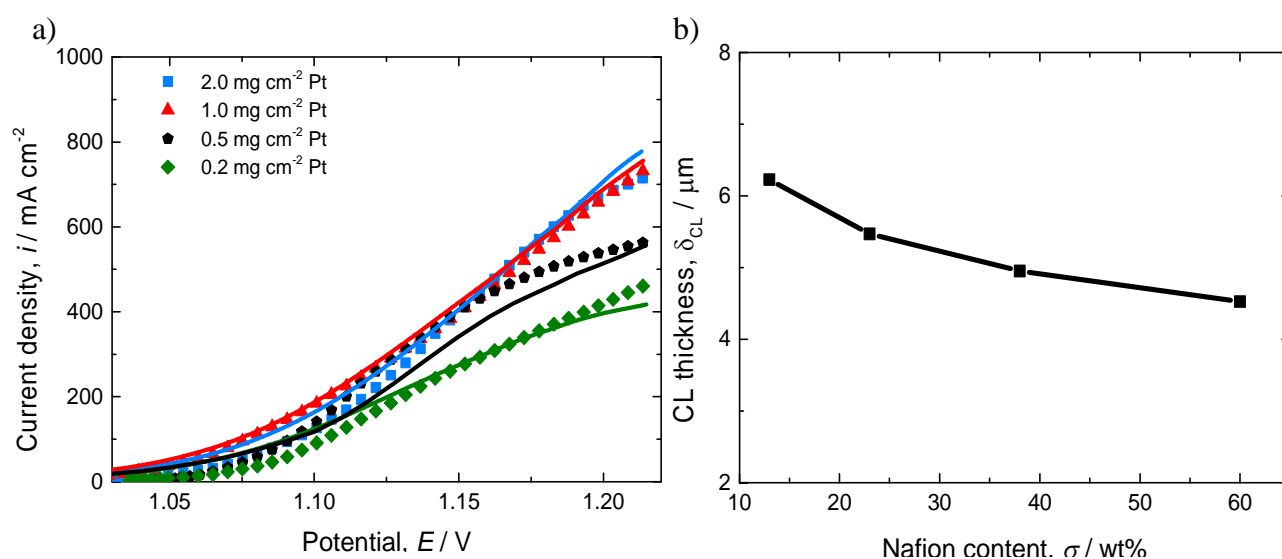

Figure 6-10 Experimental and simulated data for different Pt loadings at a constant 0.5 mg cm^{-2} Nafion loading; b) Dependence of calculated CL thickness on Nafion content in the CL. Conditions as in Figure 6-7.

A thicker Nafion layer leads to lower HCl concentrations inside the agglomerate at the active sites, even though HCl is present in sufficient amount at the CL pores. Hydrogen chloride concentration in the gas phase has influence only on the concentration in the outer part of the Nafion layer, which diminishes through the Nafion film surrounding the agglomerates. This diminishing is proportional to the HCl diffusion in Nafion, eq. (10-23), which is the same for all MEA compositions.

Table 6-4 Agglomerate model parameters for simulations depending on platinum loading

Parameter	Unit	platinum Loading / mg cm^{-2}			
		2.0	1.0	0.5	0.2
j_o^{app}	mA cm^{-2}	10.6	11.3	2.8	7.5
a_{Pt}^o	m^{-1}	6.15E+06	7.55E+06	8.87E+06	9.71E+06
δ_{Naf}	nm	2.57	9.99	20.63	40.67
σ_{Naf}	%	13.0	23.0	37.5	60.0
a_o	m^2 g^{-1}	4.2	4.9	8.3	6.0
ϵ_{CL}	%	10.3	21.2	24.1	28.3

Nevertheless, each MEA has a different thickness of Nafion surrounding the agglomerates, which changes the effective concentration at the Nafion/agglomerate interface. This yields different Nafion profiles inside the agglomerate, as reaction kinetics is a function of a_{Pt}^o, which changes with Nafion loading.

The dimensionless Cl$^-$ concentration profiles $(\bar{c}_{Cl^-} = c_{Cl^-}/c_{Cl^-}^{Naf/Agg})$ are presented as a function of the dimensionless agglomerate thickness $(\bar{\delta}_{agg} = r/r_{Agg})$ in Figure 6-11.
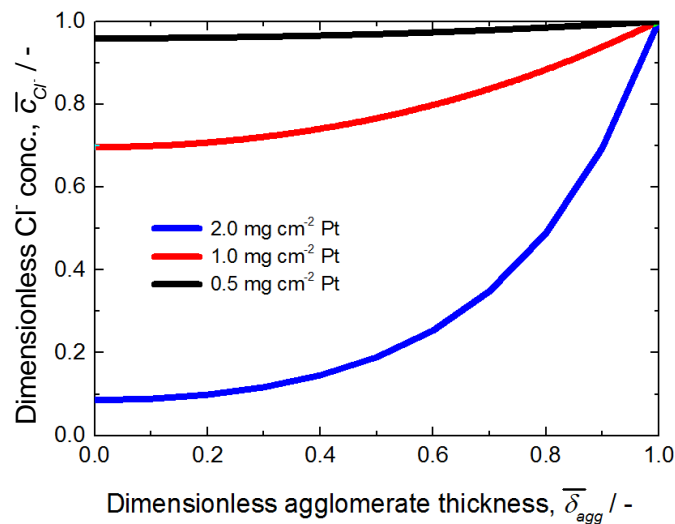
Figure 6-11 Cl$^-$ concentration profiles along the agglomerate for a constant Nafion loading of 0.5 mg cm^{-2} and varying platinum loadings of 0.5 and 2.0 mg cm^{-2} at a potential of 1.15 V. Conditions as in Figure 6-7.

It is observed that higher platinum loadings correspond to higher reactant depletion in the agglomerate, mainly due to the lower diffusion coefficient inside the agglomerate. Even though the complete volume of the agglomerate is employed for the reaction (no complete HCl depletion was obtained), kinetics is slower due to a reduced modified kinetic constant and an increased Thiele module. The former one is proportional to a_{Pt}^o, which increases with decreasing platinum loading, while the latter one is inversely proportional to D_{HCl}^{agg} and has a bigger impact on the Thiele module. This allows the MEAs with 1.0 and 2.0 mA cm^{-2} to achieve nearly the same current density.

It is important to recall that although the concentration profile for the lowest platinum loading is nearly flat, the concentration at the Nafion layer/agglomerate core interface $(c_{Cl^-}^{Naf/Agg})$ is smaller due to the higher thickness of the Nafion layer surrounding the agglomerates, therefore reaching

lower overall current densities as shown in section 5.3.2. With an increase of the platinum loading, values of $c_{Cl^-}^{Naf/Agg}$ are higher as the thickness of the Nafion layer surrounding the agglomerate reduces, allowing a better transport of reactant to the agglomerate core.

Overall, it can be seen that for technical relevant current densities between 350-400 mA cm^{-2}, overpotential reductions up to 80 mV can be achieved by optimization of the platinum loading.

6.4.5.3 Agglomerate porosity

The internal structure of the agglomerates is characterized by the agglomerate porosity ϵ_{agg}, which in case of a sufficient Nafion loading, turns into the agglomerate Nafion content ς_{Naf}. For all investigated parameters in this study, the agglomerates were completely filled with Nafion. This parameter determines the ionic conductivity inside the agglomerates and the diffusion coefficient of HCl inside the agglomerate, as HCl cannot diffuse through platinum or carbon particles.

This parameter was changed in a range of 20% up to 48%, choosing the higher limit by analogy with the simple cubic Bravier crystal structure, as explained in chapter 6.4.5.1. This corresponds to a MEA with 0.5 mg cm^{-2} platinum and 1.0 mg cm^{-2} Nafion. Figure 6-12a shows that current density increases with higher agglomerate porosities. The increase is substantial between 20 and 30%, 210 mA cm^{-2}, from 30 to 40% it is 105 mA cm^{-2}, and between 40 and 48% only 90 mA cm^{-2}.
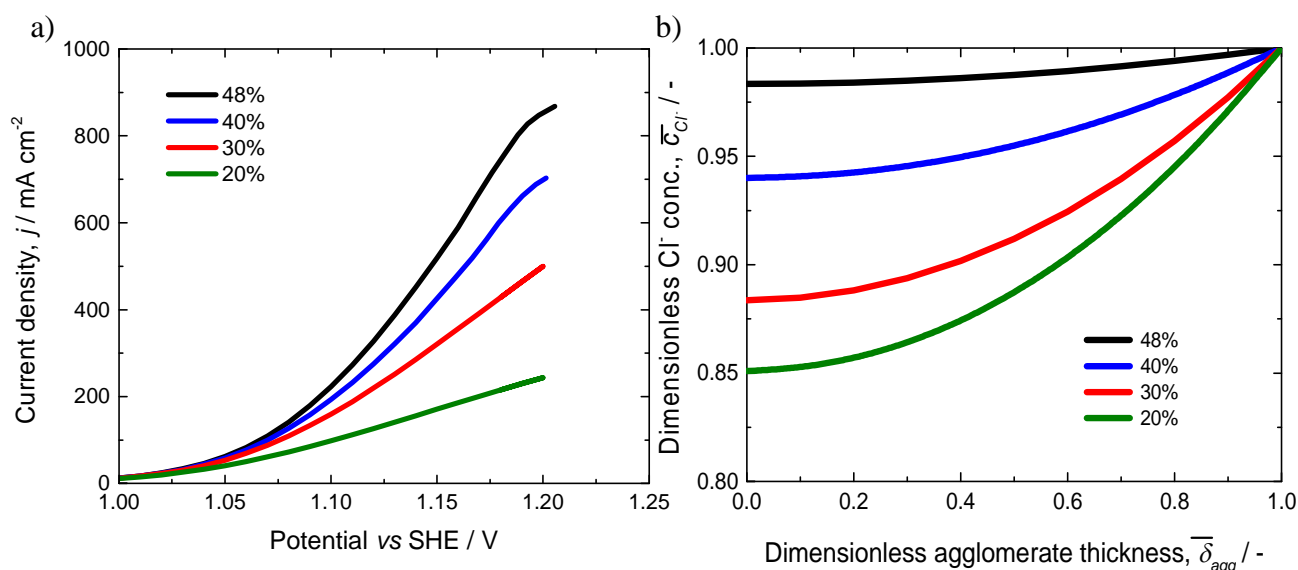

Figure 6-12 Effect of varying agglomerate porosity in a) polarization curves; b) Cl⁻ concentration profiles along the agglomerate at a potential of 1.15 V at a platinum loading of 0.5 and a Nafion loading of 1.0 mg cm⁻². Conditions as in Figure 6-14.

The effects of a higher agglomerate porosity are visible especially at potentials above 1.07 V, as at lower potentials only low current densities are obtained, and thus almost negligible reactant depletion in the agglomerates. A higher agglomerate porosity allows better HCl transport to the core of the agglomerates, allowing for an increased catalyst utilization in comparison to lower Nafion content values, as shown in Figure 6-12a. This has been reported in literature by several authors of agglomerate models for the ORR [117, 118].

As can be seen from the diffusion coefficients presented in Table 6-1, the highest mass transport resistance for HCl transport is found inside the agglomerates, where Nafion is distributed between platinum and carbon particles. Here the effective diffusion coefficient is smaller than in pure Nafion, as it is corrected for tortuosity according to the Bruggeman correlation, eq. (10-16). Analyzing the effective HCl diffusion coefficient in the agglomerate as a function of agglomerate porosity (or agglomerate Nafion content), it ranges from $1.3 \cdot 10^{-12}$ to $7.6 \cdot 10^{-12}$ m^2 s^{-1}, showing almost a seven-fold rise according to eq. (10-16). In a similar fashion, CL ionic conductivity also improves with increasing Nafion agglomerate content while electric conductivity diminishes. Due to the difference in the CL effective electric and ionic conductivity (1339 *vs* 1.15 S m^{-1}), reduction of electric conductivity plays a considerably smaller role than ionic conductivity, which should be the focus for the anodic CL optimization.

6.4.5.4 CL porosity

The effect of CL porosity to current density is shown in Figure 6-12b for values from 10 to 45%. a_{Pt}^o is inversely proportional to CL thickness as shown in eq. (6-19), thus increasing CL porosity diminishes the value of the modified kinetic constant k_{mod}, and therefore the overall reaction rate.
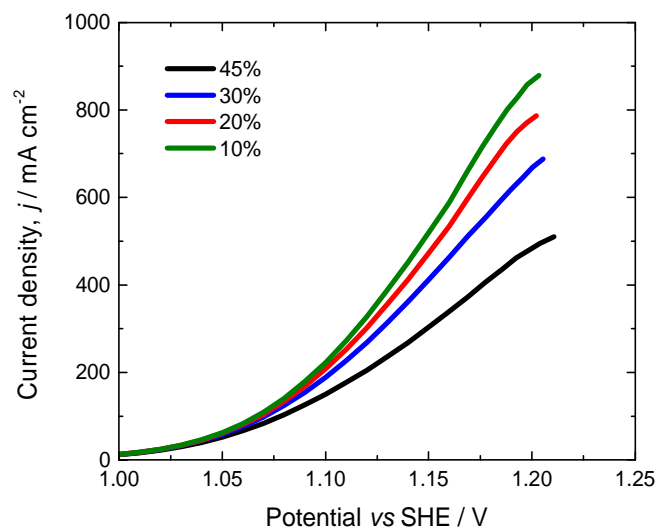

Figure 6-13 Polarization curves as a function of agglomerate for a MEA with 0.5 mg cm^{-2} Pt and 1.0 mg cm^{-2} Nafion. Conditions as in Figure 6-14.

An increase of the CL porosity results in a thicker CL and a smaller solid volume fraction. This affects both electric and ionic conductivities, but allows for a greater hydrogen chloride supply to the CL void/Nafion layer around the outer surface of the agglomerates. Because the main mass transport limitation arises inside the agglomerate and not from the gas-phase transport through the CL gas pores, CL porosity plays a smaller role than the agglomerate porosity.

6.4.5.5 Pt/C ratio

The Pt/C ratio alters the amount of support (in our case Vulcan X72R) present, which influences the amount of agglomerates that can be formed as well as the CL thickness. Simulations were performed keeping a constant Nafion loading of 1.0 mg cm^{-2}, a platinum loading of 1.0 mg cm^{-2}, and varying the Pt/C ratio between 20, 30, 40, and 50%. Results are shown in Figure 6-14a.
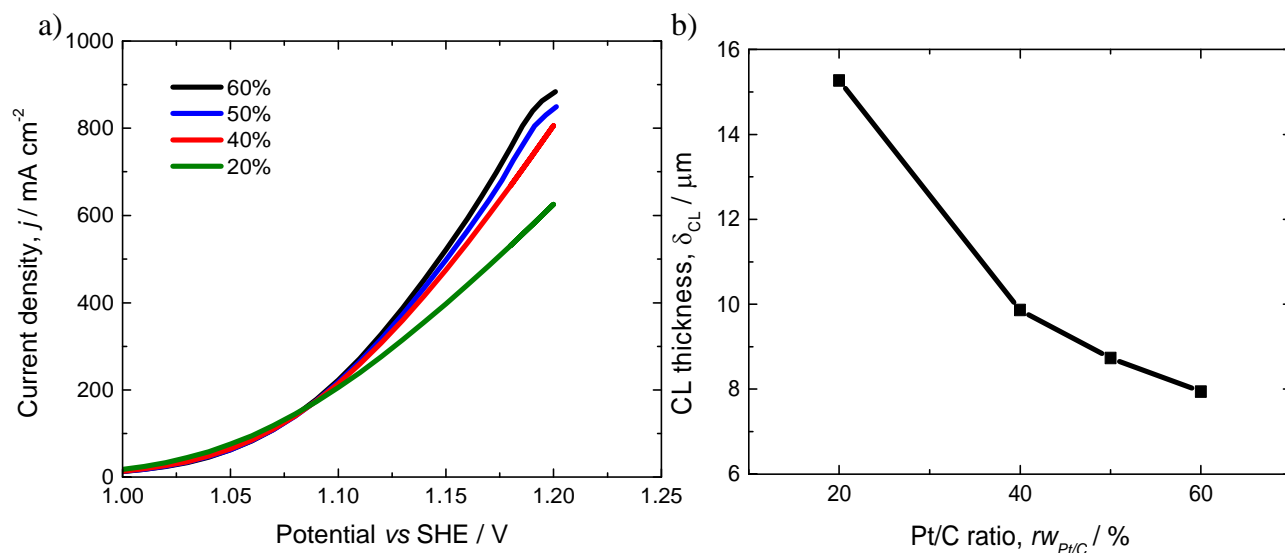

Figure 6-14 a) Polarization curves as a function of the Pt/C ratio. Conditions as in Figure 6-9.

As seen in Figure 6-14a, if the potential is low enough (below 1.07 V), MEAs with lower Pt/C ratios show a better performance. This is attributed to the higher effective specific active surface area. At higher potentials this trend is reversed, as MEAs with higher Pt/C ratios reach higher current densities.

It is important to consider that at high Pt/C ratios the CL layer is thinner and thus gas transport through the CL is improved. As seen in Figure 6-8, the change in the HCL concentration in the CL void is not that considerable as the change inside the agglomerates, which can be in the magnitude of 8% for a change in Pt/C ratio (Figure 6-15) in comparison to 4% at different potentials (Figure 6-8).

It is expected that at high Pt/C ratios a thicker Nafion layer around the agglomerates to be present and therefore higher mass transport resistances, especially at high potentials. This arises from the decreased amount of catalyst to be covered at a fixed Nafion loading. Simulations refute this trend, and show that at higher Pt/C ratios the total amount of carbon and platinum in the CL is reduced at a constant Nafion loading, leading to higher Nafion volume fractions, improving the diffusion coefficient of HCl in the agglomerates. As it was shown for the agglomerate void fraction (section 6.4.5.3), this allows for better catalyst utilization inside the agglomerate. Therefore, at low potentials, where enough reactant is present at the active sites, MEAs with lower Pt/C ratios show the best performance while at higher potentials the opposite effect is observed.
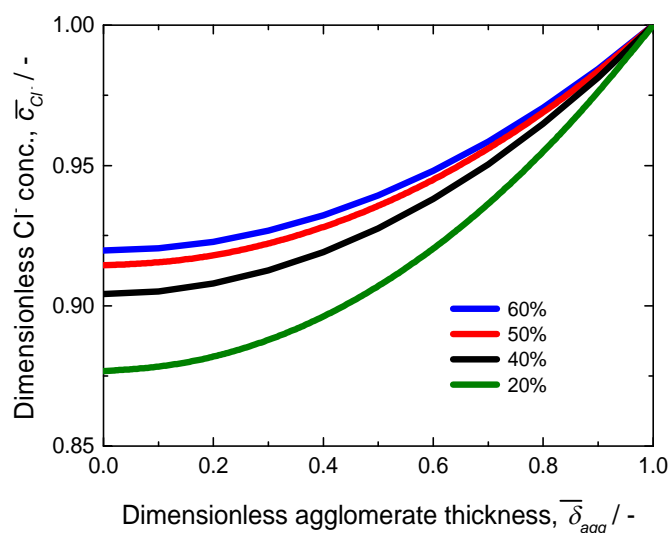
Figure 6-15 Cl⁻ concentration profiles along the agglomerate at a potential of 1.15 V for varying Pt/C ratios at a platinum loading of 0.5 mg cm⁻² and Nafion loading of 0.5 mg cm⁻². Conditions as in Figure 6-14.

6.4.5.6 Agglomerate radius

Agglomerate radii have been reported in literature for MEAs with platinum loadings from 0.5 to 5.0 mg cm⁻² and Nafion loadings from 0.5 to 1.0 mg cm⁻² in the range from 100 to 500 nm [119-121]. Agglomerate radii were investigated in the range from 50 to 500 nm, considering a constant MEA composition of 0.5 mg cm⁻² platinum and 1.0 mg cm⁻² Nafion.

Changing the agglomerate radius changes the CL structure as well as the Nafion distribution in the agglomerates. The amount of Nafion contained inside the agglomerates remains unchanged as well as Nafion remaining to cover the agglomerates, as long as the platinum and carbon total mass remain unchanged. Having smaller agglomerates results in a higher number of agglomerates, yielding thinner Nafion layers surrounding them. This greatly affects the rate of reactant supply to the active sites, as can be observed in Figure 6-16a. An increase in the agglomerate radius from 50 to 500 nm reduces the number of agglomerates by *ca.* three orders of magnitude (see Figure 6-16b), increasing the thickness of the Nafion layer around the agglomerates from roughly 5 to 45 nm.

Table 6-5 CL structural parameters as a function of the agglomerate radius

		Agglomerate radius / nm			
Parameter	Unit	50	100	350	500
j_o^{app}	mA cm⁻²	4.2	4.2	4.2	4.2
a_{Pt}^o	m⁻¹	7.55E+06	7.55E+06	7.55E+06	7.55E+06
δ_{Naf}	nm	4.99	9.95	34.79	45.14
σ_{Naf}	%	37.5	37.5	37.5	37.5
ϵ_{CL}	%	24.1	24.1	24.1	24.1

The qualitative behavior in Figure 6-16a has been reported also by other authors [122, 123], who found out that smaller agglomerates result in higher current densities. An overview of the structural parameters of the CL as a function of the agglomerate radius is presented in Table 6-5.

Isaí González Martínez

It can be noticed in Figure 6-16a, that as the agglomerate radius size increases, total current density decreases. This is in accordance with eq. (6-8), where the second term in the denominator, current density limitation due to reactant transport, is a direct function of the agglomerate radius. The lower current densities are noticeable in the entire potential range investigated.
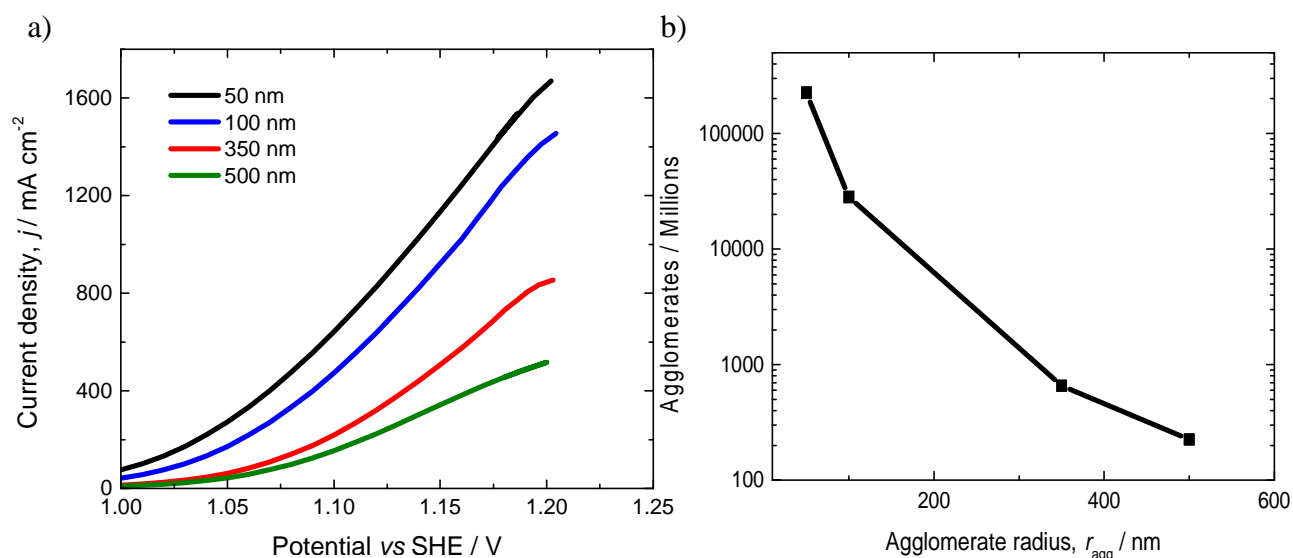

Figure 6-16 a) Polarization curves as a function of agglomerate radius. Conditions as in Figure 6-12.

As shown in Table 6-1, the HCl diffusion coefficient in Nafion is considerably smaller than in the CL, showing that a thicker Nafion layer around the agglomerates has a higher impact in current density than lowering CL porosity. A smaller agglomerate radius also translates into higher Thiele module values, which increased from 94 to 100%. Even though this difference is not striking, it is more accentuated at higher agglomerate radius values as well as higher overpotentials.

It is clear that the agglomerate radius has a great impact on current density, with an optimization potential of about 140 mV. Nevertheless, it is a parameter which can be hardly experimentally controlled and is commonly employed as a fitting parameter in literature [66, 115].

6.4.6 Concluding remarks

As seen in the previous sections, the most important parameters for current density optimization in the anode are the agglomerate Nafion content and the agglomerate radius. The former one affects the diffusion coefficient of HCl inside the agglomerate and thus not only species transport but agglomerate utilization as well. The latter one is a direct indicator of the Nafion layer thickness surrounding the agglomerates (at a given Nafion loading), affecting the reactant transport to the active sites from the gas pores in the CL. Both these parameters can't be directly controlled, and therefore its practical optimization is still not technically viable.

From the controllable parameters, Nafion loading showed the best potential to improve overall current density, followed by the platinum loading. These two parameters can be precisely controlled and influence the non-controllable parameters to some extent, allowing for a direct way to adjust current density.

6.5 Cathode

6.5.1 Governing equations

6.5.1.1 Mass transport

The governing equations for the cathode are analogous to the ones defined for the anode, as both electrodes have the same structure. The only difference is the thickness of the HDL and CL. The former one depends on reactant physical properties (viscosity and density of oxygen and water instead of hydrogen chloride and chlorine), while the former one depends on the platinum and Nafion loadings.

Because Nafion needs to be humidified in order to show ionic conductivity, and the humidification of the cathode feed is the only source of water in the reactor, fully humidified oxygen was considered for all simulation scenarios. The amount of condensed water was directly calculated from the volumetric reaction rate of the ORR. It was further assumed that water imposes no further mass transport resistance for oxygen or clogs the CL pores. The overpotential in the cathode is described analogous to that in the anode.

6.5.2 Boundary conditions

The boundary conditions for the cathode were taken as those defined for the anode. The only difference is that for the boundary at the Agglomerate/Nafion layer with the CL, eq. (6-28), the absorbed oxygen concentration was modeled according to Henry's Law (see Appendix 10.11.1).

Agg Nafion layer/CL void $\qquad r = r_{agg} + \delta_{naf}$ $\qquad c_i^{Naf} = \frac{y_{O_2}p}{H_i}$ (See Appendix 10.11) $\qquad$ (6-31)

6.5.3 Reaction mechanism

For the electrochemical reaction it was assumed that the ORR could be described by a single kinetic expression, in which the reaction order with respect to oxygen was assumed to be one [78, 124]. A single reaction is employed to describe the entire mechanism of the ORR, which has been reviewed elsewhere [45]. Henry's Law is employed to describe oxygen absorption in Nafion and concentrations instead of activities were employed. The reaction can be described by a Tafel formulation:

$$j = j_o \left(\frac{c_{O_2}^{Naf|Agg}}{c_{O_2}^{ref}} \right) \exp\left(-\frac{\alpha F}{RT} \eta_{CL} \right) \qquad (6-32)$$

where j_o stands for exchange current density and $c_{O_2}^{ref}$ for the reference oxygen concentration in the Nafion layer surrounding the agglomerates. The electrochemically active surface area and Thiele module were defined analogous to the ones for the anode. Only the modified kinetic constant for the Thiele module has a different definition in the cathode than in the anode:

$$k_k = a_{Pt}^o \left(\frac{j_o}{zF c_{O_2}^{ref}} \right) exp \left(-\frac{\alpha F}{RT} \eta_{CL} \right) \tag{6-33}$$

The values for the exchange current density were taken from the work of Parathasarathy *et al.* [51, 52] as shown in Table 6-6. These values were employed as they provide a more complete dependence of temperature for the exchange current density as well as transfer coefficient than the ones obtained in this work in chapter 5.4.

Table 6-6 Kinetic parameters for the ORR

Parameter	Value		Units
j_o	$10^{\log(p_{O_2})-7.89} \exp\left[-\frac{E_a}{R} \left(\frac{1}{T} - \frac{1}{323} \right) \right]$	$10^{\log(p_{O_2})-5.64} \exp\left[-\frac{E_a}{R} \left(\frac{1}{T} - \frac{1}{323} \right) \right]$	A m^{-2}
E_a	76.5	27.7	kJ mol^{-1}
α	1	$0.45 + 2.3 \cdot 10^{-3}(T - 300)$	-
Potential range	<0.8 V	>0.8 V	V

6.5.4 Structural effects

The analysis of the structural effects for the ORR was not considered in this work due to the extensive available literature about the ORR. Reviewing the available literature on agglomerate models for the ORR, many authors have reported that the most important parameters affecting current density are the platinum loading, the thickness of the Nafion layer surrounding the agglomerates (indirect measure of the Nafion loading), and the agglomerate porosity [97, 117, 122, 123].

6.6 Membrane

6.6.1 Governing Equations

6.6.1.1 Mass transport

The general mass balance in the membrane is shown in eq. (6-34). As there are no generation or sink terms in this domain, only species transport is considered. The first term on the right-hand side represents convective species transport, the second one diffusion transport, and the third one electroosmotic drag.

$$\epsilon_i \frac{\partial c_i}{\partial t} = -u_i \nabla c_i^m - \nabla N_i^d - \xi N_H^+ = 0 \qquad (6\text{-}34)$$

Convective transport through the membrane was modelled according to Darcy's Law, eq. 6-6. Due to the non-equimolar overall reaction (HClOR-ORR), a pressure gradient on the membrane of up to 0.2 bar at conversions around 100% is expected. Because the actual measured conversions in the reactor in Clausthal lie around 30% and the permeability values through Nafion membranes are extremely small ($1.5 \cdot 10^{-12}$ m^2 [125, 126]), this term is responsible for *ca.* 3% of the overall flux and therefore it was neglected.

For the description of the diffusive flux N_i^d, the Maxwell-Stefan equations for multicomponent mixtures were chosen as species concentrations in the membrane are high, thus species/species as well as membrane/species interactions cannot be neglected. The general Maxwell Stefan formulation is:

$$-\frac{c_i}{RT} \nabla \mu_{i_{T,p}} - \frac{c_i}{RT} \bar{V}_i \nabla p - c_i z_i \frac{F}{RT} \nabla \phi = \sum_{\substack{j=1 \\ j \neq i}}^{n} \frac{x_j N_i^d - x_i N_j^d}{Ð_{i,j}} + \frac{N_i^d}{Ð_i^{Naf}} \qquad (6\text{-}35)$$

where μ_i represents the chemical potential, $\bar{V}_i$ the molar volume, z_i the charge, x_j the mole fraction, N_i the diffusive molar flux, $Ð_{i,j}$ the effective binary diffusion coefficient, and $Ð_i^{Naf}$ the diffusion coefficient of species i in Nafion. The first term on the left-hand side stands for the effect of chemical potential on diffusion at constant temperature and pressure along the membrane. The second term considers the effect of pressure on diffusion at constant temperature, which due to the incorporation of convection in eq. (6-34) was neglected in the Maxwell-Stefan formulation. The third term on the left-hand side of eq. (6-35) stands for the effect of the potential field gradient on charged species transported through the membrane. This term is only valid for protons, as water and HCl are considered to be transported only as neutral molecules. The first term on the right-hand side considers the friction between diffusing components, while the second one considers the friction between diffusing species and the membrane structure.

Chemical potential can be defined by eq. (6-36):

$$\mu_i = \mu_i^o + RT \ln a_i \qquad (6\text{-}36)$$

where μ_i^o represents the chemical potential at standard pressure. In order to employ eq. (6-36) to describe components transported through the membrane, their activities in Nafion are required.

The activity coefficients in the membrane were described with the Flory-Huggins activity model. This model was originally developed for liquid species mixed with polymer solutions. Nevertheless, it has been previously employed in literature to describe species interaction with solid polymer electrolyte membranes [127-129]. A further insight into the different models available for membrane modeling as well as the applicability of the Flory Huggins model is given by Jonquières *et al.* [130]. The activity coefficient of species *i* is given by eq. (6-37):

$$a_i = \epsilon_i \, exp\left(\sum_{k \neq i}\left[\epsilon_k\left(1 - \frac{\overline{V_i}}{\overline{V_k}}\right) + \chi_{i,k}\epsilon_k^2\right] + \frac{\overline{V_i}\epsilon_m^{\frac{1}{3}}}{2N_mV_m}\right) \qquad (6\text{-}37)$$

where ϵ_i stands for the volume fraction of component i, $\overline{V_i}$ for the molar volume, $\chi_{i,k}$ for the non-ideality parameter between species, N_m for the average number of single chain units between two cross-links, and V_m for the molar volume of one single chain of Nafion. In order to calculate activities, the interaction parameters between species (water, hydrochloric acid, and Nafion) are needed. The system HCl-water has been extensively studied and activity formulations are available (see Appendix 10.3.2). Interactions between Nafion and aqueous species ($\chi_{H_2O,Naf}$, $\chi_{HCl,Naf}$) were experimentally determined and are presented in Appendix 10.3.3 together with a more detailed explanation of the activity model. The obtained values of these non-ideality parameters show that water is attracted by the Nafion structure while HCl is repelled by it, thus supporting the assumption that HCl crossover should be small or negligible.

This activity model was not employed for the anodic half-cell because it is computationally more expensive and has the advantage of better describing the effect of HCl interaction with water and the polymer backbone. These effects are not so critical in the CL or agglomerates due to their negligible thickness in comparison with the membrane, which is one order of magnitude thicker than the CL and more than three times thicker than the Nafion layer surrounding the agglomerates.

6.6.1.2 Charge transport

Because in the membrane no charge production or consumption takes place, it behaves like an ohmic resistor. Thus, the conductivity of Nafion in the presence of HCl is required in order to calculate the potential losses through the membrane. In the presence of HCl, water content in Nafion is affected as HCl is repulsed by Nafion as shown by the non-ideality coefficient $\chi_{HCl,M}$ (Appendix 10.3.3). This was confirmed by Motupally, *et al.* [11], who reported that the water content of Nafion decreases linearly with HCl concentration. However, Yeo and McBreen [25] experimentally found out that Nafion conductivity showed a non-linear dependence on HCl concentration. In this work, a polynomial fit of the experimental data from [25] was employed (see Appendix 10.10.1).

Regarding the total potential loss in the membrane, it was defined as:

$$E_l^{mem} = E_{l,cu}^{mem} + E_{l,H^+}^{mem} \qquad (6\text{-}38)$$

where $E_{l,cu}^{mem}$ stands for the ohmic losses through the membrane, defined by eq. (6-39):

$$E_{l,cu}^{mem} = \frac{\delta_{mem}\, j}{\sigma_{Naf}} \tag{6-39}$$

and E_{l,H^+}^{mem} for the Donnan potential through the membrane, due to the proton concentration gradient between the anode and cathode, eq. (2-22). This potential difference is affected by temperature (through the HCl and proton activity), reactant concentration, and the different water contents on each CL (HCl or water absorption in Nafion). The effect of the Donnan potential needs to be taken into consideration for proper reactor modeling as the proton concentration gradient is considerable. The Donnan potential can't be experimentally measured in our setup or be corrected by the potentiostat software, and must therefore be estimated. As mentioned in chapter 6.1, it follows that proton concentration is equal to that of the chlorine ions, which can be explicitly calculated by the activity model presented in Appendix 10.3.

In the case of the half-cell measurements, the base effect of the Donnan potential was taken into account by the use of the open circuit potential instead of the reversible anodic potential. The change in Donnan potential with current density was not considered because of the relatively constant proton concentration gradient through the membrane. This is true in the cathode due to the use of an acidic liquid electrolyte in the counter electrode compartment (providing a considerably higher concentration of protons than a cathodic MEA); in the anode the negligible hydrogen chloride conversion values allow to disregard a change in proton concentration.

For the complete reactor, on the other hand, the effect of protons is more important as the electrode and membrane potentials can't be separated from each other and only total potential through the entire cell can be measured, not allowing to disregard the Donnan potential effect without incurring in a considerable shift of the open circuit potential.

The parameters employed for the simulation of the membrane are presented in Table 6-7.

Table 6-7 Parameters employed for the membrane simulation

Parameter	Symbol	Value	Units	Reference
Nafion density	ρ_{Naf}	~1950	$\mathrm{kg\,m^{-3}}$	calculated
Membrane thickness	δ_{mem}	170		[131]
Single chain units between cross-links	N_m	5	–	[132]
Molar volume of a single Nafion chain	V_m	$5.60 \cdot 10^{-5}$	$\mathrm{m^3 mol^{-1}}$	[132]
Molar volume of Nafion	$\overline{V_m}$	$5.60 \cdot 10^{-4}$	$\mathrm{m^3 mol^{-1}}$	[132]
Non-ideality parameter HCl-Nafion	$\chi_{HCl,M}$	1.45	–	measured
Non-ideality parameter H$_2$O-Nafion	$\chi_{H_2O,M}$	0.77	–	measured
Non-ideality parameter H$_2$O-HCl	$\chi_{H_2O,HCl}$	5.73	–	measured
Molar volume HCl	V_{HCl}	$3.20 \cdot 10^{-5}$	$\mathrm{m^3 mol^{-1}}$	[133]
Molar volume H$_2$O	V_{H_2O}	$1.81 \cdot 10^{-5}$	$\mathrm{m^3 mol^{-1}}$	[108]

1: Conditions for all parameters: 40°C, 1 bar, 100% saturation

2: Nafion 117 was considered for Nafion properties

6.6.2   Boundary conditions

From the assumptions presented for the membrane, no-flow conditions were imposed for chlorine and oxygen. At the interfaces with the CLs flux conservation boundary conditions were employed.

In order to solve the Maxwell-Stefan equation system, the proton flow from the membrane to the cathode was determined from the current density at the cathode, while at the anode, a Dirichlet boundary condition was applied for the known proton concentration.

CL_{an}/Membrane	$x = \delta_{HDL} + \delta_{GDL} + \delta_{CL}$	$-N_{HCl}^{an} = -N_{HCl}^{m}$	(6-40)
		$-N_{H_2O}^{an} = -N_{H_2O}^{m}$	(6-41)
		$c_{HCl}^{an} = c_{H^+}^{m}$	(6-42)
Membrane/CL_{ca}	$x = \delta_{HDL} + \delta_{GDL} + \delta_{CL}$ $+ \delta_{mem}$	$-N_{HCl}^{m} = -N_{HCl}^{ca}$	(6-43)
		$-N_{H_2O}^{m} = -N_{H_2O}^{ca}$	(6-44)
		$-N_{H^+}^{m} = \dfrac{j}{F}$	(6-45)

6.6.3 Effect of current density

Fluxes through the membrane were simulated at three different current densities in the technical plausible range: 300, 400, and 500 mA cm^{-2} at 60°C with 100% hydrogen chloride anodic concentration, 100% oxygen cathodic concentration fully humidified, and flow rates for both species of 500 ml min^{-1}. In accordance to our experimental results (section 5.4.4) and observations from other authors [108], HCl transport from the anode to the cathode was negligible. Concentration dropped in average 100 times through the membrane at all current densities and the profile exhibited a parabolic shape (Figure 6-17a). At higher current densities, in the mixed-control region, the HCl profile took lower values due to the depletion of HCl in the anode.
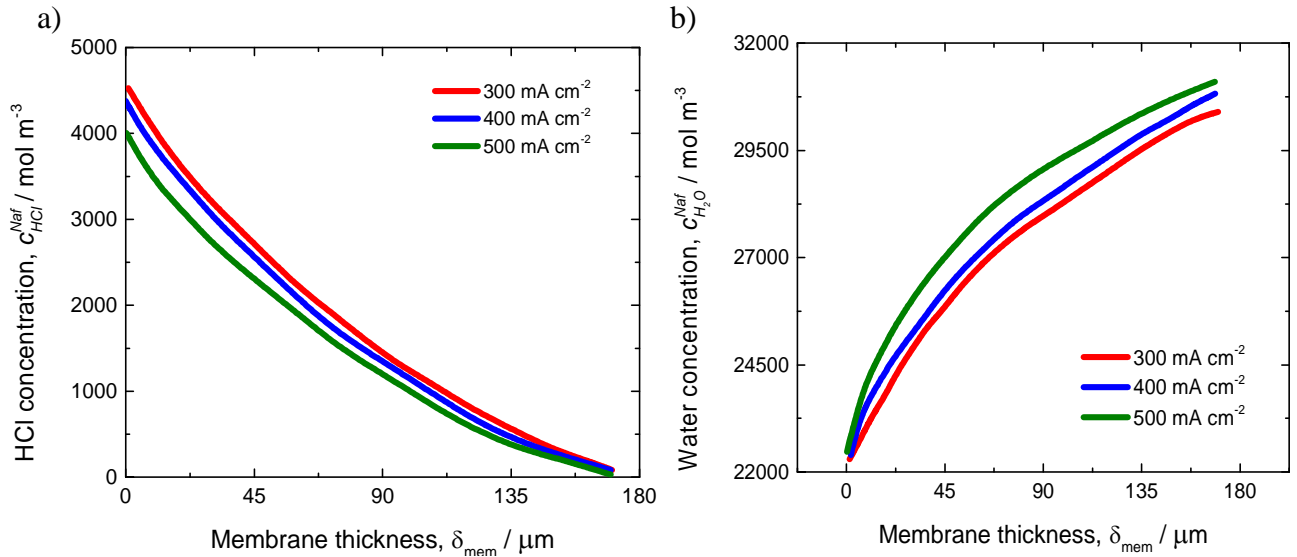
Figure 6-17 Concentration profiles of a) HCl, b) water in Nafion 117. Conditions: 60°C, anodic MEA: 0.5 mg cm^{-2} Pt, 1.0 mg cm^{-2} Nafion; cathodic MEA: 0.5 mg cm^{-2} Pt, 0.5 mg cm^{-2} Nafion. Other conditions as in Figure 5-3.

The water concentration profile, on the other hand, showed an inverted trend when compared with the HCl concentration, as shown in Figure 6-17b. Water attains higher overall values in Nafion due to the sulfonic groups present in its structure. The concentration of water in the cathode increases with current density, as water produced by the ORR condenses due to the use of a fully

humidified cathode gas feed. This results in a higher water concentration along the entire membrane thickness.

It can be seen in Figure 6-17b that an increase in current density yields higher water concentrations at the anode and cathode. The difference between 300 and 400 mA cm^{-2} is not so notorious, but at 500 mA cm^{-2} the profile is considerably higher. This can be explained by the different factors affecting water transport. First, the drop in HCl concentration in the membrane with increasing current density allows more water to be uptaken. Second, at higher current densities more water is dragged by protons to the cathode (3.9 mol water per mol of protons). Third, the fact that HCl and protons diffuse to the cathode means that water molecules come in contact inside the membrane with these two species. Analyzing the binary diffusion coefficients from the Maxwell-Stefan equation, it can be seen in Figure 6-18a that diffusional resistance between water and protons is considerably smaller than between protons and HCl in the entire temperature range. At temperatures above 50°C, the binary H$_2$O/HCl diffusion coefficient becomes higher than that of H$_2$O/H$^+$. The binary HCl/H$^+$ diffusion coefficient increases with temperature, but hydrogen chloride absorption in Nafion decreases with increasing temperature, thus both effects counteract each other.
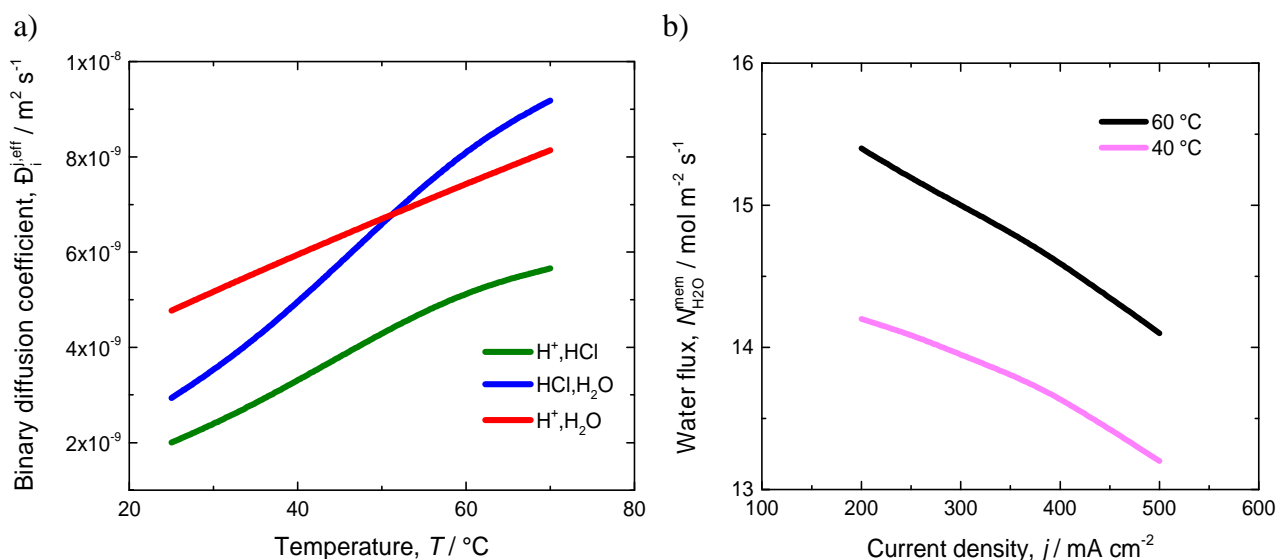
Figure 6-18 a) Binary diffusion coefficients (see Annex 10.5); b) water flux through the membrane as a function of current density. Conditions as in Figure 6-17.

In order to evaluate the impact of these three effects, the total water flux from the cathode to the anode was estimated and presented in Figure 6-18b at 40 and 60°C. A net flux of water from the cathode to the anode was observed, showing that the concentration gradient overwhelms the other two effects. These results are in agreement with those presented by Motupally *et al.* [11, 134], who obtained values in the same order of magnitude for the net water flux through Nafion membranes equilibrated with water and also HCl. Motupally *et al.* [11] considered that water diffusing from the cathode to the anode condensed in the anodic compartment, absorbed HCl and then was driven out of the cell. Because of the high gas fluxes employed in this work, it was

considered that no water condensation took place in the anode and excessive water was carried away as vapour by the high hydrogen chloride flow rate in the anodic compartment.

A change in both water and HCl concentrations translates into a change in the conductivity of Nafion and thus into membrane potential losses. These losses are presented in Figure 6-19a, without the effect of the Donnan potential. It is observed that the resistance of the membrane increases at the interface with the anode, where the highest HCl and lower water concentrations are present.
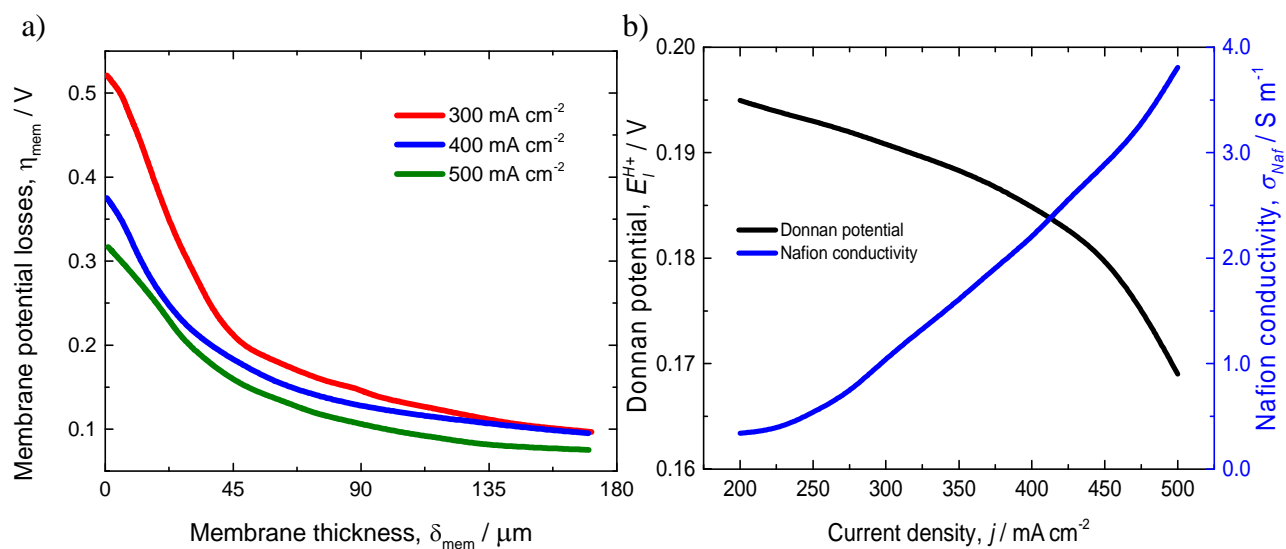
Figure 6-19 a) Potential loss along the membrane; b) Donnan potential and Nafion conductivity of Nafion 117.

Because no charge generation or consumption takes place in the membrane, ohmic losses should follow Ohm's law, which predicts a higher potential loss at higher currents, contrary to results from Figure 6-19a. Under consideration that the membrane thickness δ_{mem} remains constant and current density increases, the conductivity of the membrane σ_{mem} must increase to explain the lower ohmic losses. This phenomenon can be associated to an increase in the water uptake of the membrane, which is inversely proportional to that of the potential losses (Figure 6-19a). Nafion uptakes different amounts of water when contacted with water vapor or liquid water. Higher conductivity values are obtained when contacted with liquid water. In the reactor, no liquid water is fed, but water generation (and thus condensation) from the ORR increases in the cathode with rising current density, therefore allowing for higher water uptake values at higher current densities. This increases the membrane conductivity near the cathode as more water is present and also diluting HCl (see Figure 10-3). Higher losses are observed near the anode, where the water profile reaches its lowest value.

The Donnan potential (shown in Figure 6-19b) also diminishes with increasing current density, as the proton concentration further decreases with HCl depletion in the anode (and consequent water generation in the cathode), which has a higher influence at current densities above 450 mA cm^{-2} due to the non-linear equilibrium of the HCl-H$_2$O system. The change in Donnan potential was

found to be around 30 mV in the current density range from 200-500 mA cm^{-2}, having a lesser impact in total potential loss through the membrane than the change in Nafion conductivity.

6.7   Complete reactor

For the complete reactor model, the single modules developed in this work (anode, cathode, and membrane) were coupled. The governing equations remained the same, but the boundary conditions undertook some changes to allow continuity through the boundaries of the single modules.

6.7.1   Governing Equations

The mass balances shown for the anode and cathode in chapters 6.4 and 6.5 were employed for the reactor model. An additional equation to define total reactor potential with current density was defined: the reversible cell potential minus the potential losses associated to the cathode, anode, and membrane [135]:

$$U = E_{rev}^{ca} - E_{rev}^{an} - |\eta_{ca}| - |\eta_{an}| - E_l^{mem} \tag{6-46}$$

6.7.2   Boundary conditions

The boundary conditions employed for the reactor simulation were the same as for the single electrodes, only eq. (6-27) was changed from a no-flow to a continuity boundary condition:

CL$_{an}$/Membrane	$x = \delta_{HDL}^{an} + \delta_{GDL} + \delta_{CL}^{an}$	$-N_i^{CL,an} = -N_i^{mem}$	(6-47)
CL$_{ca}$/Membrane	$x = \delta_{HDL}^{an} + \delta_{GDL} + \delta_{CL}^{an} + \delta_{mem} + \delta_{CL}^{ca} + \delta_{GDL}$	$-N_i^{CL,ca} = -N_i^{mem}$	(6-48)

6.7.3   Experimental results

The anodic HClOR together with the cathodic ORR were measured in a 30 cm^2 reactor in the TU Clausthal. MEAs having the same compositions as those in the present work were employed. The reactor was operated at 100% hydrogen chloride and 100% oxygen concentration at temperatures of 25, 40, 50 and 60°C. Water saturation of the gas feeds was 0% for the anode and 100% for the cathode. The resulting polarization curves are presented in Figure 6-20.

These results present the proof of principle for the direct hydrogen chloride electrolysis with an oxygen-depolarized cathode. It is the first time measurements have been presented with operating cell potentials below 1 V at a technically relevant current density of 400 mA cm^{-2} [136]. It is important to note that this was obtained at temperatures below 50°C, whereas industrial standards operate between 60 and 80°C. The low reaction temperatures and achieved reactor potentials make this process variant even more attractive for a technical application.

It was noticed that the polarization curves show three polarization regions analogous to fuel cells: the activation, ohmic, and limiting current density regions. The activation region, where reaction kinetics determines current density, was observed at current densities below 80 and 100

mA cm^{-2}. Afterwards, a region where ohmic losses through the membrane mainly determine current density was identified up to values of 320-400 mA cm^{-2}. The limiting current density region was observed for all temperatures, starting at current densities ranging from 350 mA cm^{-2} up to 400 mA cm^{-2}.
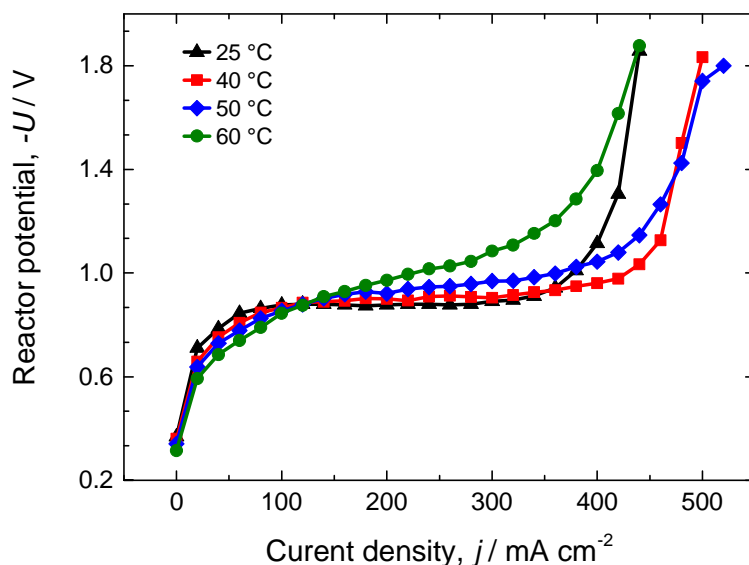

Figure 6-20 Reactor polarization curves. Conditions: hydrogen chloride and oxygen concentration: 100%, anodic MEA: 0.5 mg cm^{-2} Pt, 1.0 mg cm^{-2} Nafion; cathodic MEA: 0.5 mg cm^{-2} Pt, 0.5 mg cm^{-2} Nafion. Anode and cathode flow rates: 600 ml/s. Cathode feed relative humidity: 100%.

At the moment it is not completely clear which factor is responsible for the limitation of current density: mass transport limitation of educts to the electrodes, difficult product removal from the catalytic surface, deviation from isothermal conditions, etc. From the polarization curves it can be seen that a change of the reactor operation temperature plays a big role in the overall shape and extension of the different regions.

For the activation region, a raise in temperature increases the reaction rates by lowering the activation overpotentials at both electrodes, resulting in a decrease of the cell potential. For the ohmic region the behavior is more complex. For the curves at 25°C and 40°C, the rise in cell potential with increasing current density is almost negligible, allowing for a reactor operation at potentials below 1 V (0.969 V) up to *ca.* 350-400 mA cm^{-2}. For higher temperatures, the increase in the ohmic region was more pronounced and potentials above 1 V were measured at current densities of 360 and 280 mA cm^{-2}, respectively. The limiting current density region was found to start at lower current densities for the curves at 25°C and 60°C, while for the ones at 40°C and 50°C it started at higher values.

6.7.4   Open circuit potential (OCP) analysis

OCP was measured experimentally under zero-current conditions. According to thermodynamics, a reversible cell potential of 0.24 V at a temperature of 25°C is expected for this process. Nevertheless, negative OCPs in the range of -0.36 and -0.31 V were measured in the reactor (Figure 6-21a) at all temperatures [136]. Recalling section 2.3, reversible cell potentials of 0.24,

0.23, 0.23, and 0.21 V are expected for temperatures of 25, 40, 50, and 60°C. The difference between thermodynamics and measurements is approximately 0.58 V.
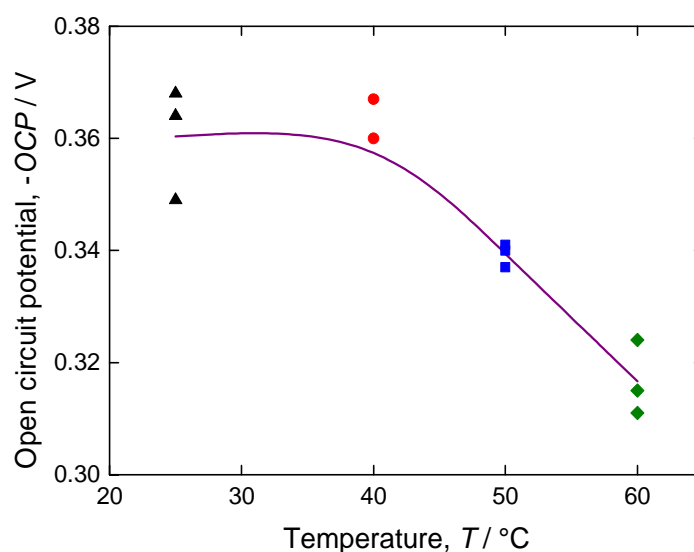
Figure 6-21 Experimental OCP as a function of temperature. Conditions as in Figure 6-20.

One of the reasons for this deviation is the loss caused by the ORR, which is also known from several half-cell and fuel cell studies [137]. While the reversible potential for the ORR is 1.23 V, as seen in section 2.2 and in literature [38, 138, 139], the maximal measurable OCP from half-cell experiments lies between values of 0.90 and 1.05 V. These losses are commonly associated to irreversibilities of the ORR due to a mixed potential from a platinum/platinum oxide catalyst surface [45, 124]. Another reason for this was presented by Zhang *et al.* [137], who pointed out that the use of humidified gaseous feeds reduce the effective oxygen concentration, lowering the OCP. The behavior of the partial pressure of water with temperature is exponential, and it is considered only in some cathode models in literature and in this work, allowing to better estimate the OCP, as the experimental values obtained were considerably lower than thermodynamic values.

An additional reason is the Donnan potential caused by the proton gradient across the membrane. It is assumed that the proton concentration at the membrane/anodic CL is dictated by the dissociation of HCl into chloride and protons. Because the Donnan potential was not measured in our setup, it was estimated by means of eq. (2-22).

As shown in eq. (6-46), the potential losses were analyzed in our reactor model, which allowed separating the contributions of the anode, cathode, and membrane. Potential losses in the reactor were modeled and presented in Figure 6-22. Considering the above mentioned contributions to the OCP, the calculated values deviate *ca.* 60 mV from the experimental values. In Figure 6-22b it is observed that the contribution of the proton concentration gradient is of the same magnitude as the OCP deviation of the ORR from its reversible potential. This is a very important consideration in our system due to the highly different acidic conditions at the membrane boundaries. Even though there is still a difference of 60 mV between simulated and experimental data, it can be considered as a good first estimation.
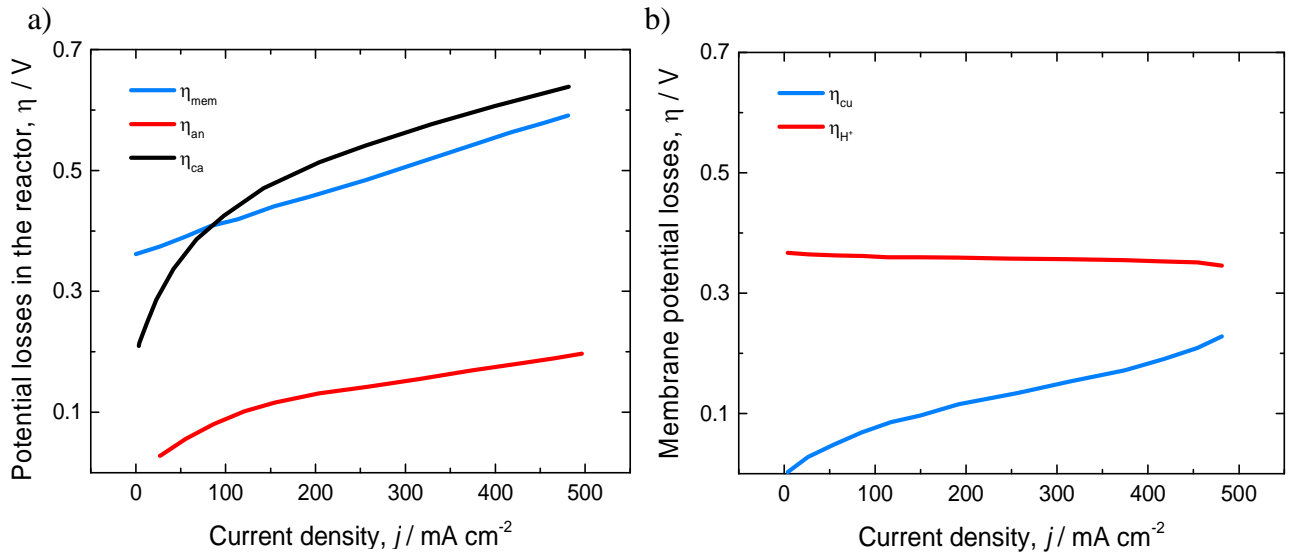
Figure 6-22 Potential losses at 40°C in the a) reactor; b) membrane. Conditions as in Figure 6-20.

6.7.5 Cell potential analysis

The reactor model developed in this work was able to describe the activation and ohmic regions of the measured reactor polarization curves, as shown in Figure 6-23. The slope of the ohmic region was found to be anomalously small, which could be traced back to an increase of the membrane conductivity due to water transport/condensation from the ORR (see section 6.6.3). Even though for fuel cells the ORR is also used as the cathodic reaction, such a small slope has not been reported. This could be traced back to the influence of HCl in the ionic conductivity of Nafion. Higher HCl concentrations in the membrane reduce the ionic conductivity. A higher water flux from the cathode to the anode not only improves Nafion conductivity by providing a higher water uptake, but also dilutes HCl and thus increases conductivity to a further extent than in fuel cells.
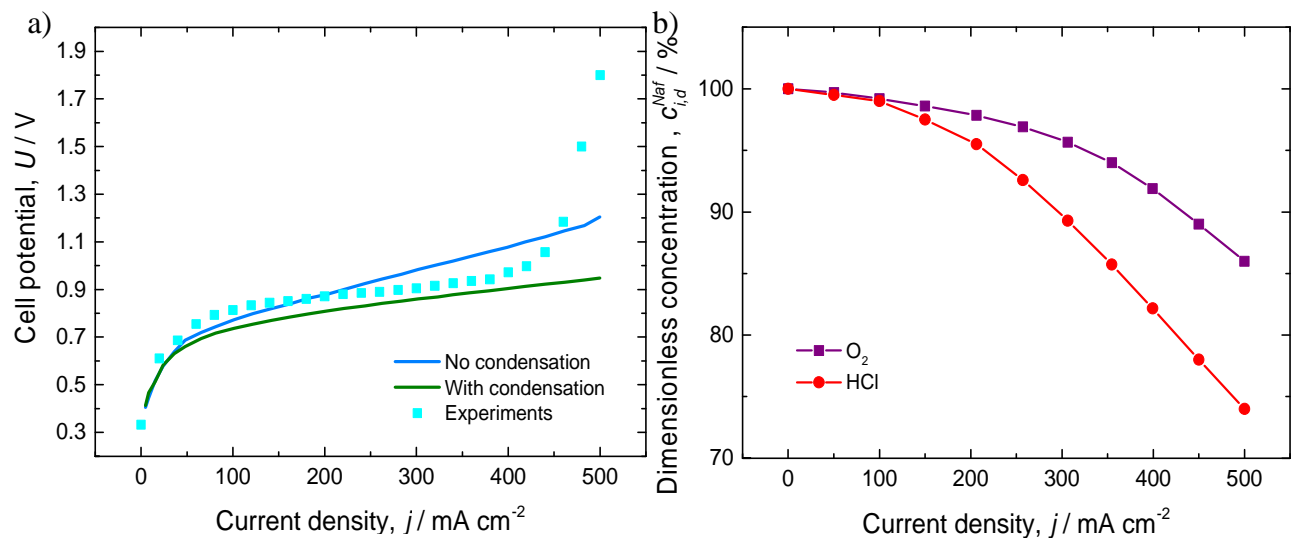
Figure 6-23 a) Polarization curves considering water condensation and no water condensation in the cathode; b) Reactant dimensionless concentration as a function of current density. Conditions as in Figure 6-22.

From the modeling point of view, commonly water condensation is bounded to the mass transfer of oxygen to the active sites at high potentials. One of the advantages of the agglomerate

model is that it doesn't require the definition of two-phase flow in order to describe this region due to the consideration of the Nafion layer surrounding the agglomerates, which in the case of the ORR provides an excellent agreement with measurements [66].

In order to visualize the effect of water condensation on the cell potential, in Figure 6-23a polarization curves were simulated neglecting and considering water condensation. Quantitative agreement between experiments and simulations improves dramatically under consideration of water condensation in the industrial relevant current density region. Neglecting water condensation results in a steeper increase of cell potential than shown by experiments. According to the model, the experimentally measured increase in cell potential at current densities above 400 mA cm^{-2} is not due to reactant concentration depletion. To support this, the concentrations of educts at the agglomerate/CL void boundary were normalized to the concentrations at OCP conditions and plotted as a function of current density in Figure 6-23b. It can be seen that reactant depletion doesn't surpass 15 and 28% for the ORR and HClOR respectively. At current densities below 500 mA cm^{-2}, polarization curves from half-cell investigations still didn't reach the limiting current density region (Figure 5-5, Figure 5-6, and Figure 5-14), hinting to an effect not present in such experiments but only in the reactor. It is speculated that non-isothermal conditions in the reactor could be the reason, resulting in membrane or CL dehydration at higher current densities due to the lack of a supporting electrolyte which could take away the reaction heat produced and keep the membrane properly hydrated.

6.7.6   Reactor optimization

The influence of anode and cathode structural parameters on the rector performance has been studied in simulations. This was done because the MEA structure can be easily modified by changing the Nafion and platinum loadings, which can be controlled in a readily and reproducible manner. From Figure 6-22a it can be seen that the higher potential losses arise from the cathode and membrane along the entire cell potential range, which are responsible for about 45% and 41% of the total potential losses respectively. MEA structures of the anode and cathode were varied in a Nafion content range of 13 to 71%. This was obtained by changing platinum loadings from 0.2 mg cm^{-2} to 2.0 mg cm^{-2} and Nafion loadings from 0.5 to 2.0 cm^{-2}.

6.7.6.1   Optimization of the anode structure

Although it was previously shown in Figure 6-23a that the HClOR contributes only with 15% to the total potential loss at 400 mA cm^{-2} and its kinetics is fast, a change in the anodic MEA structure represents an easy way to further improve the cell potential. In Figure 6-24, the polarization curves for varying anodic MEA structures and a cathodic MEA with a constant composition of 0.5 mg cm^{-2} platinum and 1.0 mg cm^{-2} Nafion (55% Nafion content) are presented. The effect of changing the anodic Nafion loading was analyzed in Figure 6-24a at a constant platinum loading of 0.5 mg cm^{-2} and in Figure 6-24b at a constant Nafion loading of 0.5 mg cm^{-2}. It is shown that the maximal deviation in cell potential between the best MEA (55% Nafion content) and the worst one (60%

Nafion) was 89 mV. The worst performance was shown by the MEA with 60% Nafion, which is consistent with results shown in chapter 5.3.2 for the MEA with 0.2 mg cm^{-2} Pt and 0.5 mg cm^{-2} Nafion. The difference in performance between MEAs with 13, 23, 55, and 71% was very small (<10 mV).
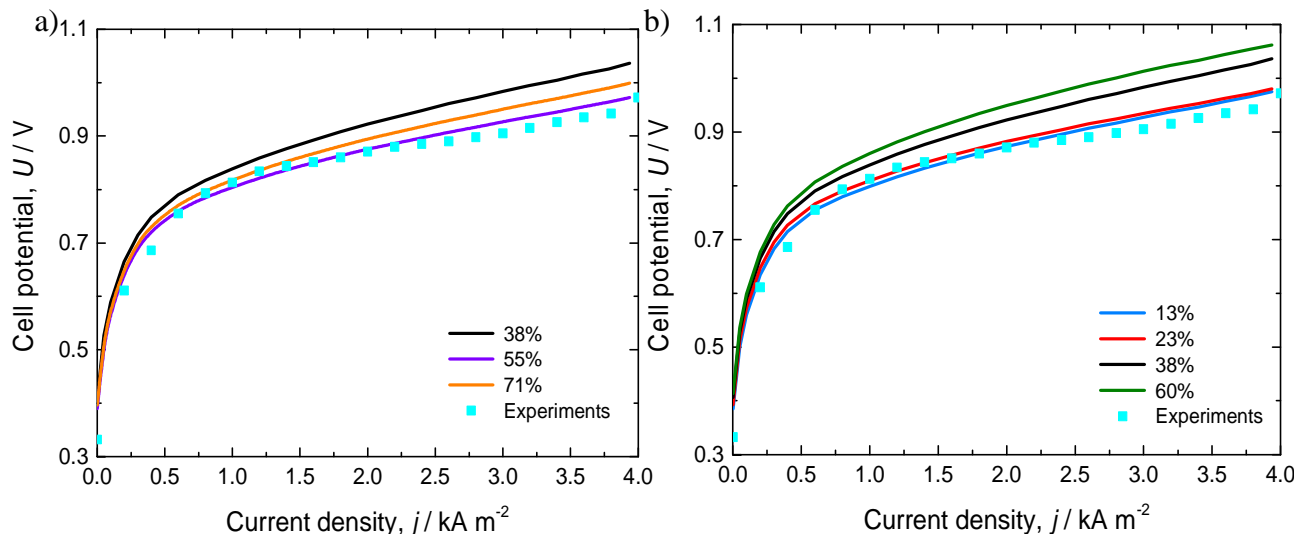

Figure 6-24 Polarization curves for a reactor comprising a cathodic MEA with 0.5 mg cm^{-2} Pt, 1.0 mg cm^{-2} Nafion (55% Nafion content) and an anodic MEA with a) constant Pt loading of 0.5 mg cm^{-2}; b) constant Nafion loading of 0.5 mg cm^{-2} . Conditions as in Figure 6-22.

The Nafion content on the cathode side was changed from 55% to 13% and anode structural parameters were optimized again, with results presented in Figure 6-25.
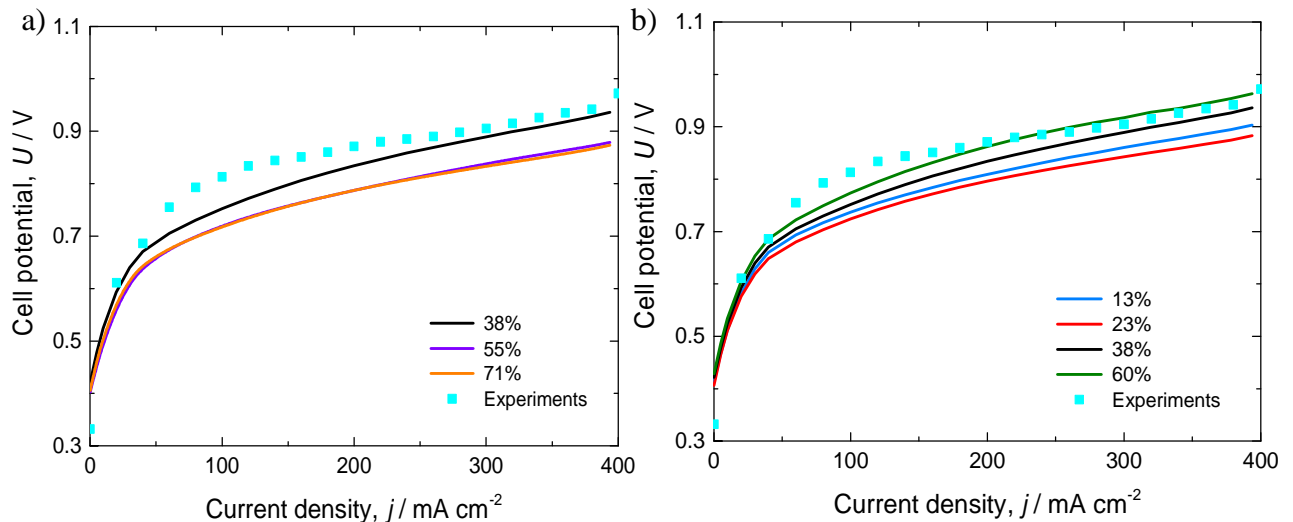
Figure 6-25 Polarization curves for a reactor comprising a cathodic MEA with 2.0 mg cm^{-2} Pt, 1.0 mg cm^{-2} Nafion (13% Nafion content) and an anodic MEA with a) constant Pt loading of 0.5 mg cm^{-2} and varying Nafion loadings; b) constant Nafion loading of 0.5 mg cm^{-2} and varying Pt loadings. Conditions as in Figure 6-22.

In this case, the worst performance was still shown by the MEA with 60% Nafion content, but the best performance was marginally obtained by the MEA with 71% Nafion content. Recalling the catalyst utilization presented in chapters 5.3.2 and 5.3.3, it was shown that at current densities below 500 mA cm^{-2}, a higher Nafion loading translates into higher catalyst utilization. It is important to mention that higher catalyst utilization doesn't directly renders considerable current density

improvements, but other aspects, *i.e.* a more cost effective MEA with reduced catalyst loadings per current ratios.

Considering this and results presented in Figure 6-24a, an increase in the anodic Nafion loading from 0.5 to 2.0 mg cm^{-2} delivers more or less the same cell potential reduction as an increase in platinum loading from 0.2 to 2.0 mg cm^{-2}. Therefore an increase of the Nafion loading is preferred as it represents a lower MEA cost and helps improving the ionic conductivity of the anodic CL, which is more prone to lower ionic conductivity due to the use of anhydrous gas as an educt.

The performance of a reactor operating with the HClOR and ORR can thus be improved up to *ca.* 80 mV at 400 mA cm^{-2} by changing the anodic CL composition.

6.7.6.2 Optimization of the cathode structure

From the ORR experiments it was discussed that at a technical current density of 400 mA cm^{-2} the MEA showing the best performance (35% Nafion content) required overpotentials of *ca.* 950 mV. In fuel cell literature [38, 45, 47, 66, 124], overpotentials required to reach such current densities range between 400 and 600 mV at 60°C. As can be seen the main kinetic bottleneck is the ORR. Results from simulating variable cathodic MEA composition with an optimized anodic MEA comprising 0.5 mg cm^{-2} platinum and 1.0 mg cm^{-2} Nafion (55% Nafion content) are shown in Figure 6-26, where they are compared with experimental data extracted from Figure 6-20.
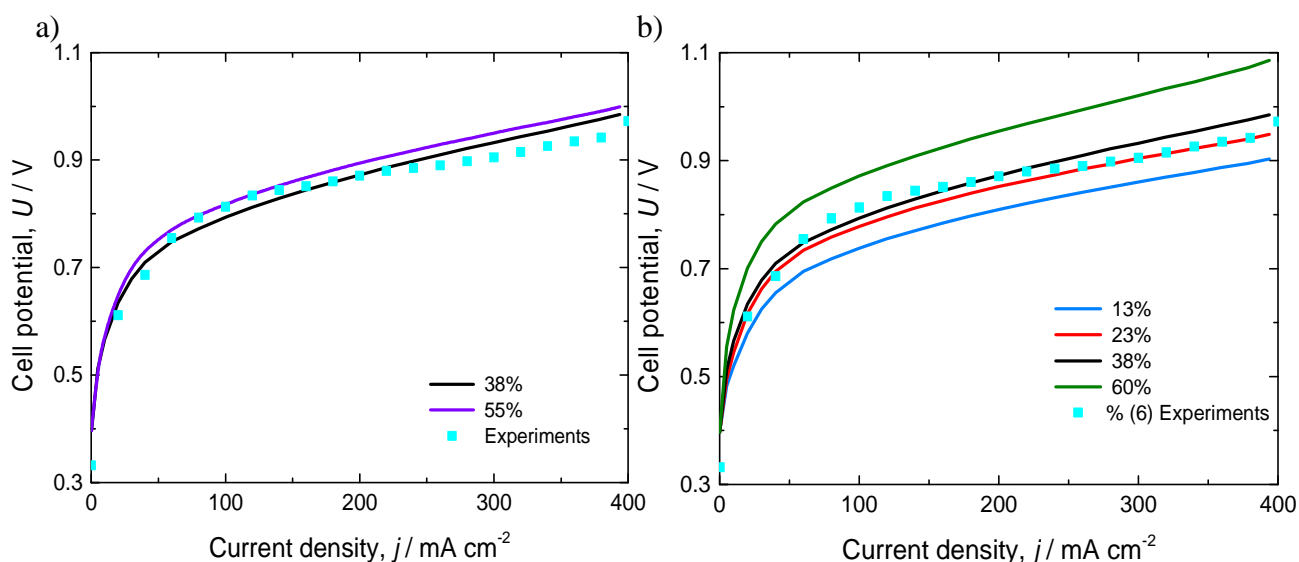
Figure 6-26 Polarization curves for a reactor comprising a cathodic MEA with 2.0 mg cm^{-2} Pt, 1.0 mg cm^{-2} Nafion (13% Nafion content) and an anodic MEA with a) constant Pt loading of 0.5 mg cm^{-2} and varying Nafion loadings; b) constant Nafion loading of 0.5 mg cm^{-2} and varying Pt loadings. Conditions as in Figure 6-22.

In experiments presented in section 5.4.1, Nafion loadings were investigated only in the range from 35 to 71% Nafion content, showing that lower values were more suitable for the ORR. According to the literature, the ORR shows a maximum performance around Nafion content values of 30-35% [38]. Nevertheless, experimental and theoretical work regarding Nafion content are

usually done with a fixed platinum loading and varying only the Nafion loading or vice versa. Keeping a constant platinum loading allows to reduce the Nafion loading up to the point of disruption of the ionic conducting network, which would lead to a very thin CL, as the density of platinum is considerably higher than that of Nafion.

By increasing the platinum loading at constant Nafion loading the same effect will be observed but the MEA cost would be considerably higher. Therefore, by simultaneously changing both loadings it is possible to reach an optimum Nafion content different than 30-35% when comparing current densities. The use of mass-normalized currents is discouraged, because as mentioned in section 5.3.2, they point out the best catalyst utilization and not precisely the highest current density.

From these results it can be observed that the difference in cell potential between a MEA with 38% and 60% Nafion content is 100 mV, leading to cell potentials of 0.985 and 1.085 V respectively. A further increase of the platinum loading leads to a decrease in Nafion content, yielding an optimum at 13% Nafion with an additional cell potential reduction of 82 mV at 400 mA cm^{-2}. This MEA consists of 2.0 mg cm^{-2} platinum and 0.5 mg cm^{-2} Nafion. Increasing the catalyst loading directly increases exchange current density allowing for lower potentials in the activation region without a considerable increase of the CL thickness, which could lead to reactant depletion in the CL. Therefore, choosing the right MEA structure could lead to a reduction in cell potential of up to 182 mV.

7 Economic Analysis

In this section, an estimation of the economic impact of this novel chlorine recycling process has been carried out. This analysis considers only the energetics of the electrochemical reactor. It should be kept in mind that more detailed analysis should also include the energetic analysis of pre- and post-processing steps to the electrochemical reactor (feed purification, compression, pumping, product separations, etc.).

7.1 HCl recycling processes: electrolyzer

The most important cost indicator of an electrolyzer is the specific energy consumption per ton of chlorine, W_{Cl_2}, which is described by eq. (7-1):

$$W_{Cl_2} = \frac{z \, F \, U}{M_{Cl_2}}$$
(7-1)

where M_{Cl_2} stands for the molecular weight of chlorine and U for the reactor potential. Considering that the process studied in this work can be operated at cell potentials as low as 971 mV and a technical current density of 400 mA cm^{-2}, a specific energy consumption of 735 kWh ton Cl$_2^{-1}$ can be calculated. In comparison to values obtained for other available process for chlorine recycling, the energy savings considering only the electrolyzer lie around 50%.

Table 7-1 Cost comparison of the processes for Chlorine production from HCl recycling

Parameter	Units	Bayer-Uhde-Hoechst	Dupont-Denora	Bayer-Uhdenora	This work
Typical cell potential	V	-2.00	-1.60	-1.35	-0.97[1]
Typical current density	A m^{-2}	4.00	10.00	4.00	4.00
Energy consumption	kWh/ton Cl$_2$	1513	1211	1021	735
Cost[2]	€/ton Cl$_2$	7.57	6.05	5.11	3.67
Energy saving[3]	%	0%	20%	33%	51%

[1] Values are calculated for 60°C, 1M HCl or 101.3 kPa
[2] The energy cost associated to generate a ton of Cl$_2$ was calculated employing an energy value of 5€ MWh^{-1} [9].
[3] Compared to the industrial standard process, the Bayer-Uhde-Hoechst process

Considering that product gas stream of the process studied in this work consists mainly of unreacted hydrogen chloride, chlorine, and water, a separation scheme has to be developed. Commonly, gas washing with water is employed to absorb unreacted hydrogen chloride due to its affinity to absorb as hydrochloric acid and the low chlorine absorption due to the acidic pH. This would yield hydrochloric acid, which is not desired as unreacted hydrogen chloride could be recirculated to the reactor. In case gas washing is employed as a separation method, a liquid HCl electrolysis unit can be placed after the hydrogen chloride reactor, as done for the Dupont-Denora process in order to avoid more complex separation alternatives such as gas absorption [5], which only work at considerably low hydrogen chloride concentrations (<10%). With this consideration,

total separation costs should not differ much between the four processes, as they all employ the same principle with the same components in the gas stream, just with different hydrogen chloride proportions [5].

Another possibility is to implement the separation scheme employed by the DuPont-DeNora process [140], in which the product gas stream is first dried with concentrated sulfuric acid, then compressed to 850 kPa and cooled down. The liquefied mixture is then distillated at 2400 kPa, obtaining hydrogen chloride and inerts from the column's top and liquefied chlorine from the bottom. The equipment requirements and utility consumptions for this separation scheme are considerably higher than those for the gas stream washing with water, thus rendering the choice of this separation scheme less economically attractive.

7.2   Study case: diisocyanate production

In order to estimate the possible energy savings related to the use of the process investigated in this work, a study case was chosen: the isocyanate production. This process is the second largest industrial process employing chlorine with a 29.4% industry share in Germany [3]. Chlorine reacts with carbon monoxide to produce phosgene, which later reacts with amines to produce isocyanate and hydrogen chloride as a byproduct [141].

The two most commonly used isocyanates are methylenediphenyl diisocyanate (MDI) and toluene diisocyanate (TDI), which are employed as precursors for polycondensation reactions to produce polyurethanes, polyureas, polyamides, and polyimides. In this process all chloride employed is transformed into hydrogen chloride, which is poisonous and corrosive [142], yielding 4 moles of HCl per mole MDI or TDI.

$$CO_{(g)} + Cl_{2(g)} \rightarrow COCl_{2(g)} \tag{7-2}$$

$$COCl_{2(g)} + R - NH_2 \rightarrow R - N = C = O + 2HCl_{(g)} \tag{7-3}$$
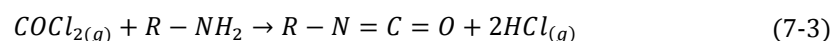
Hydrogen chloride waste can be reduced by using the oxychlorination reaction to generate EDC:

$$C_2H_{4(g)} + 4HCl_{(g)} + O_{2(g)} \rightarrow C_2H_4Cl_{2(g)} + 2H_2O_{(g)} \tag{7-4}$$
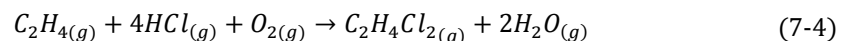
which can be thermally cracked to VCM and further recycled to PVC. Nevertheless, some hydrogen chloride is still left unreacted, which is commonly absorbed in water to produce hydrochloric acid due to the big gas volumes employed. This reaction is limited by equilibrium with a maximal HCl concentration of about 22 wt.%. The hydrochloric acid market is already saturated and large areas are required for its storage, as the plastic industry demand grows faster than the one for hydrochloric acid. HCl disposal is commonly done by neutralizing it to sodium chloride with caustic soda. Nevertheless, salt content in waste water dumped in industrial sewer systems is highly restricted in Europe [143].

The European yearly production capacity for MDI and p-MDI in 2013 was estimated to be 2.55 million tons [144, 145]. Because of the high amount of hydrogen chloride produced, commercial-

grade hydrochloric acid is manufactured and considered a desired byproduct. Only around 14% of all produced HCl is considered as waste and has the potential of being recycled to chlorine.

Currently, several processes for the electrochemical conversion of HCl to chlorine exist, as shown in Table 1-1, where it is shown that the process studied in this work offers energy consumptions considerably lower than other available options (Table 7-1). Because of the lack of complete polarization curves for the other processes, no further insight into the variation of operational potential with current density can be given.

The operational costs for all available electrochemical processes for chlorine recycling are shown as a function of F_r, the percentage of HCl considered waste from the MDI and TDI industrial segments that could be recycled for electrolysis. It is observed that the Dupont-Denora process and the process studied in this work show the lowest operational costs.

Nevertheless, considering that oxygen evolution occurs at the anode when HCl concentration is too low or impurities present in hydrogen chloride or HCl oxidize at the anode, current efficiency is expected to be lower than 100%. Current efficiency is defined as the amount of current actually employed for the HClOR reaction. This parameter was investigated by employing different values of current efficiency for the process studied in this work and the Dupont-Denora process as a function of F_r (Figure 7-1b).
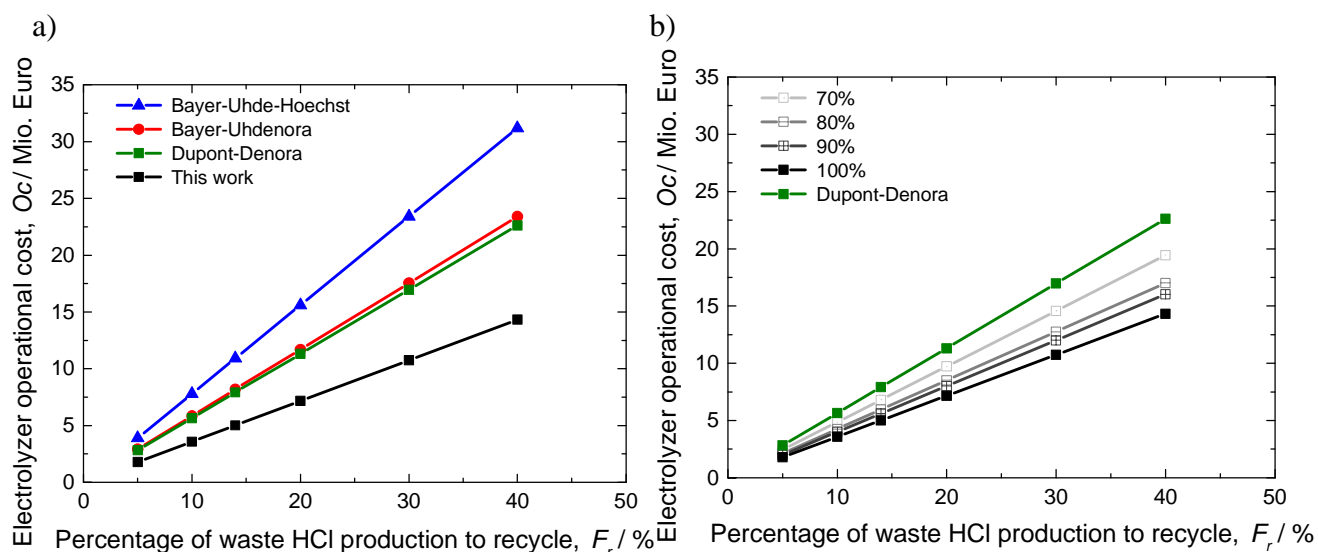
Figure 7-1 Yearly operational costs for the electrolysis of a percentage of total HCl production considered waste in the MDI and TDI industrial segments. a) All processes; b) this work at different current efficiencies.

It was found that our process provided energy savings against all other processes up to current efficiencies of 60%, where it overlapped with the curve of the Dupont-Denora process. Therefore, it is safe to say that the advantages offered by the process investigated in this work are robust regarding energy efficiency, which can be traced back to the low cell voltages measured.

8 Conclusions

In this work a novel chlorine recycling process based on the Deacon stoichiometry and using an oxygen-depolarized cathode was studied. In order to gain better understanding of the HClOR and ORR kinetics, these two reactions were studied under half-cell conditions on technical MEAs. For the HClOR, the effects of different catalysts, temperatures, and concentrations were studied. For Pt/C supported catalysts, the Nafion content was investigated in the range of 25-60°C between 13-70 wt.%. It was found out that the HCl oxidation at industrially relevant current densities is viable on both platinum and pure carbon electrodes, whereas the latter one operates at considerably higher overpotentials. Analysis of the reaction order and Tafel slopes showed that the most viable mechanism to describe the gaseous HCl oxidation was a Heyrovsky-Tafel mechanism under Temkin conditions, which is in accordance to the known behavior of chlorine evolution on platinum.

It was found out that to optimize the MEAs both the Nafion content as well as the Nafion loading have to be considered. For the HCl oxidation an optimum of *ca.* 60 wt.% Nafion was obtained. This value is considerably higher than values reported for other gas phase reactions (*i.e.* ORR). It was hypothesized that the stronger absorption of HCl compared to oxygen absorption in Nafion, can result higher mass transfer rates to the active sites, thus allowing for higher optimal Nafion loadings. For the ORR optimal values below 38 wt.% were found in accordance to results in literature.

An agglomerate model was developed for the HClOR in which the diffusion and conductivity properties of Nafion were correlated to experimental data available in literature. This was required because according to the agglomerate model, reactants must absorb and diffuse through the polymer electrolyte before reaching the active sites. This model allows the use of more structural parameters than other macroscale models (thin film and porous models), which result in a better description of current density at different conditions and MEA compositions. A membrane model was developed to describe species transport through the membrane (diffusion and electroosmotic drag) and conductivity of Nafion in the presence of HCl. This allowed the calculation of potential losses and concentration profiles through the membrane.

The models for the cathode, anode, and membrane were combined into an isothermal, 1-dimensional model for the complete reactor by adapting boundary conditions. All simulations were performed using kinetic and structural parameters estimated from measurements in the cyclone flow cell or literature correlations (especially transport and conductivity properties). Experimental data from the complete reactor, obtained by our partners in the Technical University Clausthal, showed that the OCP lies around 600 mV away from the predicted reversible cell potential values. This difference could be partially explained considering the intrinsic losses observed for the ORR (as confirmed in fuel cell literature) and the consideration of the Donnan potential. This potential is presumed to play an important role in the process analyzed due to the very different pH values at

the anode and cathode. Polarization curves showed activation, ohmic, and limiting current density regions. The ohmic region was characterized by a very low slope, which was traced back to water condensation in the cathode. Water was transported from the cathode to the anode through the membrane due to the high concentration gradient between them, overwhelming the osmotic drag from the anode to the cathode. This water flux improved the membrane conductivity by increasing the water content in Nafion as well as by diluting HCl, thus allowing for operation between 200-400 mA cm^{-2} with virtually no cell potential variation.

The reactor showed stable operation up to current densities of 400 mA cm^{-2}, after which the potential dramatically increased. The developed model showed good cell potential prediction capabilities only up to 400 mA cm^{-2}. It is hypothesized that the effects taking place above this current density are presumably caused from temperature changes in the MEAs and/or membrane, and therefore are out of the capabilities of the presented model. A global optimization for the electrode structure of the MEAs in the complete reactor was carried out. It was found that Nafion contents between 60 and 70 wt.% were optimal for the anode while for the cathode MEAs with 13% Nafion were found to yield the best performance.

The specific energy consumption per ton of chlorine for this investigated process is around 50% lower than that of the commercial standard process, making it a viable and attractive option to recycle hydrogen chloride.

9 Outlook

The process investigated in this work showed great potential as a new technology for chlorine recycling at mild conditions and with lower energy consumption than state-of-the-art industrial processes. It was the first time that cell potentials under 1 V were reported for platinum catalysts for the chlorine evolution reaction.

Simulation results with the 1-dimensional model developed in this work have shown that due to the isothermal nature of the model, the exothermal processes in the reactor could not be properly described. Energy balances have to be formulated and solved simultaneously with the mass balances to describe the temperature profile in the reactor at current densities above 400 mA cm^{-2}. The water balance and management was found to be of crucial importance in this system. The water uptake and ionic conductivity of Nafion are strong functions of temperature, and the coupling of these two phenomena must be experimentally determined at temperatures between 25 and 80°C in order to corroborate the model results.

One of the main drawbacks to analyze the HClOR is that physical data on the HCl-Nafion and hydrogen chloride-Nafion system are scarcely reported in literature. Data such as the ionic conductivity of Nafion in the presence of HCl, diffusion coefficient of HCl in Nafion, HCl uptake of Nafion, etc., have major importance for the validity of predicions made by the model. Therefore, measurements should be carried out in order to validate physical data employed in this work. Electrochemical impedance spectroscopy experiments in order to obtain the effective ionic conductivity as a function of HCl concentration could be carried out. The HCl uptake of Nafion could also be gravimetrically determined under controlled conditions. The diffusion coefficient of HCl through Nafion at different water contents should be experimentally determined, as not enough literature information about the topic is available. This could be done in a setup similar to the cyclone cell, where the concentrations of species in both compartments can be carefully regulated and a well defined membrane area can be used. With this, the permeation of HCl from one compartment to the other could be measured by titration.

A further insight into the material selection for the cell components should be done, from which possibly better membrane materials (thinner and not suceptible to aqueous HCl or with better water uptake capabilities) could be found. The catalyst selection should also be carefully revised, as several materials are active for the HClOR and could provide cheaper options compared to platinum. The deactivation of platinum for long term operation as well as constant shut-offs should be investigated in order to come closer to a reliable technical application.

10 Appendix

10.1 Thermodynamic properties

10.1.1 State properties

Due to the fact that the enthalpy, eq. (10-1), and the entropy, eq. (10-2), are both functions of temperature, the standard Nernst potential can be calculated at any temperature with help of the Shomate equations [146]. The parameters for these equations are presented in Table 10-1.

$$H(T) = H_f + AT + \frac{B}{2}T^2 + \frac{C}{3}T^3 + \frac{D}{4}T^4 - \frac{E}{T} + F - G \qquad (10\text{-}1)$$

$$S(T) = A\,ln(T) + \frac{C}{2}T^2 + \frac{D}{3}T^3 - \frac{E}{2T^2} + G \qquad (10\text{-}2)$$

Table 10-1 Thermodynamic parameters for the Shiomate equations [146].

Parameter	$HCl_{(g)}$	Cl_2	$H_2O_{(l)}$	$H_2O_{(g)}$	O_2	N_2
A	32.124	33.051	-203.606	30.092	31.322	28.986
B	-13.458	12.229	1523.290	6.833	-20.235	1.854
C	19.869	-12.065	-3196.413	6.793	57.866	-9.647
D	-6.854	4.385	2474.455	-2.534	-36.506	16.635
E	-0.050	-0.159	3.855	0.082	-0.007	0.000
F	-101.621	-10.835	-256.548	-250.881	-8.903	-8.672
G	228.687	259.029	-488.716	223.397	246.795	226.417

With help of these equations, the Gibb's energy was calculated and with help of eq. (2-13) the reversible thermoneutral and cell potentials could be obtained. Knowing the change in Gibbs energy allowed calculating the temperature dependence of the reversible electrode potentials, eqs. (2-17) and (2-18).

For the case of liquid HCl there is no Shomate equation. Therefore, the heat capacity of 1M HCl was taken from Atkins and Paula [147] as a value of -136.4 J mol⁻¹. The specific heat capacity of 1M HCl was taken as 3.966 J g⁻¹ K⁻¹ and considered constant in the temperature range from 25-80°C.

$$H_{HCl} = \Delta H_f + Cp_{HCl}(T - 298.15) \qquad (10\text{-}3)$$

where the standard enthalpy of formation ΔH_f is -167.2 kJ mol⁻¹. The entropy of HCl was calculated in a similar fashion employing a value of 56.5 J mol⁻¹ K⁻¹ for the entropy of formation ΔS_f.

$$S_{HCl} = \Delta S_f + C_{p,HCl}\,ln\left(\frac{T}{298.15}\right) \qquad (10\text{-}4)$$

10.1.2 Critical properties

The critical properties are needed for the calculation of the diffusion coefficients and viscosity of the different species and mixtures analyzed. These data were obtained from Perry [108] and Chen *et al* [148]. This data is presented in Table 10-2.

Table 10-2 Critical properties

Property	Symbol	Units	HCl	Cl_2	O_2	N_2	H_2O
Critical pressure	P_c	atm	82.6	77.0	50.4	34.0	220.6
Critical temperature	T_c	K	324.6	417.2	154.6	126.2	647.0
Critical volume	V_c	cm^3 g^{-1}	89.5	124	73.4	89.5	56.0
Lennard-Jones 2-2 Pot.	ϵ/k	K	360.0	357.0	113.0	91.5	356

10.2 Vapor pressure and liquid-vapor equilibrium correlations

10.2.1 Vapor pressure of water

For the calculation of the vapor pressure of water, the following modification of the Goff-Gratch equation was employed [149].

$$p^o_{H_2O} = A\,T^5 + B\,T^4 + C\,T^3 + D\,T^2 + E\,T + F \tag{10-5}$$

This equation provides better accuracy than the usual Antoine equation at high temperatures [150].

Table 10-3 Coefficients for eq. (10-5)

A	B	C	D	E	F
$2.08232 \cdot 10^{-11}$	$-2.48024 \cdot 10^{-8}$	$1.17673 \cdot 10^{-5}$	$-2.7667 \cdot 10^{-3}$	$-2.7667 \cdot 10^{-3}$	$-1.44700 \cdot 10^{1}$

10.3 Fugacity and activity models

10.3.1 Activity of gases

To calculate the activity of gases, (2-15), the fugacity of the gas, eq. (2-16), should be known. In order to implement the real behavior of gases in the modeled temperature (25-80°C) and pressure (1-2 bar) ranges, the compressibility factor z_g approach was employed. z_g is calculated according to the Stryjek-Vera modification to the Peng-Robinson equation, which takes into account polarity of the molecules through the acentric factor ω_f [151].

$$z_g^3 - (1 - B)z_g^2 + (A - 2B - 3B^2)z_g - (AB - B^2 - B^3) = 0 \tag{10-6}$$

where the factors *A*, *B*, and *k* area defined as:

$$A = 0.457235 \frac{P_r}{T_r^2} \left[1 + k\left(1 - \sqrt{T_r}\right)\right]^2 \tag{10-7}$$

$$B = 0.077796 \frac{P_r}{T_r} \tag{10-8}$$

$$k = 0.37464 + 1.54226\omega_f - 0.26992\omega_f^2 \tag{10-9}$$

The subindex r stands for the reduced properties and ω_f for the acentric factor, which are presented in Table 10-4. The required critical properties can be obtained from Table 10-2.

Table 10-4 Peng-Robinson-Stryjek-Vera parameters

Symbol	Units	HCl	Cl_2	O_2	N_2	H_2O
k	-	0.5528	0.4858	0.408	0.4313	0.8732
ω_f	-	0.1200	0.0700	0.0200	0.0400	0.3400

10.3.2 Activity of HCl in water

Because HCl dissociates into protons and chloride ions in aqueous solutions, its mean activity coefficient is defined as the geometrical average of the proton and chloride ion activity [152]:

$$\gamma_{HCl}^{\pm} = \sqrt{\gamma_{H^+}\gamma_{Cl^-}} \tag{10-10}$$

Experimental data for the HCl-water system was reported by Cerquetti *et al.* [153], who measured the activity coefficients in the range from 25 to 90°C. A correlation for the mean molal HCl activity coefficient as a function of either temperature or molality was given. It was found that $\gamma_{HCl}^{\pm}$ is a strong function of temperature, especially at high concentrations and low temperatures, as shown in Figure 10-1a.

Symbol	Value
A	$-4.61 \cdot 10^{-2}$
B	$7.46 \cdot 10^{-1}$
C	$-7.49 \cdot 10^{-1}$
D	$3.58 \cdot 10^{-4}$
E	$-3.71 \cdot 10^{-3}$
F	$3.79 \cdot 10^{-3}$
G	$-6.22 \cdot 10^{-7}$
H	$5.23 \cdot 10^{-6}$
I	$-6.70 \cdot 10^{-6}$
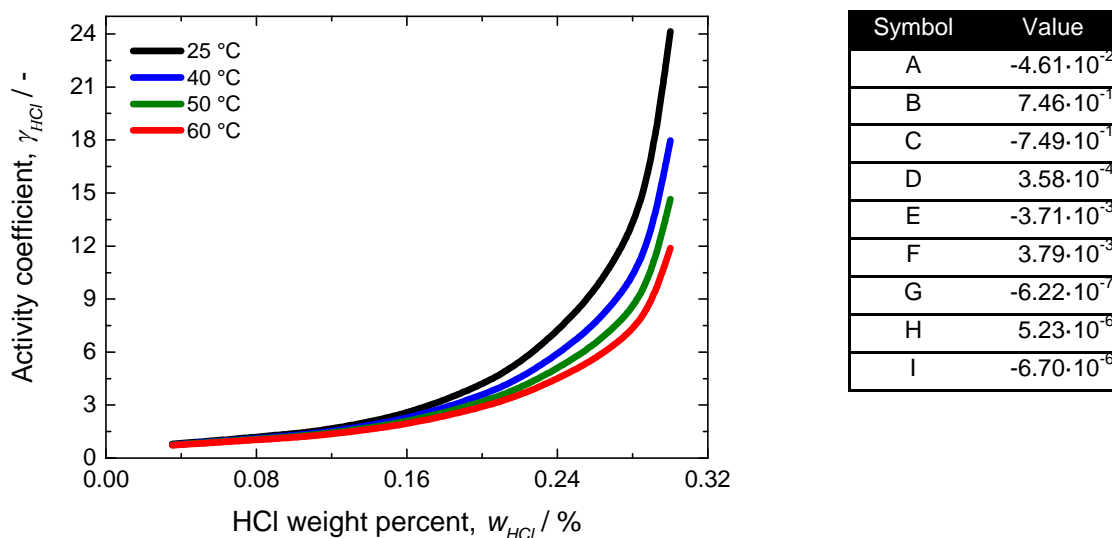
Figure 10-1 a) HCl activity as a function of HCl weight fraction at different temperatures, based on data from [153]; b) parameters for the activity coefficient of HCl eq. (10-11).

In order to use this data in the developed model, the experimental data of the logarithm of the mean HCl molal activity coefficient was correlated as a function of both, temperature and HCl molarity (M). This change was made because molarity is directly calculated by the model. It is important to note that the dependency of $\gamma_{HCl}^{\pm}$ on concentration diminishes at higher temperatures.

$$log(\gamma_{HCl}^{\pm}) = A\,M_{HCl}^2 + B\,M_{HCl} + C + \left(D\,M_{HCl}^2 + E\,M_{HCl} + F\right)T_s + (G\,M_{HCl}^2 + H\,M_{HCl} - I)T_s^2 \tag{10-11}$$

10.3.3 Activity model for HCl in Nafion

Considering that recast polymers resemble undercooled liquids [132], the model can be employed for mobile species within an immobile polymer backbone. The general formulation for activity is expressed in eq. (6-37). In this equation the molar volume of a single unit of Nafion V_m is taken as $5.6 \cdot 10^{-5}$ mol m^{-3} and the number of single chain units of Nafion between cross-links N$_m$ as 5 [132].

The Flory-Huggins activity model requires the interaction parameters χ between water, HCl, and Nafion. Parameters for water-Nafion interactions have been reported by several authors [127, 132], but not for HCl-Nafion. χ is zero for species similar to the membrane polymer, negative if both species attract each other and positive if both species repel each other.

The water-Nafion and HCl-Nafion parameters were estimated with swelling experiments as presented by Schultz [132]. Nafion 117 membranes were pretreated according to chapter 4.2 substituting the catalyst inks with pure water. This was done to obtain the same internal Nafion structure as in MEAs employed for the HClOR. The dry Nafion membranes dimensions V_{Naf}^{dry} were recorded. Then the membranes were immersed in pure water and HCl solutions of known concentrations (32 wt.%, 1M) and left to equilibrate for two days. The membranes uptake a definite amount of solution, whose volume, V_{Naf}^{sw}, was determined by measuring its swelled dimensions. Subtracting the ratio of the solution volume uptake to the dry Nafion membrane volume from unity, results in the volume fraction of the Nafion backbone when fully swollen.

This method considers that when the membrane is in equilibrium with the surrounding solution, the chemical potential inside and outside the membrane are identical. If the solution is a pure solvent, as in pure water, it holds that the activity of the solvent outside and inside the membrane is equal to one. On the other hand, HCl it is not available in pure form but as a water solution. Therefore, the activity of HCl was determined according to the equations presented in Appendix 10.3.2. The results from the swelling experiments are presented in Table 10-5.

Table 10-5 Swelling experiment results at 25°C.

Solution	V_{Naf}^{dry}	V_{Naf}^{sw}	ϵ_i^{Naf}	ϵ_{Naf}	$\chi_{i,m}$
Water	69.5	130.9	0.47	0.53	0.7686±0.0381
30% HCl	72.0	128.7	0.35	0.65	-1.1038±0.0436

The non-ideality parameter $\chi_{H_2O,m}$ was determined according to the following equation:

$$\chi_{H_2O,m} = \frac{1}{\epsilon_m^2}\left[-ln(\epsilon_{H_2O}) - \epsilon_m\left(1 - \frac{\bar{V}_{H_2O}}{\bar{V}_m}\right) - \frac{\bar{V}_{H_2O}\epsilon_m^{\frac{1}{3}}}{2N_mV_m}\right] \qquad (10\text{-}12)$$

From which a value of 0.7686 was obtained. Schultz [132] reported a value of 0.7177, showing good agreement with the calculated value. $\chi_{H_2O,m}$ exhibited a change of *ca.* 3% over the temperature range investigated in this work (25-60°C). The non-ideality parameter $\chi_{HCl,m}$ cannot be

determined directly as the one from water due to the dilution of HCl, leaving it as a function of HCl activity and the non-ideality parameter χ_{HCl,H_2O}.

$$\chi_{HCl,m} = \frac{1}{\epsilon_m^2}\left[ln(\gamma_{HCl}) - \epsilon_{H_2O}\left(1 - \frac{\bar{V}_{HCl}}{\bar{V}_{H_2O}}\right) - \chi_{HCl,H_2O}\epsilon_{H_2O}^2 - \epsilon_m\left(1 - \frac{\bar{V}_{HCl}}{\bar{V}_m}\right) - \frac{\bar{V}_{HCl}\epsilon_m^{\frac{1}{3}}}{2N_mV_m}\right] \qquad (10\text{-}13)$$

As presented in Appendix 10.3.2, the activity coefficient of HCl in water γ_{HCl} is a strong function of both temperature and HCl concentration, feature also shown by $\chi_{HCl,m}$ according to eq. (10-13). Therefore in simulations presented in this work, the non-ideality parameter $\chi_{HCl,m}$ was calculated as the average between the value at the anode side (high HCl concentrations, values between -1.0 and -0.1 depending on temperature) and the cathode side (negligible HCl concentration, value of 0.7 regardless of temperature). These results are in accordance to data presented by Balko *et al.* [17] in which an increasing HCl concentration reduced the solvent activity and the overall water content of the polymer electrolyte membrane.

$$\chi_{HCl,H_2O} = \frac{1}{\epsilon_{H_2O}^2}\left[ln(\gamma_{HCl}) - \epsilon_{H_2O}\left(1 - \frac{\bar{V}_{HCl}}{\bar{V}_{H_2O}}\right)\right] \qquad (10\text{-}14)$$

With these parameters, activities for HCl and water in the Nafion membrane were calculated.

10.3.4 Activity of protons in Nafion

As reported in literature [154, 155], the proton activity in Nafion equilibrated with water ranges from 0.8 up to 2.8.

10.4 Correlations to determine effective properties

Transport coefficients and conductivities must be corrected for the volume fraction of the phase in which the corresponding transport phenomena take place: the void or the solid phase, eq. (10-15):

$$t_i^{eff} = \frac{\epsilon_m \, t_i}{\tau_m^2} \qquad (10\text{-}15)$$

where τ stands for the tortuosity of media m and t the property of component i to correct.

10.4.1 CL

Different correlations for tortuosity have been proposed in the literature to account for effective properties in the CL. Shen and Chen [70] briefly reviewed the most common correlations, in which the most important are the ones from:

a) Bruggeman: Empirically developed for non-overlapping packed spheres. In porous media, its validity has been experimentally shown at porosities above 0.6. It doesn't consider contact between spheres.

$$\tau^2 = \frac{1}{\sqrt{\epsilon_m}} \qquad (10\text{-}16)$$

b) Maxwell: Developed for randomly ordered packed spheres and the calculation of diffusivity. The contact between spheres is considered and is valid for low and medium porosity values.

$$\tau^2 = \frac{3 - \epsilon_m}{2} \tag{10-17}$$

c) Beekmann: Developed through Monte-Carlo simulations of randomly packed and branch-connected media. Its validity is not bounded by any porosity value.

$$\tau^2 = \frac{\epsilon_m}{1 - \sqrt[3]{(1 - \epsilon_m)}} \tag{10-18}$$

The Bruggeman correlation is the most widely used correction in CL modeling because it corresponds to the physical description of the CL being composed by an arrangement of round agglomerates. Due to its simplicity it has been used even at low porosity values. The Beekman correlation takes into account the contact pathways between particles and not just its volume fraction, yielding lower values for the effective properties in accordance with experiments [45, 156]. The Maxwell correlation overestimates effective diffusion in comparison with the other two correlations in the entire porosity range. Due to its irregular nature and typical porosity values (0.1-0.4 [76, 80, 91, 96, 157-160]), none of the correlations fit CL experimental data completely. Therefore, due to its simplicity the Bruggeman correlation was employed in this work to correct diffusion coefficients.

10.4.2 GDL

Even though the Bruggeman correlation has been widely employed for the GDL [149], the GDL internal structure is hair-like, thus rendering its use as physically incorrect. In order to properly describe connected hair-like structures percolation theory was employed, which takes the form of:

$$\tau^2 = \left[\frac{\epsilon_{th}}{\epsilon_{GDL} - (1 - \epsilon_{th})} \right]^n \tag{10-19}$$

where ϵ_{th} is the threshold porosity of the media (taken as 0.89) and n is an empirically determined coefficient. This correlation gives lower effective property values as the Bruggeman correlation as the tortuosity in the GDL is greater than in the CL.

10.5 Diffusion coefficients

The following physical properties are used in all modeled domains and were corrected for the different media porosity by means of the corresponding empirical correlation, Bruggeman or percolation theory.

10.5.1 Binary diffusion coefficient of gases

The binary diffusion coefficient was calculated according to the Chapman-Enskog kinetic theory of gases [66, 97, 161, 162], which considers that molecules are spherical, there is no interaction between molecules except when they collide, molecules have no polarity, and collisions between molecules are elastic. This results in eq. (10-20) [66, 97, 161, 162].

$$D_{12} = \frac{1.86 \cdot 10^{-7} T^{3/2} \sqrt{\frac{MW_1 + MW_2}{MW_1 MW_2}}}{P \, \sigma_{12}^2 \, \Omega_D} \tag{10-20}$$

with P as the pressure, σ_{12} the collision diameter, MW_i the molecular weight, and Ω_D the collision integral. In order to describe the diffusion of polar molecules correctly, such as water and hydrochloric acid, a correction to the collision integral is used according to Othmer und Chen [148, 163], where k stands for the Boltzmann-constant and ε_{LJ} for the Stockmayer Potential [164], which includes the effect of the dipole moment [164].

$$\Omega_D = \begin{cases} 1.47 \left(\dfrac{k_b T}{\epsilon_{LJ}} \right)^{-0.59} & \dfrac{k_b T}{\epsilon_{LJ}} < 2.5 \\[4mm] 1.07 \left(\dfrac{k_b T}{\epsilon_{LJ}} \right)^{-0.17} & \dfrac{k_b T}{\epsilon_{LJ}} > 2.5 \end{cases} \tag{10-21}$$

10.5.2 Diffusion coefficient in and of a gas mixture

In order to calculate the diffusion coefficient of a species in a mixture of three or more components (*i.e.,* when using dilution with nitrogen in both electrodes), the binary interactions between species must be averaged by its mole fractions according to [165]:

$$D_i = \frac{1 - x_i}{\sum_{\substack{j=1 \\ j \neq i}}^{n} \dfrac{x_j}{D_{ij}}} \tag{10-22}$$

The binary diffusion coefficients as a function of temperature are given in Figure 10-2.
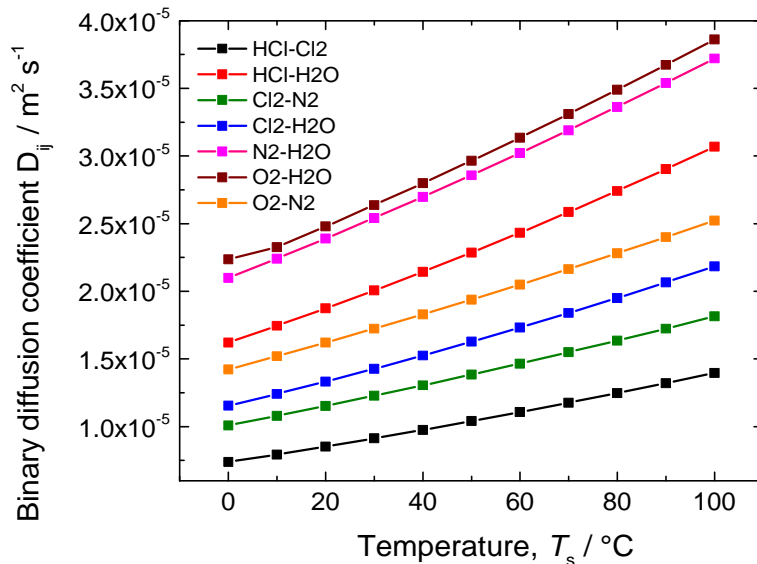
Figure 10-2 Binary diffusion coefficients as a function of temperature.

10.5.3 Diffusion coefficient in Nafion

There is very little information about the diffusion coefficient of HCl through Nafion, being the experimental data from Schwitzgebel and Endres [166] the most reliable. Their data was adjusted to the following modified Arrhenius-like correlation in the range of 25-70°C:

$$D_{HCl}^{Naf} = 4.54 \cdot 10^{-9} \, exp\left(-\frac{25000}{RT}\right) + 3.00\lambda \qquad (10\text{-}23)$$

For the diffusion coefficient of water in Nafion, correlations from different authors were compared [68, 112, 134] to obtain the activation energy and preexpoential factor. For the water content dependence the correlation presented by Nguyen was taken as a basis [167]:

$$D_{H_2O}^{Naf} = (0.033\lambda + 0.575) \cdot 1.516 \cdot 10^{-7} exp\left(-\frac{16250}{RT}\right) \qquad (10\text{-}24)$$

It was assumed that the diffusion coefficient of chlorine in Nafion was equal to that of oxygen, as both molecules are non-polar and have similar molecule sizes (*ca.* 4.4 and 3.0 Å, respectively [168]).

According to the Onsager relationship, in order to simulate the simultaneous transport of protons, water, and HCl in the membrane, three different binary diffusion coefficients are required. For the diffusion of protons in HCl, data from Bertagnolli *et al.* [169] at 25°C was correlated. This correlation was extrapolated to temperatures above 40°C by means of the Einstein-Stokes equation, based on the relation of viscosity with temperature. The reference temperature is taken as 25°C.

$$D_{HCl,H^+} = 2.426 \cdot 10^{-9} \, exp(-6.343 \cdot 10^{-5} c_{HCl}^m)\left(\frac{T}{T_o}\frac{\mu_o}{\mu}\right) \qquad (10\text{-}25)$$

Harpst *et al.* [170] investigated the diffusion coefficient of HCl in water and found out that it follows a logarithmic decay at molarities higher than 0.05.

$$D_{HCl,H_2O} = [4.205 \cdot 10^{-14} \, ln(c_{HCl}^m) + 2.985 \cdot 10^{-9}]\left(\frac{T}{T_o}\frac{\mu_o}{\mu}\right) \qquad (10\text{-}26)$$

For the diffusion coefficient of protons in water, Chen *et al* [171] reported their transport proceeds by means of Grotthus and *en masse* diffusion. The correlation they presented is temperature dependent:

$$
\begin{aligned}
D_{H_2O/H^+} = {}& 2.397 \cdot 10^{-8} \, ln(T) - 1.318 \cdot 10^{-7} - [2.397 \cdot 10^{-8} ln(T) - 1.318 \cdot 10^{-7} \\
& - (2.117 \cdot 10^{-14}T^3 - 2.017 \cdot 10^{-11}T^2 + 6.409 \cdot 10^{-9}T - 6.761 \cdot 10^{-7})] \cdot \\
& exp\left(-\frac{1}{6.22T^{-4.79}}\right)
\end{aligned}
\qquad (10\text{-}27)
$$

10.6 Viscosity

10.6.1 Viscosity of single gaseous species

The dynamic viscosity of non-polar gaseous species is calculated according to the Chapman-Enskog theory, valid up to pressures below 2.5 times the reduced pressure [164, 172, 173].

$$\mu_i = \begin{cases} \dfrac{34 \cdot 10^{-7} \cdot T_r^{0.94} \cdot MW_i^{\frac{1}{2}} \cdot P_c^{\frac{2}{3}}}{T_c^{\frac{1}{6}}} & T_r \leq 1.5 \\[2em] \dfrac{17.78 \cdot 10^{-7}(4.58 \cdot T_r - 1.67)^{\frac{5}{8}} \cdot MW_i^{\frac{1}{2}} \cdot P_c^{\frac{2}{3}} \cdot}{T_c^{\frac{1}{6}}} & T_r > 1.5 \end{cases} \tag{10-28}$$

For polar gases a correction proposed by Hyun, based on the theorem of corresponding states [172], is employed. Eq. (10-29) is valid for molecules with hydrogen bridge bonds up to 2 times the reduced pressure, where T_r is the reduced temperature, Z_c the critical compression factor, MW_i the molecular weight, P_C the critical pressure, and T_c the critical temperature.

$$\mu_i = \frac{10^{-7}(7.55 T_r - 0.55) Z_c^{-\frac{5}{4}} MW_i^{\frac{1}{2}} P_c^{\frac{2}{3}}}{T_c^{\frac{1}{6}}} \tag{10-29}$$

10.6.2 Viscosity of a gaseous mixture

The mixture viscosity is necessary to determine the HDL thickness, given the fact that represents the cohesion and flow capability between molecules [174]:

$$\eta_{mix} = \sum_{i=1}^{n} \frac{\eta_i}{1 + \frac{1}{x_i} \cdot \sum_{\substack{j=1 \\ j \neq i}}^{n} \frac{x_j \left[1 + \left(\frac{\eta_i}{\eta_j}\right)^{\frac{1}{2}} \left(\frac{MW_j}{MW_i}\right)^{\frac{1}{4}}\right]^2}{2\sqrt{2}\left(1 + \frac{MW_i}{MW_j}\right)^{\frac{1}{2}}}} \tag{10-30}$$

A particularity and advantage of this equation is that no density or diffusion coefficient is needed, leaving viscosity as a function only of temperature and pressure.

10.6.3 Viscosity of aqueous solutions

In order to employ the Einstein-Stokes relation to estimate diffusion coefficients of aqueous HCl at different temperatures, the viscosity of HCl is needed. Experimental data from Solvay GmbH [175] was correlated for a concentration range from 5 to 38 wt.% and temperatures from 25 to 80°C.

$$\mu_{HCl} = (AT_s^3 + BT_s^2 + CT_s + D)w_{HCl}^2 + (ET_s^3 + FT_s^2 + GT_s + H)w_{HCl} + (IT_s^3 + JT_s^2 + KT_s + L) \tag{10-31}$$

The viscosity of water is given by the following equation [168]:

$$\mu_{H_2O} = 1.68 \cdot 10^{-5} \rho_{H_2O} T_s^{-0.88} \tag{10-32}$$

Table 10-6 Parameters for eq. (10-31).

Coeff.	Value	Coeff.	Value	Coeff.	Value
A	$-2.33 \cdot 10^{-8}$	F	$-1.91 \cdot 10^{-6}$	K	$-7.75 \cdot 10^{-5}$
B	$5.64 \cdot 10^{-6}$	G	$1.00 \cdot 10^{-4}$	L	$2.51 \cdot 10^{-3}$
C	$-3.69 \cdot 10^{-4}$	H	$-7.13 \cdot 10^{-4}$		
D	$1.18 \cdot 10^{-2}$	I	$-4.04 \cdot 10^{-9}$		
E	$8.69 \cdot 10^{-9}$	J	$9.61 \cdot 10^{-7}$		

10.7 Nafion water content

Nafion has the capacity to uptake water molecules due to its physical (porosity) and chemical nature (sulfonic groups). Water uptake λ_{Naf} has been described as a function of water concentration and its physical state in literature [18, 111, 112, 134, 176]. Alberti and Zawodzinski measured Nafion isotherms up to 80°C and assumed their validity up to glass-transition temperatures, *ca.* 130°C [18, 176]. Hinatsu showed different λ_{Naf} were achieved at different temperatures [111], so based on his experimental data eq. (10-33) was correlated.

$$\lambda_{naf}^{T} = \begin{cases} -1.32 \cdot 10^{-5}T^3 + 1.36 \cdot 10^{-2}T^2 - 4.52T + 500.30 \quad Liquid \\ \\ 3.64 \cdot 10^{-4}T^2 - 1.67 \cdot 10^{-1}T + 23.79 \qquad\qquad Gaseous \end{cases} \qquad (10\text{-}33)$$

This correlation is valid from 25 to 80°C and a water activity of unity. As it can be observed, water uptake is twice as much for Nafion membranes equilibrated with liquid water as for membranes equilibrated with vapor. However, λ_{Naf} is also a function of water activity, which is unity for liquid water and variable for vapor ($y_{H_2O}p/p_{H_2O}^o$). λ_{Naf} shows a small increase at low activities and a drastic increase at activities above 0.6. This can be explained by the hydrophobic backbone of Nafion, which repulses water, and the hydrophilic sulfonic groups, which are easily solvated and therefore attract water [18]. At low water activities not much water is absorbed by Nafion due to the repulsion due to the hydrophobic backbone. Nevertheless, when the water activity is high enough to overcome this repulsion, water uptake increases drastically, as represented in eq. (10-34):

$$\lambda_{Naf}^{a_{H_2O}} = 36.01a_{H_2O}{}^3 - 39.85a_{H_2O}{}^2 + 17.81a_{H_2O} + 0.04 \qquad (10\text{-}34)$$

Eqs. (10-33) and (10-34) were combined yielding:

$$\lambda_{Naf}^{a_{H_2O}} = \frac{\left(\lambda_{Naf}^{T} \cdot \lambda_{Naf}^{a_{H_2O}}\right)}{7} \qquad (10\text{-}35)$$

10.8 Density

10.8.1 GDL and catalysts

The density of the carbon cloth employed as GDL ranges between 480 and 520 kg m^{-3} [62, 177]. Platinum has a density of 21450 kg m^{-3} [108], while the density of Vulcan XC72R lies between 1.75 and 2.10 kg m^{-3} [66, 97, 108-110]. The density of these three components shows a very little dependence of temperature, less than 1% for temperature changes of up to 50°C.

10.8.2 Nafion

Nafion density is dependent on the water uptake λ, as water is uptaken by Nafion's structure. Another factor influencing Nafion density is the membrane preparation: if membranes are protonated with acids or with salts [45, 112, 178]. The choice of drying temperature also influences density, as higher temperatures result in higher Nafion densities [68, 179]. Experimental data of

Nafion density was correlated as a function of water uptake for values of λ from 0-22 and temperatures up to 80°C.

$$\rho_{Naf} = -3.96T_s + 2144.7 - 19.58\lambda \qquad (10\text{-}36)$$

10.8.3 Hydrochloric acid

The density of liquid HCl is required to calculate mass and mol fractions from molarity values. According to experimental data from Perry [168] and Solvay GmbH [175], eq. (10-37) was correlated for HCl weight fractions with respect to liquid water w_{HCl} from 0 to 38% and temperatures from 25 to 80°C.

$$\rho_{HCl} = (5.357 \cdot 10^{-3}T_s^2 - 9.928 \cdot 10^{-1}T_s + 516)\, w_{HCl} + \\ (-2.70 \cdot 10^{-3}T_s^2 - 1.35 \cdot 10^{-1}T_s + 1 \cdot 10^{-3}) \qquad (10\text{-}37)$$

10.8.4 Water

The density of water in this work is based on the work of McCutcheon *et al.* [180]. Its value is required for the calculation of the water content in Nafion:

$$\rho_{H_2O} = \left(1 - \frac{(T_s - 4)^2}{119000 + 1365\, T_s - 4\, T_s^2}\right) \qquad (10\text{-}38)$$

10.9 Electric conductivity

10.9.1 GDL

The GDL electrical conductivity depends on material properties, such as the carbon type, its internal structure, polymer binders, thermal handling, etc. Toray paper and carbon cloth are among the most used materials with conductivities in the range from 100 to 300 S m^{-1} [45, 62, 124, 177]. Analogous to the diffusion coefficient, conductivity was corrected for porosity. Percolation theory was employed due to the hair-like nature of the GDL [78, 83] with a porosity threshold of 0.89.

$$\sigma_e^{GDL} = \sigma_{GDL}^o (1 - \epsilon_{GDL}) \left(\frac{(1 - \epsilon_{GDL}) - (1 - \epsilon_{th})}{\epsilon_{th}}\right)^{0.785} \qquad (10\text{-}39)$$

I.e., with porosity of 0.75 and bulk conductivity of 3445 S m^{-1} [62], a value of 200 S m^{-1} is obtained.

10.9.2 CL

In the CL, only the Pt/C network is electrically conductive. Platinum has an electrical conductivity expressed by eq. (10-40) as a function of temperature [108, 124, 181]:

$$\sigma_e^{pt} = 1.75 \cdot 10^7 - 2.69 \cdot 10^4 T \qquad (10\text{-}40)$$

which yields values of 9.6 MS m^{-1}. For the conductivity of Vulcan XC72R, values between 200 and 400 S m^{-1} have been reported [182]. The electrical CL conductivity can be determined only experimentally due to the complexity of its structure, such as contact points between Pt-C particles, Nafion distribution, etc. In literature, very different values have been assumed, ranging from 200 up

to 21400 S m^{-1} [66, 69, 97, 99, 183, 184]. The base CL electrical conductivity is calculated as a weighted average of the Vulcan X72R and platinum conductivities according to eq. (10-41):

$$\sigma_e^{0,CL} = \left[rw_{Pt/C}\,\sigma_e^{Pt} + \left(1 - rw_{Pt/C}\right)\sigma_e^{C}\right]\left(\frac{\rho_C}{\rho_{Pt}}\right) \tag{10-41}$$

This equation results in values between 5300-5800 S m^{-1}, which are then corrected with Bruggeman correlation to yield the effective CL electrical conductivity according to eq. (10-42):

$$\sigma_e^{CL} = \left[1 - \epsilon_{CL} - \epsilon_{Naf}\right]^{\frac{3}{2}}\sigma_e^{0,CL} \tag{10-42}$$

10.10 Ionic conductivity

10.10.1 *Membrane*

Ionic conductivity of Nafion is a function of temperature and water content. Springer *et al.* [66, 184] described it by means of a modified Arrhenius equation:

$$\sigma_p^0 = (0.51\lambda - 0.32)\,exp\left[1268\left(\frac{1}{303} - \frac{1}{T}\right)\right] \tag{10-43}$$

This equation considers a maximum λ value of 22, which as shown in 10.7 is not the case for low temperatures and low humidification. Experimental data from Springer, Tsampas, and Zawodzinski [18, 184, 185] was employed to correlate an Arrhenius model, yielding:

$$\sigma_p^0 = (33.75\lambda - 21.41)\,exp\left(-\frac{10512}{RT}\right) \tag{10-44}$$

In the presence of HCl, Nafion conductivity shows lower values than in pure water. Because of the complex dissociation behavior of HCl in water, Nafion conductivity in HCl is a function of temperature, water content, and HCl concentration. There is currently no correlation that properly describes this behavior and a polynomial fit of experimental data from McBreen and Yeo [25] was correlated and employed in this work:

25-60°C
$$\begin{aligned}\sigma_{naf}^{HCl} = &(A\,T^2 + B\,T + C)c_{HCl}^6 + (D\,T^2 + E\,T + F)c_{HCl}^5 +\\ &(G\,T^2 + H\,T + I)c_{HCl}^4 + (J\,T^2 + K\,T + L)c_{HCl}^3 +\\ &(M\,T^2 + N\,T + O)c_{HCl}^2 + (P\,T^2 + Q\,T + R)c_{HCl} +\\ &(S\,T^2 + U\,T + V)\end{aligned}$$

60-85°C
$$\begin{aligned}\sigma_{naf}^{HCl} = &(AT^3 + BT^2 + CT + D)c_{HCl}^6 + (ET^3 + FT^2 + GT + H)c_{HCl}^5 +\\ &(IT^3 + J\,T^2 + KT + L)c_{HCl}^4 + (MT^3 + NT^2 + OT + P)c_{HCl}^3 +\\ &(QT^3 + RT^2 + ST + T)c_{HCl}^2 + (UT^3 + VT^2 + WT + X)c_{HCl} +\\ &(Y\,T^3 + Z\,T^2 + A'T + B')\end{aligned}$$
$$\tag{10-45}$$

Table 10-7 Coefficients for the Nafion conductivity equilibrated with HCl.

a) 25-60°C				b) 60-85°C		
A	$1.3497\cdot10^{-10}$	O	$-6.5773\cdot10^{-1}$	A	$-2.7975\cdot10^{-11}$	O	$4.9876\cdot10^{-2}$
B	$-2.9284\cdot10^{-9}$	P	$1.4446\cdot10^{-3}$	B	$5.5928\cdot10^{-9}$	P	$-1.1245\cdot10^{0}$
C	$2.2519\cdot10^{-8}$	Q	$-2.1911\cdot10^{-1}$	C	$-3.6532\cdot10^{-7}$	Q	$-3.8866\cdot10^{-5}$
D	$-1.5462\cdot10^{-8}$	R	$6.7646\cdot10^{0}$	D	$7.9945\cdot10^{-6}$	R	$8.2322\cdot10^{-3}$
E	$1.9257\cdot10^{-7}$	S	$-6.9121\cdot10^{-3}$	E	$3.4096\cdot10^{-9}$	S	$-5.7095\cdot10^{-1}$
F	$1.9862\cdot10^{-6}$	U	$8.9318\cdot10^{-1}$	F	$-6.8675\cdot10^{-7}$	T	$1.3073\cdot10^{1}$

G	$6.1670 \cdot 10^{-7}$	V	$-1.9761 \cdot 10^{1}$	G	$4.5212 \cdot 10^{-5}$	U	$1.9631 \cdot 10^{-4}$
H	$4.7030 \cdot 10^{-6}$			H	$-9.9695 \cdot 10^{-4}$	V	$-4.3006 \cdot 10^{-2}$
I	$-4.8449 \cdot 10^{-4}$			I	$-1.5947 \cdot 10^{-7}$	W	$3.0833 \cdot 10^{0}$
J	$-8.6722 \cdot 10^{-6}$			J	$3.2462 \cdot 10^{-5}$	X	$-7.1769 \cdot 10^{1}$
K	$-6.7256 \cdot 10^{-4}$			K	$-2.1608 \cdot 10^{-3}$	Y	$-4.4200 \cdot 10^{-4}$
L	$2.7282 \cdot 10^{-2}$			L	$4.8115 \cdot 10^{-2}$	Z	$9.8592 \cdot 10^{-2}$
M	$-2.7310 \cdot 10^{-5}$			M	$3.5653 \cdot 10^{-6}$	A'	$-7.0744 \cdot 10^{0}$
N	$1.9460 \cdot 10^{-2}$			N	$-7.3716 \cdot 10^{-4}$	B'	$1.7011 \cdot 10^{2}$

a)   b)
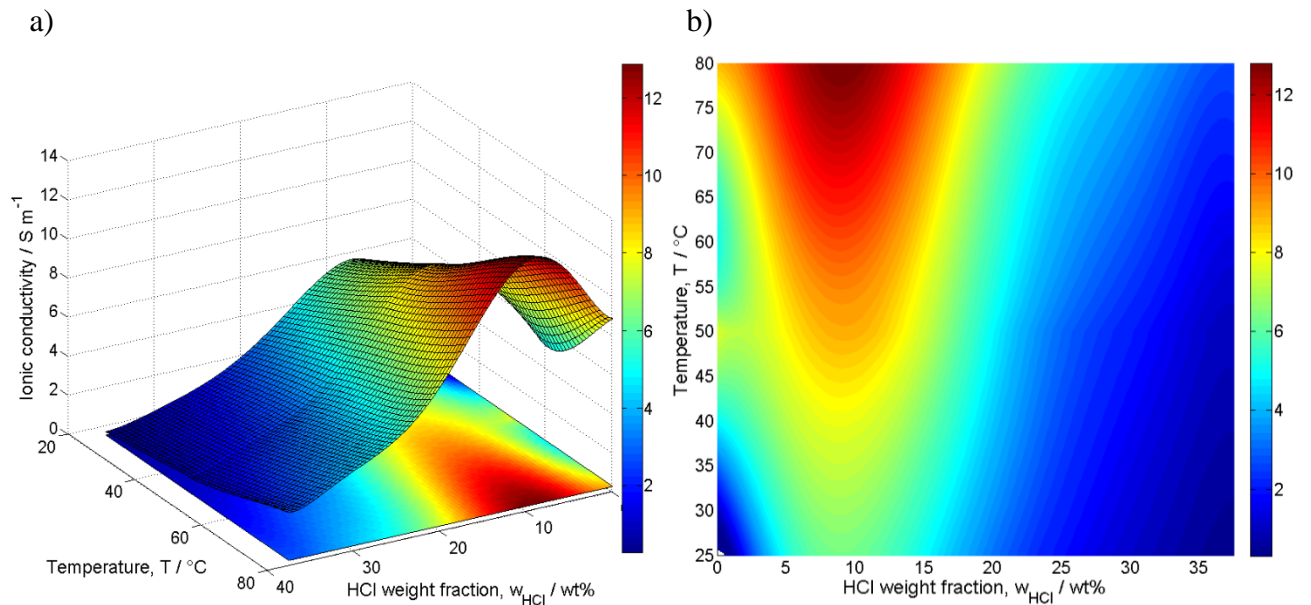
Figure 10-3 Nafion conductivity as a function of temperature and HCl weight fraction: a) 3D; b) 2D.

10.10.2   CL ionic conductivity

The ionic conductivity in the CL was taken as the Nafion conductivity in the presence of HCl for the anode and of Nafion in the presence of only water for the cathode. These conductivities were corrected for the fraction of Nafion in the CL with the Bruggeman correlation:

$$\sigma_p^{CL} = \left[1 - \epsilon_{CL} - \epsilon_{Pt/C} \right]^{\frac{3}{2}} \sigma_p^{0,CL} \qquad (10\text{-}46)$$

10.11 Gas absorption in Nafion

10.11.1   Oxygen

Absorption of oxygen in Nafion can be described by Henry's Law [66]:

$$p_i^o = H_i \, c_i^{CL/naf} \qquad (10\text{-}47)$$

where p_i^o stands for the partial pressure of oxygen in the CL. The temperature dependence of the Henry coefficient H_i follows an Arrhenius dependence:

$$H_i = H_i^o \, exp \left(-\frac{E_a}{RT} \right) \qquad (10\text{-}48)$$

Parthasarathy and Morris [52, 103, 112] correlated values of $2.23 \cdot 10^5$ J mol^{-1} and an activation energy of 5720 J mol^{-1} from experimental data. This equation is only valid up to pressures of 5 bar [108, 186]. The value of H_i rises with increasing temperature, resulting in a decrease of reactant absorption in Nafion.

10.11.2   Chlorine

In order to calculate the chlorine concentration in Nafion, it was assumed that Nafion has the same absorption properties as water. Chlorine can absorb and hydrolyze in water. In the case of low pH, *i.e.* due to HCl absorption in the anode, chlorine hydrolysis doesn't take place allowing the direct calculation of the chlorine concentration in water Nafion from the chlorine partial pressure in the gas phase. A correlation was obtained from experimental data presented by Adams and Edmonds [187]. Knowing the water uptake in Nafion, one can compute the total chlorine concentration in Nafion as a function of temperature in °C (T_s) according to the following equation:

$$c_{Cl_2}^{Naf|CL} = \frac{(6.38 \cdot 10^{-4}T_s^2 - 9.90 \cdot 10^{-2}T_s + 4.73)p_{Cl_2}}{zRT} \tag{10-49}$$

Absorbed chlorine as a function of the gas phase molar fraction is presented in Figure 10-4.
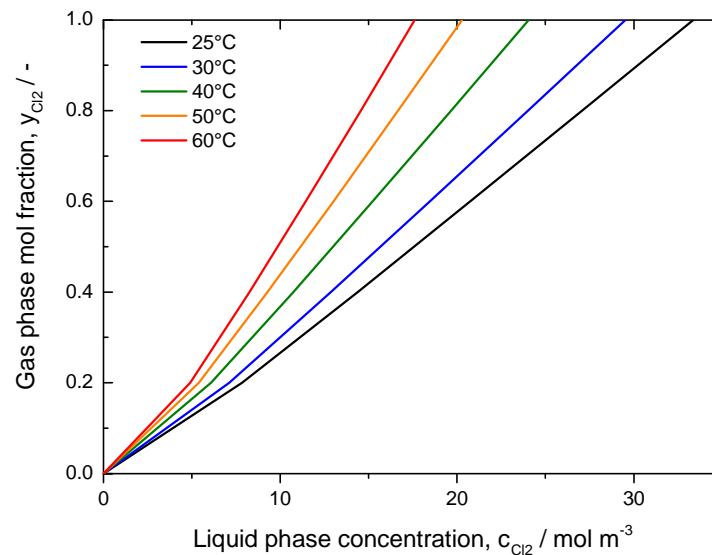
Figure 10-4 Chlorine-Nafion equilibrium diagram as a function of temperature.

10.11.3   Hydrogen chloride

For the absorption of HCl in water, experimental data from the HCl-Water system equilibrium was taken into consideration [142, 188, 189]. HCl absorption shows a non-linear equilibrium between the liquid and gas molar fractions x_{HCl} and y_{HCl}, as shown in Figure 10-5. Maximal HCl absorption takes place at 25°C with a value of 22% and diminishes with temperature. y_{HCl} is directly calculated from the gas composition, which is a function only of the temperature. The molar fraction of hydrogen chloride was fitted to the molar fraction of absorbed HCl in water yielding isotherms of the form:

$$y_{HCl} = \frac{-1.59 \cdot 10^{-4}T_s + 1.027}{1 + exp(-(0.4737T_s + 42.544)[x_{HCl} - (-8.525 \cdot 10^{-4}T_s + 0.1734)])} \tag{10-50}$$

By solving eq. (10-50) for x_{HCl}, the following expression is obtained for absorbed HCl in water.

$$x_{HCl} = -\frac{ln\left(\frac{-1.59E - 4T_s + 1.027}{y_{HCl}} - 1\right) - 8.525 \cdot 10^{-4}T_s + 0.1734}{0.4737T_s + 42.544} \tag{10-51}$$

Knowing the concentrations of chlorine and water in Nafion, the concentration of HCl at the boundary between the Nafion layer surrounding the agglomerates and the CL void fraction can be directly calculated by eq. (10-52).

$$c_{HCl}^{Naf|CL} = \frac{x_{HCl}(c_{Cl_2} + c_{H_2O})}{1 - x_{HCl}} \tag{10-52}$$

This concentration is the starting point for the agglomerate model calculations, as the activity coefficient and therefore chlorine activity require the concentration present in Nafion (see Appendix 10.3.2 and 10.3.3). Once activities are obtained, reaction kinetics can be calculated.
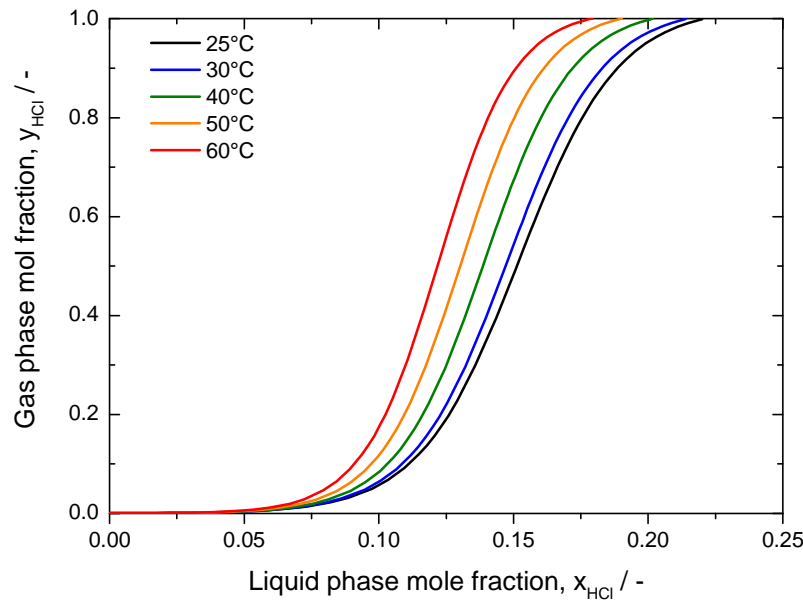
Figure 10-5 HCl-water equilibrium diagram as a function of temperature

10.12 Mass Biot number analysis

The Biot number analysis was done based on a gas mixture of 90% HCl and 10% chlorine and at 60°C. The mass Biot number is defined by eq. (5-12), which compares the mass transport resistance of the HDL against other layers. The HDL mass transport coefficient is obtained from the Sherwood number correlation in a cyclone flow cell [29], with validity for Re<1000 and Sc>1.

$$Sh = 0.0136Sc^{1/3}Re^{2/3} \tag{10-53}$$

The Schmidt number follows employing the diffusion coefficient in the gas mixture D_i, which in this case is equal to the binary diffusion coefficient of hydrogen chloride in chlorine and oxygen in water, respectively:

$$Sc = \frac{\mu}{\rho D_i} \tag{10-54}$$

Because of the cyclone gas flow inside the cell, the Reynolds number is defined as a function of the gas angular velocity ω and radius of the electrode r_e (0.8 cm):

$$Re = \frac{\omega r_e^2 \rho_g}{\mu} \tag{10-55}$$

where ω is given by the following relation:

$$\omega = 19.2 \, \dot{V} \tag{10-56}$$

and $\dot{V}$ represents volumetric flow rate in ml s^{-1}. With these definitions and a flow rate of 8.3 ml s^{-1}, Reynold numbers of 894 and 548 were obtained at 60°C for hydrogen chloride and oxygen respectively. For the Schmidt number, values of 1.06 and 0.58 were obtained. This shows that the correlation would be suitable for calculations at the anode and that at the cathode a certain error needs to be considered. The different values for the Schmidt number arise due to the high diffusion coefficient of oxygen in water compared to the one of hydrogen chloride in chlorine (1.08·10^{-5} vs. 3.25·10^{-5} m^2 s, respectively). Considering the definition of the Sherwood number:

$$Sh = \frac{k_m r_e}{D_i} \tag{10-57}$$

The mass transfer coefficient was calculated, yielding values of 1.76·10^{-3} and 2.81·10^{-3} m s^{-1} for hydrogen chloride and oxygen.

11 List of Symbols

Greek letters

Symbol	Units	Description	Symbol	Units	Description
α	-	Transfer coefficient	ξ	$\text{mol H}_2\text{O mol H}^{+\,-1}$	Electroosmotic drag coefficient
β	-	Symmetry factor	ρ	kg m^{-3}	Density
γ	-	Activity coefficient	σ	$-$	CL Nafion content
γ_a	-	Real to geom. surface area	σ_i	S m^{-1}	Conductivity of phase i
δ	m	Thickness	σ_{12}	m	Collision diameter
δ_{Naf}	m	Nafion layer thickness covering the agglomerates	ς_{Naf}^{CL}	$-$	Nafion fraction in CL
			ς_{Naf}	$-$	Agglomerate Nafion fraction
ϵ	-	Porosity	τ	$-$	Tortuosity
ϵ_{LJ}	-	Lennard Jones potential	υ	m^2s^{-1}	Kinematic viscosity
ϵ_{th}	-	Threshold porosity	φ	V	Potential
ε	F m^{-1}	Lateral interaction factor for adsorbed species	ϕ	$-$	Thiele Module, Fugacity coefficient
η	V	Overpotential	χ	$-$	Pore to gas molecule diameter
η_{th}	$-$	Thermodynamic efficiency	$\chi_{i,j}$	$-$	Non-ideality parameter
θ	-	Surface coverage	ω	s^{-1}	Radial velocity
λ	$\text{mol SO}_3^-\text{ mol H}_2\text{O}^{-1}$	Nafion water content	ω_f	$-$	Acentric factor
μ_i	kJ mol^{-1}	Electrochemical potential	Ω_D	$-$	Collision's integral

Latin letters

Symbol	Units	Description	Symbol	Units	Description
a	$-$	Activity	N_i^m	$\text{mol m}^{-2}\text{ s}^{-1}$	Molar flux of component i
a_{CL}	m^{-1}	Specific agglomerate surface area per CL volume	N_m	$-$	Single chain units between Nafion cross-links
a_{Pt}^o	m^{-1}	Specific active surface area	Oc	Mio. Euro	Annual electrolyzer operating cost
A	A mol^{-1}	Preexponential factor	P	Pa	Pressure
Bi	$-$	Biot number	p^o	Pa	Vapor pressure
c	mol m^{-3}	Concentration	p_c	Pa	Critical pressure
$c^{m/n}$	mol m^{-3}	Interface concentration	r	$\text{mol m}^{-3}\text{ s}^{-1}$	Volumetric reaction rate
C_p	$\text{kJmol}^{-1}\text{ K}^{-1}$	Specific heat capacity	r_{agg}	m	Agglomerate radius
D	$\text{m}^2\text{ s}^{-1}$	Diffusion coefficient	r_e	m	Electrode radius
E	V	Potential	r_s	$\text{mol m}^{-2}\text{ s}^{-1}$	Surface reaction rate
E_a	kJ mol^{-1}	Activation energy	$rw_{Pt/C}$	$-$	platinum to carbon ratio
E_o	V	Thermodynamic potential	R	$\text{J mol}^{-1}\text{ K}^{-1}$	Gas constant
Ef	$-$	Effectiveness factor	Re	-	Reynold's number
EW	$\text{gr mol SO}_3^{-\,-1}$	Equivalent weight	S	$\text{kJ mol}^{-1}\text{K}^{-1}$	Entropy

f_p	–	Packing factor	S_{el}	m^2	Electrochem. active surface area	
F	$A\,s\,mol^{-1}$	Faraday's constant	ΔS_f	$kJ\,mol^{-1}K^{-1}$	Entropy of formation	
G	$kJ\,mol^{-1}$	Gibb's energy	S_m	m^2	Surface area of phase m	
h	$A\,cm^{-2}\,mg^{-1}$	Nafion normalized current	Sc	–	Schmidt number	
H	$kJ\,mol^{-1}$	Enthalpy	T	K	Temperature	
H_i	$m^3\,Pa\,mol^{-1}$	Henry constant	T_c	K	Critical temperature	
ΔH_f	$kJ\,mol^{-1}$	Enthalpy of formation	T_s	°C	Temperature	
j	$A\,m^{-2}$	Surface current density	u	$m\,s^{-1}$	Velocity of discharge flow rate	
j_{kin}	$A\,m^{-2}$	Kinetic current density	U	V	Cell potential	
j_l	$A\,m^{-2}$	Limiting current density	U_{rev}	V	Reversible potential	
j_o	$A\,m^{-2}$	Exchange current density	U_{th}	V	Thermoneutral potential	
i	$A\,kg^{-1}$	Specific mass current	v	–	Stoichiometric coefficient	
k	mol	Volumetric kinetic constant	V_c	$cm^3 gr^{-1}$	Critical volume	
k_b	$J\,K^{-1}$	Boltzman constant	V_i	m^3	Volume of phase i	
k_d	m^2	Permeability	V_m	$m^3 mol^{-1}$	Molar vol. of a single Nafion chain	
k_m	$m\,s^{-1}$	Mass transfer coefficient	$\dot{V}$	$ml\,s^{-1}$	Flow rate	
k_k		Modified reaction constant	$\overline{V}$	$m^3 mol^{-1}$	Molar volume	
l_i	$mg\,cm^{-2}$	Loading of component i	w_{H_2O}	-	Weight fraction of water	
m_i	$mol\,kg^{-1}$	Molality of component i	W_{Cl_2}	$kWh\,ton\,Cl_2^{-1}$	Mol fraction of the liquid phase	
m_b	$mV\,dec^{-1}$	Tafel slope	x	-	Mol fraction of the liquid phase	
M_i	$mol\,L^{-1}$	Molarity of component i	y	-	Mol fraction of the gas phase	
MW_i	$gr\,mol^{-1}$	Molar weight of component i	z	-	Number of electrons transferred	
n	–	Reaction order	z_g	-	Compressibility factor	
N_{agg}	–	Number of agglomerates	z_i	-	Charge of component i	

12 List of Abreviations

Abbreviation	Description	Abbreviation	Description
CL	Catalyst layer	HV	Heyrovsky-Volmer mechanism
CV	Cyclic voltammetry	HTV	Heyrovsky-Tafel-Volmer mechanism
DLS	Dynamic light scattering	MEA	Membrane electrode assembly
DSA	Dimension stable anode	ODC	Oxygen depolarized cathode
EDC	Ethylene dichloride	ORR	Oxygen reduction reaction
GDE	Gas diffusion electrode	PEM	Polymer electrolyte membrane
GDL	Gas diffusion layer	PVC	Polyvinyl chloride
$HClOR$	Hydrogen chloride oxidation reaction	RDE	Rotating disk electrode
HDL	Hydrodynamic diffusion layer	SHE	Standard hydrogen electrode
HER	Hydrogen evolution reaction		
HT	Heyrovsky-Tafel mechanism		

13   Figures

---

14 Tables

15 References

1.   Greenwood, N., Earnshaw, A., *Chemistry of the Elements*. 1997: Butterworth-Heinemann.
2.   Chlor, E., *Chlorine Tree*, E. Chlor, Editor. 2012.
3.   Eurochlor, *Chlorine Industry Review 2011-2012*, Eurochlor, Editor. 2012: Brussels, Belgium. p. 48.
4.   O'Brien, T.F., T.V. Bommaraju, and F. Hine, *Chlor-Alkali Technologies*. 2005, Springer: New York. p. 111-114.
5.   ThyssenKrupp Uhde, G., *Hydrochloric Acid Electrolysis - Sustainable Chlorine Production*. 2012, ThyssenKrupp Uhde GmbH: Dortmund, Germany. p. 24.
6.   Vidakovic-Koch, T., *et al.*, Membranes, 2012. **2**(3): p. 510-528.
7.   Perez-Ramirez, J., *et al.*, Energy & Environmental Science, 2011. **4**(12): p. 4786-4799.
8.   Iwanaga, K.S., K.; Hibi, T.; Issoh, K.; Suzuta, T.; Nakada, M.; Mori, Y.; Abe, T., *The Development of Improved Hydrogen Chloride Oxidation Process*, in *Sumitomo Kagaku: R&D Report*. 2004, Sumitomo Chemical Co., Ltd.: Tokyo.
9.   Blachnik, I., *Strompreis in Deutschland im Vergleich 2000-2012*, in *Strompreis in Deutschland*. 2012, Agentur für Erneuerbare Energien: Berlin.
10. Eames, D.J. and J. Newman, Journal of The Electrochemical Society, 1995. **142**(11): p. 3619-3625.
11. Motupally, S., A.J. Becker, and J.W. Weidner, Journal of The Electrochemical Society, 2002. **149**(5): p. D63-D71.
12. Zimmerman, W.H.S., T. F.; Artysiewicz, J. S.; Trainham; J. A.; Law, C. G.; Newman, J. S.; Eames, D. J., *Electrochemical conversion of anhydrous hydrogen halide to halogens gas using a membrane-electrode assembly or gas diffusion electrodes* E.I.d.P.d.N.a. Company, Editor. 1994: USA. p. 43.
13. Wilson, M.S. and S. Gottesfeld, Journal of Applied Electrochemistry, 1992. **22**(1): p. 1-7.
14. Duby, P., JOM, 1993. **45**(3): p. 41-43.
15. Malmgren, C., *et al.*, Journal of Physics: Conference Series, 2008. **100**(5): p. 052026.
16. Viswanathan, B.H., M. , Bull. Catal. Soc. India, 2007. **6**: p. 50– 66.
17. Balko, E.N., J.F. McElroy, and A.B. LaConti, International Journal of Hydrogen Energy, 1981. **6**(6): p. 577-587.
18. Zawodzinski, T.A., *et al.*, Journal of the Electrochemical Society, 1993. **140**(4): p. 1041-1047.
19. Bettelheim, A., *et al.*, Analytical Chemistry, 1991. **63**(23): p. 2724-2727.
20. Baturina, O.A., *et al.*, Journal of The Electrochemical Society, 2011. **158**(10): p. B1198-B1205.
21. Schwitzgebel, G. and F. Endres, Journal of Electroanalytical Chemistry, 1995. **386**(1–2): p. 11-16.
22. Okada, T., *et al.*, Electrochimica Acta, 1998. **43**(24): p. 3741-3747.
23. Balko, E.N., Journal of Applied Electrochemistry, 1980.
24. Slade, S., *et al.*, Journal of The Electrochemical Society, 2002. **149**(12): p. A1556-A1564.
25. Yeo, R.S. and J. McBreen, Journal of The Electrochemical Society, 1979. **126**(10): p. 1682-1687.
26. Hoormann, D., H. Pütter, and J. Jörissen, Chemie Ingenieur Technik, 2005. **77**(9): p. 1363-1376.
27. Bratsch, S.G., Journal of Physical and Chemical Reference Data, 1989. **18**(1): p. 1-21.
28. Wright, S.H., Advances in Physiology Education, 2004. **28**(4): p. 139-142.
29. Sundmacher, K., Journal of Applied Electrochemistry, 1999. **29**(8): p. 919-926.
30. Litster, S. and G. McLean, Journal of Power Sources, 2004. **130**(1–2): p. 61-76.
31. Kuwertz, R., *Elektrolyse von Chlorwasserstoff in einem Polymerelektrolyt-Membranreaktor mit Sauerstoffverzehrkathode: Herstellung der Reaktorkomponenten und Konzeption der Versuchsanlage*, in *Institut für Chemische Verfahrenstechnik*. 2010, TU Clausthal: Clausthal-Zellerfeld.
32. Lindermeir, A., *et al.*, Journal of Power Sources, 2004. **129**(2): p. 180-187.
33. Wang, S., *et al.*, Journal of Power Sources, 2007. **165**(1): p. 128-133.
34. von Kraemer, S., *et al.*, Journal of Power Sources, 2008. **180**(1): p. 185-190.

35.   Zecevic, S.K., *et al.*, Journal of The Electrochemical Society, 1997. **144**(9): p. 2973-2982.
36.   García-Rodríguez, S., *et al.*, International Journal of Hydrogen Energy, 2010. **35**(20): p. 11576-11581.
37.   Lee, S.J., *et al.*, Electrochimica Acta, 1998. **43**(24): p. 3693-3701.
38.   Sasikumar, G., J.W. Ihm, and H. Ryu, Journal of Power Sources, 2004. **132**(1–2): p. 11-17.
39.   Lee, S.P., J.; Su S.; Jung, K., 2007. **53**(2): p. 12.
40.   Vidakovic, T., *Kinetics of Methanol Electrooxidation on PtRu Catalysts in a Membrane Electrode Assembly*, in *Fakultät für Verfahrens- und Systemtechik*. 2005, Otto-von-Guericke-Universität Magdeburg: Magdeburg.
41.   Trasatti, S., Electrochimica Acta, 1987. **32**(3): p. 369-382.
42.   Jörissen, J., T. Turek, and R. Weber, Chemie in Unserer Zeit, 2011. **45**(3): p. 172-183.
43.   Hine, F., M. Yasuda, and M. Iwata, Journal of The Electrochemical Society, 1974. **121**(6): p. 749-756.
44.   Kim, M.-s., *et al.*, Journal of Chemical Technology & Biotechnology, 2013. **88**(7): p. 1212-1219.
45.   Zhang, J., *PEM Fuel Cell Catalysts and Catalyst Layers - Fundamentals and Applications*. 2008: Springer. 1137.
46.   Gonzalez Martinez, I., *et al.*, Journal of the Serbian Chemical Society, 2013. **78**(12): p. 2115-2130.
47.   Banham, D.W., J.N. Soderberg, and V.I. Birss, The Journal of Physical Chemistry C, 2009. **113**(23): p. 10103-10111.
48.   Lai, C.-M., *et al.*, International Journal of Hydrogen Energy, 2008. **33**(15): p. 4132-4137.
49.   Xie, J., *et al.*, Electrochimica Acta, 2010. **55**(24): p. 7404-7412.
50.   Hallinan, D.T. and Y.A. Elabd, The Journal of Physical Chemistry B, 2007. **111**(46): p. 13221-13230.
51.   Parthasarathy, A., C.R. Martin, and S. Srinivasan, Journal of the Electrochemical Society, 1991. **138**(4): p. 916-921.
52.   Parthasarathy, A., *et al.*, Journal of the Electrochemical Society, 1992. **139**(9): p. 2530-2537.
53.   Group, S., *Systems – HCl Syntheses*, in *Process Technology*, S. Group, Editor. 2012: Wiesbaden.
54.   Koestner, R., *et al.*, Langmuir, 2011. **27**(16): p. 10157-10166.
55.   Gileadi, E., *Electrode kinetics for chemists, chemical engineers, and materials scientists*. 1993, VCH.
56.   Pourbaix, M.J.N., J. Van Muylder, and N. de Zoubov, Platinum Metals Review, 1959. **3**(2): p. 47.
57.   Nylén, L. and K.T.h.l.f. kemiteknik, *Critical Potential and Oxygen Evolution of the Chlorate Anode*. 2006.
58.   Adžić, R.R., *et al.*, *Proceedings of the Symposium on Oxygen Electrochemistry*. 1996: Electrochemical Society.
59.   Perry, M.L., J. Newman, and E.J. Cairns, Journal of The Electrochemical Society, 1998. **145**(1): p. 5-15.
60.   Martinez, I.G., *et al.*, Electrochimica Acta, 2014. **123**(0): p. 387-394.
61.   Eikerling, M., A.A. Kornyshev, and A.R. Kucernak, Physics Today, 2006. **59**(10): p. 38-44.
62.   Quintech, *Gas Distribution Layer*, in *Fuel Cell Technology*. 2010, Quintech: Göppingen.
63.   Jiang, J. and A. Kucernak, Journal of Solid State Electrochemistry, 2012. **16**(8): p. 2571-2579.
64.   Koper, M.T.C., *Fuel Cell Catalysis: A Surface Science Approach*. Wiley Series on Electrocatalysis and Electrochemistry, ed. A. Wieckowski. 2009: John Wiley & Sons. 720.
65.   Beattie, P.D., V.I. Basura, and S. Holdcroft, Journal of Electroanalytical Chemistry, 1999. **468**(2): p. 180-192.
66.   Sun, W., B.A. Peppley, and K. Karan, Electrochimica Acta, 2005. **50**(16-17): p. 3359-3374.
67.   Kim, K.-H., *et al.*, International Journal of Hydrogen Energy, 2010. **35**(5): p. 2119-2126.
68.   Takamatsu, T., M. Hashiyama, and A. Eisenberg, Journal of Applied Polymer Science, 1979. **24**(11): p. 2199-2220.
69.   Chirkov, Y. and V. Rostokin, Russian Journal of Electrochemistry, 2009. **45**(9): p. 1027-1036.

70. Shen, L. and Z.X. Chen, Chemical Engineering Science, 2007. **62**(14): p. 3748-3755.
71. Benziger, J., *et al.*, Aiche Journal, 2011. **57**(9): p. 2505-2517.
72. Schmidt, T.J., *et al.*, Journal of Electroanalytical Chemistry, 2001. **508**(1): p. 41-47.
73. Unnikrishnan, E.K., S.D. Kumar, and B. Maiti, Journal of Membrane Science, 1997. **137**(1–2): p. 133-137.
74. Hamann, C.H., Vielstich, W., *Elektrochemie*. 2005, Weinheim: Wiley-VCH.
75. Vlachos, D.G., A.B. Mhadeshwar, and N.S. Kaisare, Computers & Chemical Engineering, 2006. **30**(10-12): p. 1712-1724.
76. Goddard, W.A., *et al.*, Molecular Simulation, 2006. **32**(3-4): p. 251-268.
77. Wang, Q.P., *et al.*, Journal of Electroanalytical Chemistry, 2004. **573**(1): p. 61-69.
78. Weber, A.Z. and J. Newman, Chemical Reviews, 2004. **104**(10): p. 4679-4726.
79. Cheddie, D.F. and N.D.H. Munroe, Journal of Power Sources, 2008. **183**(1): p. 164-173.
80. Danilov, V.A. and I. Moon, Chemical Engineering Communications, 2007. **194**(11): p. 1531-1542.
81. Fuhrmann, F., Zhao, H., Holzbecher, E., Langmach, H., Journal of Fuel Cell Science and Technology, 2008. **5**(2): p. 021008.
82. Ruiz, J.A.a.Z., C. F., International Journal of Chemical Reactor Engineering, 2010. **8**(39).
83. Wang, Y. and X. Feng, Journal of The Electrochemical Society, 2008. **155**(12): p. B1289-B1295.
84. You, L. and H. Liu, International Journal of Hydrogen Energy, 2001. **26**(9): p. 991-999.
85. Dawes, J.E., *et al.*, Chemical Engineering Science, 2009. **64**(12): p. 2781-2794.
86. Min, C.-H., Journal of Power Sources, 2010. **195**(7): p. 1880-1887.
87. Okada, T., Journal of New Materials for Electrochemical Systems, 2001. **4**(4).
88. Sahraoui, M., C. Kharrat, and K. Halouani, International Journal of Hydrogen Energy, 2009. **34**(7): p. 3091-3103.
89. Limjeerajarus, N. and T. Yamaguchi, Proceedings of the Asme 8th International Conference on Fuel Cell Science, Engineering, and Technology 2010, Vol 2, 2010: p. 317-320.
90. Limjeerajarus, N.Y., Tatsunori; Yamamoto, Toshio, Journal of Chemical Engineering of Japan, 2009. **42**(10): p. 771-781.
91. Das, P.K., X. Li, and Z.-S. Liu, Journal of Electroanalytical Chemistry, 2007. **604**(2): p. 72-90.
92. Das, P.K., X. Li, and Z.S. Liu, Journal of Power Sources, 2008. **179**(1): p. 186-199.
93. Liu, Z.S., *et al.*, Journal of Electroanalytical Chemistry, 2004. **573**(1): p. 61-69.
94. Rama, P., *et al.*, Energy & Fuels, 2010. **24**: p. 3130-3143.
95. Suh, D.M. and S.B. Park. *Modeling of transport phenomena in polymer electrolyte fuel cells*. 2010.
96. Harvey, D., J.G. Pharoah, and K. Karan, Journal of Power Sources, 2008. **179**(1): p. 209-219.
97. Das, P.K., X.G. Li, and Z.S. Liu, Journal of Power Sources, 2008. **179**(1): p. 186-199.
98. Mauritz, K.A. and R.B. Moore, Chemical Reviews, 2004. **104**(10): p. 4535-4586.
99. Bernardi, D.M. and M.W. Verbrugge, Aiche Journal, 1991. **37**(8): p. 1151-1163.
100. Shah, A.A., G.-S. Kim, and K. Promislow, IMA Journal of Applied Mathematics, 2007. **72**(3): p. 302-330.
101. Durlofsky, L. and J.F. Brady, Physics of Fluids, 1987. **30**(11): p. 3329-3341.
102. Neuman, S.P., Acta Mechanica, 1977. **25**(3): p. 153-170.
103. Parthasarathy, A., *et al.*, Journal of the Electrochemical Society, 1992. **139**(10): p. 2856-2862.
104. Gonzalez Martinez, I.V.-K., T.; Kuwertz, R.; Kunz, U.; Turek, T.; Sundmacher, K., J. Serb. Chem. Soc. , 2013.
105. Gonzalez Martinez, I., Vidaković-Koch, T.,Kuwertz, R., Kunz,U., and T. Turek, Sundmacher, K., Electrochimica Acta, 2013.
106. NuVant, S. *ELAT™ Gas Diffusion Layer*. Fuel Cell Electrode Fabrication Equipment 2010 [cited 2012 27.08.2012].
107. Gode, P., *et al.*, Electrochimica Acta, 2003. **48**(28): p. 4175-4187.
108. Perry, R.H., and Green, D. W., *Perry's Chemical Engineers' Handbook*. 6th ed. 1984, New York: McGraw-Hill.

109. Carmo, M., *et al.*, Journal of Power Sources, 2007. **173**(2): p. 860-866.
110. Inchem, I., *Chemical Safety Information from Intergovernmental Organizations*. 2011, IPCS Inchem.
111. Hinatsu, J.T., M. Mizuhata, and H. Takenaka, Journal of the Electrochemical Society, 1994. **141**(6): p. 1493-1498.
112. Morris, D.R. and X. Sun, Journal of Applied Polymer Science, 1993. **50**(8): p. 1445-1452.
113. Xu, H.B., E.; Garzon, F.; Uribe, F.; Wilson, M.; Pivovar, B., ed. Proton Exchange Membrane Fuel Cells, ed. T.G. Fuller, H. A.; Cleghorn, S.; Ramani, V.; Zhao, T.; Nguyen, T. V.; Haug, A.; Bock, C.; Lamy, C.; Ota, K. Vol. 7. 2007, The Electrochemical Society: New Jersey, USA.
114. Gasteiger, H.A., J.E. Panels, and S.G. Yan, Journal of Power Sources, 2004. **127**(1–2): p. 162-171.
115. Secanell, M., *et al.*, Structural and Multidisciplinary Optimization, 2010. **40**(1-6): p. 563-583.
116. Kittel, C., *Solid State Physics*. 7th ed. 1996, New York: John Wiley & Sons.
117. Kamarajugadda, S. and S. Mazumder, Journal of Power Sources, 2008. **183**(2): p. 629-642.
118. Xia, Z.T., *et al.*, Canadian Journal of Chemistry-Revue Canadienne De Chimie, 2008. **86**(7): p. 657-667.
119. Hongsirikarn, K., *et al.*, Journal of Power Sources, 2010. **195**(17): p. 5493-5500.
120. Xie, J. *Microstructural Characterization of PEM Fuel Cells*. 2004. Los Álamos, USA.
121. Yin, K.-M., Journal of The Electrochemical Society, 2005. **152**(3): p. A583-A593.
122. Broka, K. and P. Ekdunge, Journal of Applied Electrochemistry, 1997. **27**(3): p. 281-289.
123. Jain, P., L.T. Biegler, and M.S. Jhon, Journal of the Electrochemical Society, 2010. **157**(8): p. B1222-B1229.
124. Barbir, F., *PEM Fuel Cells: Theory and Practice*. 2005, Burlington: Elsevier Academic Press. 456.
125. Yan, W.-M., *et al.*, Journal of Power Sources, 2010. **195**(17): p. 5731-5734.
126. Hussaini, I.S. and C.Y. Wang, Journal of Power Sources, 2010. **195**(12): p. 3822-3829.
127. Choi, P., N.H. Jalani, and R. Datta, Journal of The Electrochemical Society, 2005. **152**(3): p. E123-E130.
128. Schultz, T. and K.S. Sundmacher, Journal of Power Sources, 2005. **145**(2): p. 435-462.
129. Izquierdo-Gil, M.A., *et al.*, Chemical Engineering Science, 2012. **72**(0): p. 1-9.
130. Jonquières, A., *et al.*, Journal of Membrane Science, 1998. **147**(1): p. 59-71.
131. Zawodzinski, T.A.D., C.; Radzinski, S.; Sherman, R. J.; Smith, V. T.; Springer, T. E.; Gottesfeld, S., Journal of The Electrochemical Society, 1993. **140**(4): p. 1041-1047.
132. Schultz, T., *Experimental and Model-based Analysis of the Steady-state and Dynamic Operating Behaviour of the Direct Methanol Fuel Cell (DMFC)*, in *Institute for Process Engineering*. 2004, Otto-von-Guericke University: Magdeburg.
133. Lide, D.R., *CRC Handbook of Chemistry and Physics*, W.M. Haynes, Editor. 2012, CRC Press: Boca Raton, FL.
134. Motupally, S., A.J. Becker, and J.W. Weidner, Journal of The Electrochemical Society, 2000. **147**(9): p. 3171-3177.
135. Pletcher, D.W., F.C., *Industrial Electrochemistry*. 2nd ed. 1990, New York: Chapman and Hall.
136. Kuwertz, R., *et al.*, Electrochemistry Communications, 2013. **34**(C): p. 320-322.
137. Zhang, J., *et al.*, Journal of Power Sources, 2006. **163**(1): p. 532-537.
138. Ignaszak, A., S. Ye, and E. Gyenge, Journal of Physical Chemistry C, 2009. **113**(1): p. 298-307.
139. Parthasarathy, A., *et al.*, Journal of Electroanalytical Chemistry, 1992. **339**(1–2): p. 101-121.
140. Motupally, S.M., D. T.; Freire, F. J.; Weidner, W., The Electrochemical Society: Interface, 1998. **7**(3): p. 5.
141. Six, C. and F. Richter, *Isocyanates, Organic*. 2000, Wiley-VCH Verlag GmbH & Co. KGaA.
142. Japan Soda Industry, A., *Safe Handling of Hydrochloric Acid*, P.C.o.T.a. Safety, Editor. 2006: Tokyo.
143. ISOPA, *Toluene Diisocyanate (TDI) & Methylenediphenyl Diisocyanate (MDI)*, ISOPA, Editor. 2012, ISOPA: Brussels, Belgium. p. 31.

144. Entec, *Data on manufacture, import, export, uses and releases of 4-4' diaminodiphenylmethane as well as information on potential alternatives to its use*, Entec, Editor. 2010, Entec: Brussels, Belgium. p. 31.

145. Gemchem, *MDI, PMDI, TDI & Aliphatic di-isocyanates: All producers and plant capacities*, Gemchem, Editor. 2013, Gemchem: Brussels, Belgium.

146. Burgess, D.R., *Thermochemical Data*, in *NIST Chemistry WebBook, NIST Standard Reference Database*. National Institute of Standards and Technology

147. Atkins, P. and J. De Paula, *Physical Chemistry*. 2006: Oxford University Press.

148. Chen, N.H. and D.F. Othmer, Journal of Chemical & Engineering Data, 1962. **7**(1): p. 37-41.

149. Das, P.K., X. Li, and Z.-S. Liu, Applied Energy, 2010. **87**(9): p. 2785-2796.

150. Wexler A.; Greenspan, L., Journal of Research of the National Bureau of Standards, Physics and Chemistry, 1976. **80A**(5).

151. Peng, D.-Y. and D.B. Robinson, Industrial & Engineering Chemistry Fundamentals, 1976. **15**(1): p. 59-64.

152. Smith, J.M.V., N. H. C., *Introduction to chemical engineering thermodynamics*. 1959, New York: McGraw-Hill.

153. Cerquetti, A., P. Longhi, and T. Mussini, Journal of Chemical & Engineering Data, 1968. **13**(4): p. 458-461.

154. Seger, B., K. Vinodgopal, and P.V. Kamat, Langmuir, 2007. **23**(10): p. 5471-5476.

155. Umeda, M., *et al.*, Ionics, 2013. **19**(4): p. 623-627.

156. LaManna, J. and S.G. Kandlikar, ASME Conference Proceedings, 2008. **2008**(48345): p. 1305-1315.

157. Berg, P., A. Novruzi, and K. Promislow, Chemical Engineering Science, 2006. **61**(13): p. 4316-4331.

158. Djilali, N. and P.C. Sui, International Journal of Computational Fluid Dynamics, 2008. **22**(1-2): p. 115-133.

159. Jang, J.-H., *et al.*, International Journal of Hydrogen Energy, 2008. **33**(1): p. 156-164.

160. Jaouen, F., G. Lindbergh, and G. Sundholm, Journal of The Electrochemical Society, 2002. **149**(4): p. A437-A447.

161. Bird, R.B., Steward, W. E., Lightfoot, E. N., *Transport Phenomena*. 2nd ed. 2002, New York: Wiley. 914.

162. Poling, B.E., J.M. Prausnitz, and J.O. O'Connell, *Properties of Gases and Liquids*. 2001 ed. 2001: McGraw Hill Professional. 768.

163. Othmer, D.F. and H.T. Chen, Industrial & Engineering Chemistry Process Design and Development, 1962. **1**(4): p. 249-&.

164. Vanleeuwen, M.E., Molecular Physics, 1994. **82**(2): p. 383-392.

165. Fairbanks, D.F. and C.R. Wilke, Industrial & Engineering Chemistry, 1950. **42**(3): p. 471-475.

166. Schwitzgebel, G. and F. Endres, Journal of Electroanalytical Chemistry, 1995. **386**(1): p. 11-16.

167. Nguyen, T.V. and R.E. White, Journal of the Electrochemical Society, 1993. **140**(8): p. 2178-2186.

168. Perry, R.H.G., D.W., *Perry's Chemical Engineers' Handbook*. 1997, McGraw-Hill: New York.

169. Bertagnolli, H., P. Chieux, and H.G. Hertz, Journal of the Chemical Society, Faraday Transactions 1: Physical Chemistry in Condensed Phases, 1987. **83**(3): p. 687-695.

170. Harpst, J.A., E. Holt, and P.A. Lyons, The Journal of Physical Chemistry, 1965. **69**(7): p. 2333-2335.

171. Chen, H.N., G.A. Voth, and N. Agmon, Journal of Physical Chemistry B, 2010. **114**(1): p. 333-339.

172. Hyun, K.S., Plastics Fundamental Research, The Dow Chemical Company, 1965.

173. Mourits, F.M. and F.H.A. Rummens, Canadian Journal of Chemistry-Revue Canadienne De Chimie, 1977. **55**(16): p. 3007-3020.

174. Krieger, F.J., *Calculation of the Viscosity of Gas Mixtures*. 1951, RAND Corporation: Santa Monica.

175. Solvay GmbH, *HCl: Product Characteristics*. 2005: Hannover.

176. Alberti, G., R. Narducci, and M. Sganappa, Journal of Power Sources, 2008. **178**(2): p. 575-583.
177. Toray Industries, I., *Toray Carbon Fiber Paper* in *TGP Series*. 2008.
178. Zook, L.A. and J. Leddy, Analytical Chemistry, 1996. **68**(21): p. 3793-3796.
179. Oberbroeckling, K.J., *et al.*, Analytical Chemistry, 2002. **74**(18): p. 4794-4799.
180. McCutcheon, S.C.M., J.L.; Barnwell, T.O., *Water Quality*. Handbood of Hydrology, ed. D.R. Maidment. 1993, New York: McGraw-Hill.
181. Macdonald, F. and D.R. Lide, Abstracts of Papers of the American Chemical Society, 2003. **225**: p. U552-U552.
182. Pantea, D., *et al.*, Carbon, 2001. **39**(8): p. 1147-1158.
183. Bernardi, D.M. and M.W. Verbrugge, Journal of the Electrochemical Society, 1992. **139**(9): p. 2477-2491.
184. Springer, T.E., T.A. Zawodzinski, and S. Gottesfeld, Journal of the Electrochemical Society, 1991. **138**(8): p. 2334-2342.
185. Tsampas, M.N., *et al.*, Electrochimica Acta, 2006. **51**(13): p. 2743-2755.
186. Smith, J.M., Van Ness, H.C.,, *Introduction to Chemical Engineering Thermodynamics*. 4th ed. 1987, New York: McGraw-Hill.
187. Adams, F.W. and R.G. Edmonds, Industrial & Engineering Chemistry, 1937. **29**(4): p. 447-451.
188. Korbach, J., *Absorption of Hydrogen Chloride* P.S. Department, Editor. 2008, De Dietrich Process Systems GmbH: Mainz.
189. Nichols, T.T., D., *Thermodynamic Phase and Chemical Equilibrium at 0-110°C for the H+ -K+ -Na+ -CI- -H2O system up to 16 Molal and the HNO3-H2O system up to 20 Molal using an association-based Pitzer Model compatible with ASPEN Plus*, in *Thermodynamic Phase and Chemical Equilibrium*. 2003, Idaho National Engineering and Environmental Laboratory: Idaho.